

COMPUTER AIDED DIAGNOSIS OF LUNG GROUND GLASS OPACITY NODULES AND LARGE LUNG CANCERS IN CT

BY JINGHAO ZHOU

A dissertation submitted to the
Graduate School—New Brunswick
Rutgers, The State University of New Jersey
and
The Graduate School of Biomedical Sciences
University of Medicine and Dentistry of New Jersey
in partial fulfillment of the requirements for the
Joint Degree of Doctor of Philosophy
Graduate Program in Biomedical Engineering

Written under the direction of

Dimitris Metaxas

and approved by

New Brunswick, New Jersey

October, 2008

© 2008

Jinghao Zhou

ALL RIGHTS RESERVED

ABSTRACT OF THE DISSERTATION

Computer Aided Diagnosis of Lung Ground Glass Opacity Nodules and Large Lung Cancers in CT

by Jinghao Zhou

Dissertation Director: Dimitris Metaxas

Diagnosis of lung nodules and cancers is a critical and urgent problem in clinical diagnosis. This thesis is to design and build a computer aided lung ground glass opacity (GGO) nodules and large lung cancers diagnosis system which aims to quantify the volumetric change of the lung GGO nodules and large lung cancers between the pre-treatment and post-treatment. In order to quantify the volumetric change of the lung nodules and cancers over time, segmentation and registration methods are used to determine the same lung nodule or cancer between the pre-treatment and post-treatment. We first perform a pre-selection method and extract the centerlines of tubular objects by applying intensity ridge tracing method. While tracing tubular objects, bifurcation points are automatically detected from the cross-sectional planes by applying scan-conversion method or Adaboost algorithm. For the registration method, we develop a 3D-3D model based rigid registration method based on bifurcation points. This rigid registration method minimizes the least square error of the corresponding bifurcation points between the planning CT images and the respiration-correlated CT images. For the lung GGO nodules and large lung cancers detection and segmentation, we propose a novel method to automatically detect and segment lung GGO nodules and large lung

cancers from chest CT images. For lung GGO nodules detection, we develop a classifier by boosting k-Nearest Neighbor. We then apply a clustering method to detect the regions of the lung GGO nodules. The detected regions of lung GGO nodules are then automatically segmented. We also present the statistical validation of the proposed classifier for lung GGO (10 datasets contains 10 GGO nodules) detection as well as the promising results of automatic lung GGO nodules segmentation. The improvement of the method of large lung cancers is that we propose a robust active shape model method for automatic segmentation of lung areas which can be distorted by large lung cancers. We present the statistical validation of the proposed classifier for large lung cancers (10 datasets contains 16 large lung cancers) detection as well as the very promising results of automatic large lung cancers segmentation.

Acknowledgements

I am grateful to Professor Dimitris Metaxas for his advice, encouragement, trust, and support over my Ph.D. years. He has been an excellent advisor and always directed me toward doing fundamental research that will make a difference. He also exposed me to infinite possibilities by doing research in Medical Image Analysis, Computer Vision and Machine Learning. None of the work in this thesis would have happened without him.

I would like to thank the other members of my doctoral committee: Prof. Leon Axel, Prof. Anant Madabhushi and Prof. John Li, for their advices, help and valuable suggestions regarding this thesis. It is a privilege for me to have each of them serve in my committee.

I also thank Prof. Sukmoon Chang. He has been a wonderful mentor to me, and contributed many ideas and insights to the work that I present in this thesis. Thanks also go to many professors at Rutgers that have helped and supported me through the long process, especially to Prof. Troy Shinbrot, Prof. Thomas V. Pappathomas, Prof. Ahmed Elgammal, Prof. Vladimir Pavlovic, Prof. Cun-Hui Zhang, Prof. Minge Xie, Prof. John Kolassa.

Thanks to my friends and colleagues from the Center for Computational Biomedicine Imaging and Modeling (CBIM). I benefited a lot from their friendship and help.

Finally, thanks go to many of my collaborators without whose help I would not have achieved as much. Special thanks to Prof. Leon Axel at New York University, Dr. Binsheng Zhao at Memorial Sloan-Kettering Cancer Center, Dr. Gig Mageras at Memorial Sloan-Kettering Cancer Center, Dr. Michelle S. Ginsberg at Memorial Sloan-Kettering Cancer Center, Dr. Lawrence H. Schwartz at Memorial Sloan-Kettering Cancer Center, for providing crucial data that are used in my doctoral research.

Dedication

This thesis is dedicated to my wife, Yanyan Xu, and to my parents, Yongguo Zhou and Yuehua Liang, who have supported me all the way since the beginning of my studies. Also, this thesis is dedicated to all those who believe in the richness of learning.

Table of Contents

Abstract	ii
Acknowledgements	iv
Dedication	v
List of Tables	x
List of Figures	xii
1. Introduction	1
1.1. The lungs on CT	2
1.1.1. Computed tomography	2
1.1.2. Computed tomography of the lungs	3
1.1.3. Lung anatomy on CT	5
1.1.4. Lung cancer on CT	7
1.2. Brief overview of image analysis and machine learning tools employed in this thesis	9
1.3. Organization of this thesis	12
2. Previous Literature	14
2.1. Segmentation of lung structures	14
2.1.1. Lung segmentation on CT	14
2.1.2. Segmentation of pulmonary airways on CT	15
2.1.3. Segmentation of vessels	16
A. Pattern recognition techniques	18
B. Model based approaches	20
C. Neural network based approaches	22

2.1.4.	Lobar segmentation	23
2.2.	Registration	24
2.3.	Computerized detection, quantification and classification	26
2.3.1.	Lung cancer: detection of lung nodules	26
2.3.2.	Lung cancer: characterization of lung nodules	29
2.3.3.	Lung cancer: nodule size measurements	30
3.	Novel Contribution of This Thesis Work	33
3.1.	Segmentation of tubular organs	33
3.2.	Registration of tubular organs	35
3.3.	Detection and segmentation of lung GGO nodules	37
3.4.	Detection and segmentation of large lung cancers	38
4.	Methods	40
4.1.	Segmentation	40
4.1.1.	Eigenanalysis of the Hessian matrix	40
4.1.2.	3D texture likelihood map method	41
4.1.3.	Robust active shape models (RASM)	42
4.2.	Reconstruction	44
4.2.1.	Vessel radii estimation by spherical deformable model	44
4.3.	Registration	45
4.3.1.	3D-3D model based rigid registration	45
4.4.	CAD methods	46
4.4.1.	Vessel and noise suppression with 3D cylinder filters	46
4.4.2.	Scan-conversion method	46
4.4.3.	Adaboost learning method	48
	A. Feature design	49
	B. Adaboost learning	49
4.4.4.	Boost k -NN	51
4.5.	Evaluation techniques	52

4.5.1. Receiver Operating Characteristic Curves (ROC) Curve	52
4.5.2. Overlap rate	53
4.5.3. Bhattacharya distance	53
4.5.4. Mean distance	53
4.5.5. Root mean square error	53
5. Tubular Objects Segmentation with Bifurcation Detection in Lung	54
5.1. Vessel direction estimation	54
5.2. Vessel normal plane extraction	54
5.3. Vessel bifurcation detection using scan-conversion method	54
5.4. Vessel bifurcation detection using Adaboost learning method	54
5.5. 3D reconstruction	54
5.6. Results	55
5.6.1. Qualitative Results	56
5.6.2. Quantitative Results	57
A. Scan-conversion method	57
B. Adaboost learning method	58
C. Comparison of two bifurcation detection method	60
6. Tubular Objects Registration in Lung	61
6.1. Tubular organ direction estimation and normal plane extraction	61
6.2. Bifurcation detection using Adaboost	61
6.3. Tubular organs radius estimation for 3D reconstruction	61
6.4. Tubular organs registration	61
6.5. Results	61
6.5.1. Qualitative Results	62
6.5.2. Quantitative Results	63
7. Lung GGO Nodules Detection and Segmentation	66
7.1. Threshold for lung area segmentation	66

7.2. Vessel and noise suppression with 3D cylinder filters	66
7.3. Detection of GGO	67
7.4. Segmentation of GGO using nonparametric density estimation	67
7.5. Removal vessels overlapped with lung abnormalities	68
7.6. Results and Discussion	68
7.6.1. Qualitative Results	68
7.6.2. Quantitative Results	68
7.6.3. Discussion	70
8. Large lung cancers detection and segmentation	75
8.1. Robust active shape models (RASM) for lung area segmentation	75
8.2. Detection of large lung cancers	75
8.3. Segmentation of large lung cancers	76
8.4. Removal vessels overlapped with large lung cancers	77
8.5. Results	77
8.5.1. Qualitative Results	77
8.5.2. Quantitative Results	78
9. Concluding Remarks and Future Work	83
References	85
Vita	100

List of Tables

1.1. Treatment methods of different types of lung cancers	8
1.2. Nomenclature of related work	9
2.1. Papers on airways segmentation. The variables in the table include number of scans (#), slice thickness (mm), the algorithm, whether the method is automatic or not (Auto), 2D or 3D (Dim), and the result. .	17
2.2. Papers on pattern recognition techniques. The variables in the table include the author name of the paper (Paper), the algorithm (Method), input type, whether the method is multi-scale (Multiscale), the result such as centerlines (Cen.), edges (Ed.), Junctions (Junc.). Whether the method segment the whole tree, whether the method has bifurcation detection (Bi).	18
2.3. Nomenclature of pattern recognition techniques.	19
2.4. Papers on model based approaches. The variables in the table include the author name of the paper (Paper), the algorithm (Method), input type, whether the method is multi-scale (Multiscale), the result such as centerlines (Cen.), edges (Ed.), Junctions (Junc.). Whether the method segment the whole tree, whether the method has bifurcation detection (Bi).	20
2.5. Nomenclature of model based approaches.	21

2.6. Papers on neural network based approaches. The variables in the table include the author name of the paper (Paper), the algorithm (Method), input type, whether the method is multi-scale (Multiscale), the result such as centerlines (Cen.), edges (Ed.), Junctions (Junc.). Whether the method segment the whole tree, whether the method has bifurcation detection (Bi).	23
2.7. Nomenclature of neural network based approaches.	23
2.8. Papers on approaches of detection of lung nodules and false positive reduction. The variables in the table include the author name of the paper (Paper), the false positive reduction algorithm (FP reduction), Data description, the performance.	27
2.9. Papers on approaches of characterization of lung nodules. The variables in the table include the author name of the paper (Paper), Data description, Features used, Dimension (Dim), Classifier and the result.	30
4.1. Criteria for eigenvalues and corresponding shapes.	40
5.1. Results of bifurcation detection using scan-conversion algorithm.	57
6.1. Results of the registration method on clinical datasets.	64
7.1. Comparisons. $d1$ and $d2$ are the greatest diameter and its greatest perpendicular distance of each GGO. Vol is the volume of each GGO. Overlap ratio is the volume overlap ratio of the manual segmentation results and automatic segmentation results. Manual and Auto are the measurements on the manual segmentation results and the automatic segmentation results, respectively.	74
8.1. Comparisons. $d1$ and $d2$ are the greatest diameter and its greatest perpendicular distance of each tumor. Vol is the volume of each tumor. Overlap ratio is the volume overlap ratio of the manual segmentation results and automatic segmentation results. Manual and Auto are the measurements on the manual segmentation results and the automatic segmentation results, respectively.	79

List of Figures

1.1.	1.6 CT slices of the lung, taken from a 3D data volume in three main orientations. (a) The image in the coronal plane. (b) The image in the transverse plane. (c) The image in the sagittal plane.	4
1.2.	The illustration of the anatomy of human lung. The upper image shows the view in the coronal plane and the lower image shows the view in the transverse plane. Picture Source: Medical-dictionary.thefreedictionary.com	6
1.3.	An HRCT slice of lung in the transverse plane with arrows indicating a perpendicular cross-section of a bronchus (B), a vessel (V) and a fissure (F).	7
1.4.	The branching structure of the airway tree. The number in the middle column shows the number of the branching generation.	8
1.5.	The flow chart of a typical CAD system which has five steps.	11
1.6.	The flow chart of the organization of this thesis.	13
4.1.	Tracing along the direction of the vessel. Figure shows \mathbf{e}_3 and the normal plane defined by \mathbf{e}_1 and \mathbf{e}_2	41
4.2.	HH barriers and TT barriers. (a) in one ridge. (b) in two ridges.	47
4.3.	The vessel cross-sectional planes without bifurcation (a) and with bifurcation (c). The gradient field only has HH barriers (c), and the gradient field has HH and TT barriers (d). The red point is the mass center. The squares in (d) denote the TT barriers.	48

4.4.	(a) The vessel cross-sectional planes with bifurcation (top row) and without bifurcation (bottom row), (b) 2D Gaussian used for low frequency information detection, (c) the first derivatives of Gaussian used for edge detection, and (d) the second derivatives of Gaussian used for ridge detection.	50
5.1.	The flow chart of vessel segmentation method using scan-conversion method to detect bifurcation points.	55
5.2.	The flow chart of vessel segmentation method using Adaboost method to detect bifurcation points.	56
5.3.	Visual validation. (a) cross-sectional planes, (b) centerlines superimposed on an isosurface of the initial image. The blue point in (b) shows the bifurcation point detected.	57
5.4.	Vessel segmentation and bifurcation detection. (a) centerlines superimposed on an isosurface of the initial image, (b) 3D reconstruction of vessels from the graph representation of vessels in (a). Blue points in (a) shows the bifurcation points detected by our method.	58
5.5.	Error rate. (a) Mean training and test error curves of Adaboost (training error: lower curve, test error: upper curve), (b) Comparison of the mean error rates of Adaboost and various classifiers	59
5.6.	ROC curve measures the performance of the Adaboost learning method.	60
5.7.	A normal plane of a vessel bifurcation and two selected weak features are presented. (a) a normal plane of a vessel bifurcation. (b) the first selected weak feature. (c) the second selected weak feature.	60
6.1.	The flow chart of airways registration method.	62
6.2.	Pulmonary tracheobronchial tree segmentation and bifurcation detection. (a) centerlines superimposed on an isosurface of the initial image, (b) 3D reconstruction of pulmonary tracheobronchial tree from the graph representation in (a). Blue points in (a) shows the bifurcation points detected by our method.	63

6.3.	Registration results. Blue shows the 3D reconstruction of pulmonary tracheobronchial tree in the registered planning images and red shows 3D reconstruction of pulmonary tracheobronchial tree in the respiration-correlated images.	64
6.4.	ROC curve measures the performance of the Adaboost learning method.	65
7.1.	The flow chart of GGO detection and segmentation method.	67
7.2.	Effect of F_{cyl} . (a) Original volume, (b) Volume filtered with F_{cyl} , (c) After thresholding.	68
7.3.	Histogram of a cylinder filtered volume.	69
7.4.	Volumetric samples for learning. (a) Positive (GGO) samples, (b) Negative (non GGO) samples.	70
7.5.	Typical probability density functions of positive (solid line, GGO), negative (dash-dot line, typical background), and negative (dotted line, typical vessels) examples.	71
7.6.	GGO segmentation. (a) ROI containing a classified GGO, (b) 3D likelihood map in ROI, (c) 3D likelihood map in ROI after vessel removal. . .	71
7.7.	ROC curve measures the performance of the Boosted k -NN method for GGO detection.	72
7.8.	Comparison of the mean error rates of various classifiers by bootstrapping.	72
7.9.	GGO segmentation—four segmented GGO nodules are shown. (a) original CT images containing GGO nodules, (b) enlarged GGO areas, (c) segmented GGO, (d) 3D reconstruction of segmented GGO overlaid with original CT images in (a), and (e) 3D reconstruction of segmented GGO with other nearby structures.	73
8.1.	The flow chart of large lung cancers detection and segmentation method.	76

8.2.	The segmented lung area using RASM. Red points are active shape model and green lines are the connected contour. (a) Large cancers attached to the chest wall and mediastinum (large red circle) and the initialization of the ASM, (b) ASM finding the false boundary of lung, and (c) RASM finding the correct boundary of lung and the large white area in the left lung is a large lung cancer.	77
8.3.	Effects of F_{cyl} (only one slice from the whole volume is shown). (a) Original volume, (b) Volume filtered with F_{cyl} , and (c) Volume after thresholding.	78
8.4.	Results. Segmented large lung lesions projected onto a slice (left) and corresponding 3D lesions (middle and right).	81
8.5.	ROC curve measures the performance of the Boosted k -NN method for large lung cancer detection.	82

Chapter 1

Introduction

Lung cancer is responsible for more than 25% of all cancer-related deaths every year and lung cancer kills more people than breast, colon and prostate cancers combined [1]. Only 16% of lung cancer patients are diagnosed before their diseases have spread to other parts of their bodies (e.g., regional lymph nodes and beyond), compared to more than 50% of breast cancer patients and 90% of prostate cancer patients [2]. Also, the results of the Early Lung Cancer Action Project suggested that nodules with pure or mixed Ground Glass Opacity at the thin-section CT are likely to be malignant or cancerous [3].

The facts above show that the diagnosis of lung nodules and lung cancers is a very difficult and urgent problem in clinical diagnosis. This thesis is to design and build a computer aided lung ground glass opacity (GGO) nodules and large lung cancers diagnosis system which aims to quantify the volumetric change of the lung GGO nodules and large lung cancers between the pre-treatment and post-treatment. The difficulties of such system are how to segment the tubular objects (as landmarks), how to register the tubular objects with topology changes and how to quantitatively analyze the corresponding lung GGO nodules and large lung cancers.

This introduction chapter is to familiarize the reader with the problem and solving approaches. The lungs on computed tomography (CT) are explained in section 1.1. Then, a brief overview of image analysis and machine learning tools employed in this thesis is in section 1.2. Organization of this thesis is in section 1.3.

1.1 The lungs on CT

1.1.1 Computed tomography

The concepts of the basis of CT can be traced back to the beginning of 20th century. However, it was until 1972 the first commercially CT scanner was invented by Sir Godfrey Newbold Hounsfield in Hayes, United Kingdom at EMI Central Research Laboratories based on X-rays. Within 10 years, more than 10,000 devices were used in clinical and medical centers around the world. CT is not only the breakthrough from the discovery of X-ray, but also a milestone of diagnostic radiology and radiation therapy. An overview of CT technology and applications is presented in [4].

CT scanner includes a radiation source and a set of detectors. The radiation source circles around the patient body and the detectors measure the attenuation of the radiation at different angle. From these measurements, computers are used to reconstruct a slice of the section of the patient body. A stack of such slices is obtained by moving source and detectors to capture slices at close positions. Multiple slices which constitute a three dimensional volume of the patient are obtained using two methods: conventional CT scans take pictures of slices of the body, while helical CT scans take pictures as the X-ray tube helically circles the patient. A detailed description of the equations of reconstruction and the practical methods of solving them is presented in [5] and [6].

Values in a CT image are called Hounsfield unit (HU). They are the measurements of a physical property of the tissue displayed, i.e., the radiation attenuation coefficient μ of the tissue. The value of μ varies with the wavelength and the strength of the radiation, but the ratio of μ between different materials does not. The Hounsfield unit (HU) is a linear transformation of the original linear attenuation coefficient measurement, where the radiodensity of distilled water at standard pressure and temperature (STP) is defined as zero Hounsfield units (HU), while the radiodensity of air at STP is defined as -1000 HU. For a material X with linear attenuation coefficient μ , the corresponding HU value is therefore given by:

$$CTvalue = \frac{\mu_X - \mu_{H_2O}}{\mu_{H_2O} - \mu_{air}} \times 1000$$

where μ_{H_2O} and μ_{air} are the linear attenuation coefficients of water and air, respectively, at STP. Thus, a change of one Hounsfield unit (HU) represents a change of 0.1% of the attenuation coefficient difference between water and air, or approximately 0.1% of the attenuation coefficient of water since the attenuation coefficient of air is nearly zero. Using this scale, images from different and properly calibrated scanners can be quantitatively compared.

CT has had tremendous improvements [4, 7] after it was created. New CT scanners use a continuously rotating gantry that contains the radiation source. The detectors are set out in a stationary array and form a complete circle. The gantry performs a complete rotation within a second and during that time, more than 64 slices can be acquired simultaneously since rows of circular detector arrays are mounted close to each other. The images are commonly composed of a matrix of 512×512 pixels in each direction and the image resolution can be as high as 0.3 mm per pixel. Isotropic 3D volume can be obtained based on setting the slice thickness to the same range as image resolution. It takes less than a minute to scan a complete patient body now.

1.1.2 Computed tomography of the lungs

CT scanner had fast speed and high resolution to make it an important instrument in the imaging of the lungs in 1980 [8]. The high-resolution CT (HRCT) scanners were developed, in which the thickness of slices was approximately 1 mm thick. However, the acquisition speed became a hamper to the amount of slices that could be acquired during a breathing period. As the aim of HRCT is to assess a generalized lung disease, the test is conventionally performed by taking thin sections 10-40 mm apart. This type of noncontiguous scans are used today since the added diagnostic value of the slices in between does not exceed the increase in radiation dose received by the patient [9].

There are three most commonly separated axial planes (the coronal plane, the transverse plane and the sagittal plane) to represent a 3D volume. Three CT image slices of separated axial planes from a 3D HRCT volume of the lung are demonstrated in Fig. 1.1.

Pixels in an image obtained by CT scanning are displayed in terms of relative

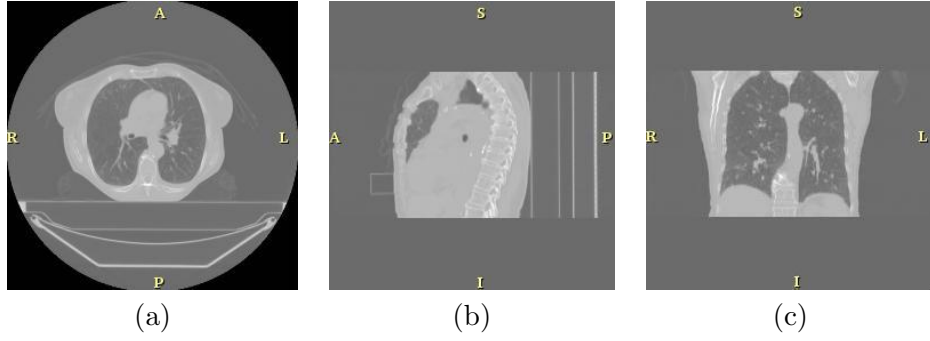


Figure 1.1: 1.6 CT slices of the lung, taken from a 3D data volume in three main orientations. (a) The image in the coronal plane. (b) The image in the transverse plane. (c) The image in the sagittal plane.

radiodensity. The pixel itself is displayed according to the mean attenuation of the tissue(s) that it corresponds to on a scale from -1024 to +3071 on the Hounsfield scale. Pixel is a two dimensional unit based on the matrix size and the field of view. When the CT slice thickness is also factored in, the unit is known as a voxel, which is a three dimensional unit.

The phenomenon that one part of the detector cannot differ between different tissues is called the “Partial Volume Effect”. That means that a big amount of cartilage and a thin layer of compact bone can cause the same attenuation in a voxel as hyperdense cartilage alone. Water has an attenuation of 0 Hounsfield units (HU) while air is -1000 HU, cancellous bone is typically +400 HU, cranial bone can reach 2000 HU or more. The attenuation of metallic implants depends on atomic number of the element used: Titanium usually has an amount of +1000 HU, iron steel can completely extinguish the X-ray and is therefore responsible for well-known line-artifacts in computed tomograms. Artifacts are caused by abrupt transitions between low- and high-density materials, which results in data values that exceed the dynamic range of the processing electronics.

The images are displayed using a windowing technology since human eyes cannot identify so many grey levels. Windowing is the process of using the calculated Hounsfield units to make an image. The display device can only resolve 256 shades of gray. These shades of gray can be distributed over a wide range of HU values to get an overview of structures that attenuate the beam to widely varying degrees. Alternatively, these

shades of gray can be distributed over a narrow range of HU values (called a “narrow window”) centered over the average HU value of a particular structure to be evaluated. In this way, subtle variations in the internal makeup of the structure can be discerned. This is a commonly used image processing technique known as contrast compression. For example, to evaluate the abdomen in order to find subtle masses in the liver, one might use liver windows. Choosing 70 HU as an average HU value for liver, the shades of gray can be distributed over a narrow window or range. One could use 170 HU as the narrow window, with 85 HU above the 70 HU average value; 85 HU below it. Therefore the liver window would extend from -15 HU to +155 HU. All the shades of gray for the image would be distributed in this range of Hounsfield values. Any HU value below -15 would be pure black, and any HU value above 155 HU would be pure white in this example. Using this same logic, bone windows would use a “wide window” (to evaluate everything from fat-containing medullary bone that contains the marrow, to the dense cortical bone), and the center or level would be a value in the hundreds of Hounsfield units. To an untrained person, these window controls would correspond to the more familiar “Brightness” (Window Level) and “Contrast” (Window Width).

1.1.3 Lung anatomy on CT

We talk about the human anatomy in order to understand what is visible in an HRCT slice of the lung (Fig. 1.2). The lungs are contained within the thoracic cavity. The diaphragm encloses it at the bottom and the rib cage and intercostal muscles form the top and sides of the thoracic cavity. The lungs are contained in two pleural membranes or pleurae. The pleura visceralis encloses the lungs, the pleura parietalis adheres closely to the chest walls and the diaphragm. The pleurae are isolated by a thin film of fluid. This lets them to glide across each other without friction during breathing. The lung essentially exists free in the thoracic cavity. It holds its form and size due to the vacuum between the pleura and the chest wall. If the chest wall is punctured, the lungs collapse. The lung consists of airways, vessels, and connective tissue called the interstitium which is a framework of thin membranes that supports the structure of the lung. The lung airways and lung vessels are laid out in a tree-like network which is

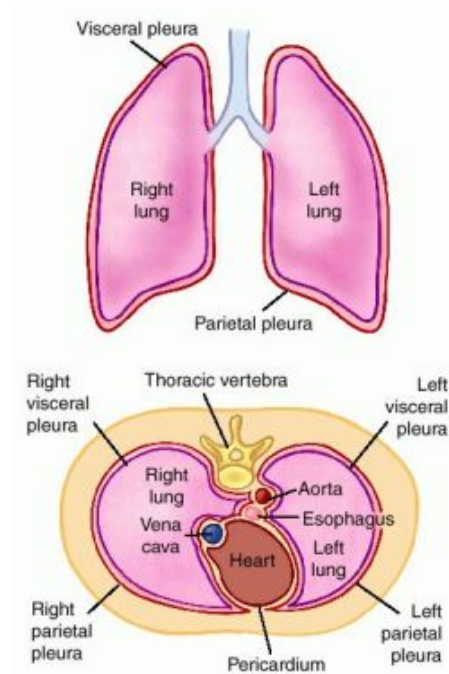


Figure 1.2: The illustration of the anatomy of human lung. The upper image shows the view in the coronal plane and the lower image shows the view in the transverse plane. Picture Source: Medical-dictionary.thefreedictionary.com

dividing into increasingly smaller branches starting at the hilum which is the location where they enter the lungs. The arterial vessel tree lies along side the bronchial tree and each vessel is attached by a bronchus of approximately equal size. In perpendicular cross-sections, such a bronchovascular pair seems as one hole closed and one hole open which is often called a “signet ring” sign (Fig. 1.3). There are also veins which do not accompany a bronchus.

Human lungs are located in two cavities on either side of the heart. Though similar in appearance, the two are not identical. Both are separated into lobes, with three lobes on the right and two on the left. The lobes are further divided into lobules, hexagonal divisions of the lungs that are the smallest subdivision visible to the naked eye by membranes called the fissures, which can be seen as lines on a high-resolution CT slice (Figure 1.3).

The airways have around 23 branching generations until they achieve in alveolar sacs. The alveolar sacs are grapelike clusters and exist of many alveoli which are the gas exchange sites of the lung (Fig. 1.4). The smallest anatomical unit that can be

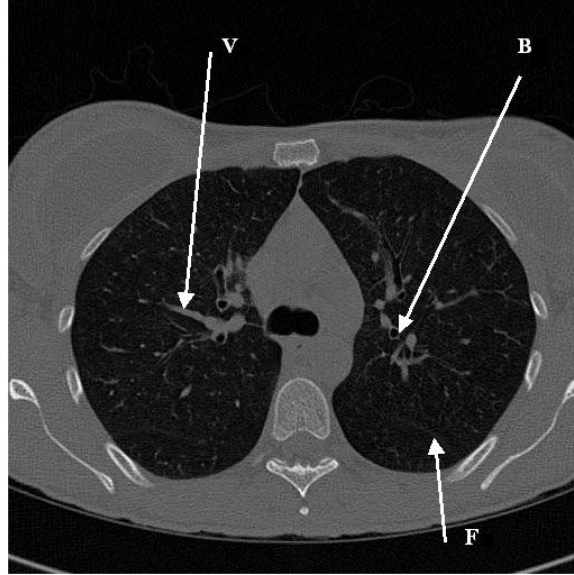


Figure 1.3: An HRCT slice of lung in the transverse plane with arrows indicating a perpendicular cross-section of a bronchus (B), a vessel (V) and a fissure (F).

viewed on HRCT is the secondary lobule, at the 16th branching generations [10]. The secondary lobule is the smallest discrete portion of the lung that is surrounded by connective tissue. It is 2 to 3 cm in diameter and contains up to 12 of the acini. It can show up on HRCT as a polygon with a blood vessel in the middle. The terminal bronchiole, the airway that accompanies the vessel, has such a thin wall that it cannot be seen.

1.1.4 Lung cancer on CT

HRCT scans of the lung are made to establish the presence or progression of disease in clinical field. They will therefore seldom show a set of normal healthy lungs. The work in chapters 3 through 5 of this thesis is centered specifically on automated computer aided diagnosis system of the lung cancers.

Lung cancer is a disease of uncontrolled cell growth in tissues of the lung. This growth may lead to metastasis, invasion of adjacent tissue and infiltration beyond the lungs. The vast majority of primary lung cancers are carcinomas of the lung, derived from epithelial cells. Lung cancer, the most common cause of cancer-related death in men and the second most common in women, is responsible for 1.6 million deaths

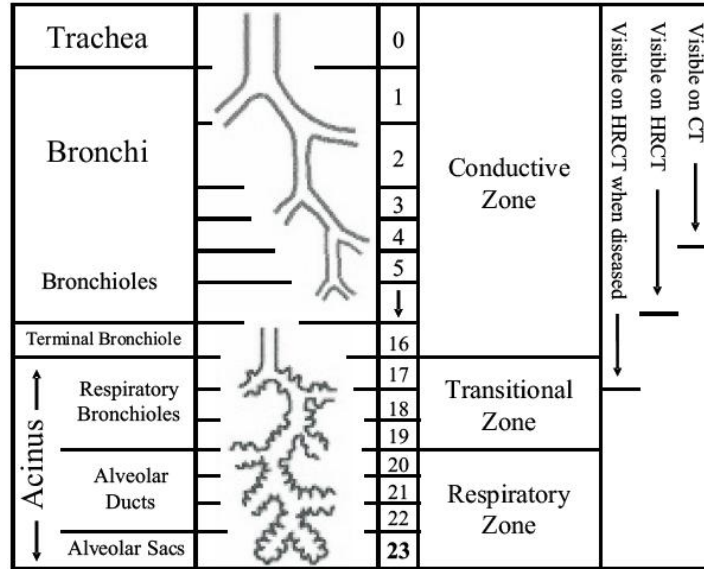


Figure 1.4: The branching structure of the airway tree. The number in the middle column shows the number of the branching generation.

Table 1.1: Treatment methods of different types of lung cancers

Type	Treatment method
Small cell lung cancer	Chemotherapy, Radiation
Non-small cell lung cancer	Surgery

worldwide annually [1]. The most common symptoms are shortness of breath, coughing (including coughing up blood), and weight loss [11].

The main types of lung cancer are small cell lung carcinoma and non-small cell lung carcinoma. Different types of lung cancer need different treatment methods (see Table 1.1); non-small cell lung carcinoma (NSCLC) is sometimes treated with surgery, while small cell lung carcinoma (SCLC) usually responds better to chemotherapy and radiation [12]. The most common cause of lung cancer is long term exposure to tobacco smoke. The occurrence of lung cancer in non-smokers, who account for fewer than 10% of cases, appears to be due to a combination of genetic factors, radon gas, asbestos, and air pollution, including second-hand smoke [13, 14, 15, 16, 17, 18, 19].

Lung cancer may be seen on chest x-ray and computed tomography (CT) scan. Performing a chest x-ray is the first step if a patient reports symptoms that may be suggestive of lung cancer. If there are no x-ray findings but the suspicion is high (such

Table 1.2: Nomenclature of related work

ANN	Artificial neural network.
AUC	Area under the ROC curve.
CAD	Computer-aided detection/diagnosis.
CT	Computed tomography.
CTA	CT angiography.
EC	Explosion controlled region growing.
FN	False negative.
FP	False positive.
HRCT	High-resolution computed tomography.
PVE	Partial volume effect.
ROC	Receiver Operating Characteristic.
ROI	Region of interest.
TN	True negative.
TP	True positive.
VOI	Volume of interest.

as a heavy smoker with blood-stained sputum), bronchoscopy and/or a CT scan may provide the necessary information.

The diagnosis is confirmed with a biopsy. This is usually performed via bronchoscopy or CT-guided biopsy. Treatment and prognosis depend upon the histological type of cancer, the stage (degree of spread), and the patient's performance status. Possible treatments include surgery, chemotherapy, and radiotherapy. With treatment, the five-year survival rate is 14% [12].

1.2 Brief overview of image analysis and machine learning tools employed in this thesis

In this section, we introduce the terminology and the general methods which are important in the medical image analysis field. The key concepts are image segmentation, image registration, machine learning and image visualization. The nomenclature used in this thesis is shown in Table 1.2.

Image segmentation refers techniques to detect and delineate the anatomical objects of interest in the image, discriminating each object from other objects and from its background. Image registration is a fundamental task in medical image processing

used to match multiple images taken, for example, at different times, with different sensors, or from different subjects. This technique provides basis for image comparison and information integration in many clinical applications.

Machine learning, a broad subfield of artificial intelligence, is concerned with the design and development of algorithms and techniques that allow computers to “learn”. At a general level, there are two types of learning: inductive and deductive. Inductive machine learning methods extract rules and patterns out of massive data sets. The major focus of machine learning research is to extract information from data automatically, by computational and statistical methods. Hence, machine learning is closely related not only to data mining and statistics, but also theoretical computer science. Machine learning algorithms are organized into a taxonomy, based on the desired outcome of the algorithm. Common algorithm types include Supervised learning, Unsupervised learning, Semi-Supervised learning, Reinforcement learning, Transduction and Learning to learn. We will focus on Supervised learning.

Supervised learning is a machine learning technique for learning a function from training data. The training data consist of pairs of input objects (typically vectors), and desired outputs. The output of the function can be a continuous value (called regression), or can predict a class label of the input object (called classification). The task of the supervised learner is to predict the value of the function for any valid input object after having seen a number of training examples (i.e. pairs of input and target output). To achieve this, the learner has to generalize from the presented data to unseen situations in a “reasonable” way. The parallel task in human and animal psychology is often referred to as concept learning.

Image visualization is a technique to provide visual feedback for image interpretation and for display of analysis results in 3-D. In conventional 2-D imaging, an experienced diagnostician views a sequence of 2-D images, mentally transforms them into an impression of the 3-D anatomy and pathology, then makes the diagnosis or performs an interventional procedure. This process is not only time consuming and inefficient, but more importantly, variable and subjective, which may lead to incorrect decisions in diagnosis, planning and delivering the therapy. Image visualization is to overcome the

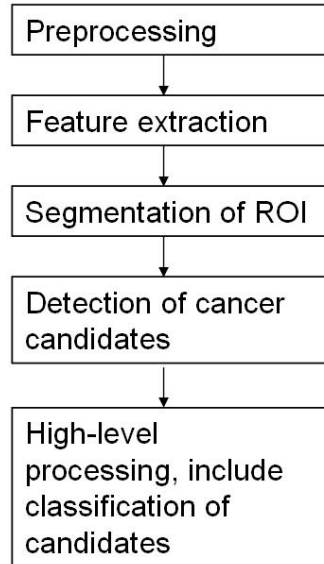


Figure 1.5: The flow chart of a typical CAD system which has five steps.

limitations of conventional 2-D imaging and provide the diagnostician or therapist a more complete view of the anatomy in 3-D. For example, it can place the 2-D image plane at any location within an organ; orient the 2-D image to the optimal image plane, and give more accurate estimation of organ. With the advance of computer hardware, it is desirable to develop image visualization system for real-time image manipulation and rendering and provides intuitive tools for controlling the multi-dimensional image to allow extraction of the needed information.

The goal of the work in this thesis is to design and build a computer aided diagnosis (CAD) system for lung cancers. The stages of a typical CAD system are shown in the flow chart (Fig. 1.5).

Steps 1 through 4 involve image processing of the image data. Prior knowledge on the Techniques such as filtering, thresholding, region growing, connected component analysis and mathematical morphology is assumed. They can be found in the standard textbooks on image processing [20].

Step 5 is performed in the feature space; the space spanned by the feature vectors calculated to represent the image segments. “Classification” in this space involves the process of finding the decision boundaries that separate the different classes. Popular techniques such as artificial neural networks (ANN) or linear discriminant classifiers

(LDC) can be found in textbooks on pattern recognition [21, 22].

For the evaluation of the classification results, different measures are used depending on the number of classes, N , involved in the classification.

A two-class classification problem is for example the discrimination between normal and abnormal (or diseased) tissue. Diseased samples are called “positive” samples, normal samples are called “negative” samples. For such a problem, three measures of performance should be given: accuracy, sensitivity and specificity. Accuracy is the total fraction of correctly classified samples. Sensitivity and specificity are the fractions of correctly classified positive and negative samples, respectively. For a classifier that makes no classification errors at all, all three measures have the value 1. There is a trade-off between sensitivity and specificity. A classifier that marks all samples as being positive will achieve a sensitivity of one, but will have zero specificity. This trade-off can be measured using ROC curves, which measure sensitivity as a function of specificity.

For multiple classes classification, the evaluation of the performance is through the single measures of accuracy, or by giving a confusion matrix. Accuracy is the total fraction of correctly classified samples. In the presence of a dominant class to which the majority of the samples belong, accuracy is not a reliable measure of performance. A confusion matrix is a matrix with on one axis the true classes to which the samples belong, and on the other axis the classes to which the samples were assigned in the classification procedure. Correctly classified samples end up on the diagonal. The confusion matrix gives insight into which pairs of classes are confused most, that is, which pairs of classes are responsible for the most classification errors.

1.3 Organization of this thesis

The first chapter is the introduction. Second chapter is the review of previous literature. Third chapter present the novel contributions of this thesis work. Forth chapter is on the methods. Chapter five to chapter eight show the clinical applications. The last chapter is the conclusion and future work (Fig. 1.6).

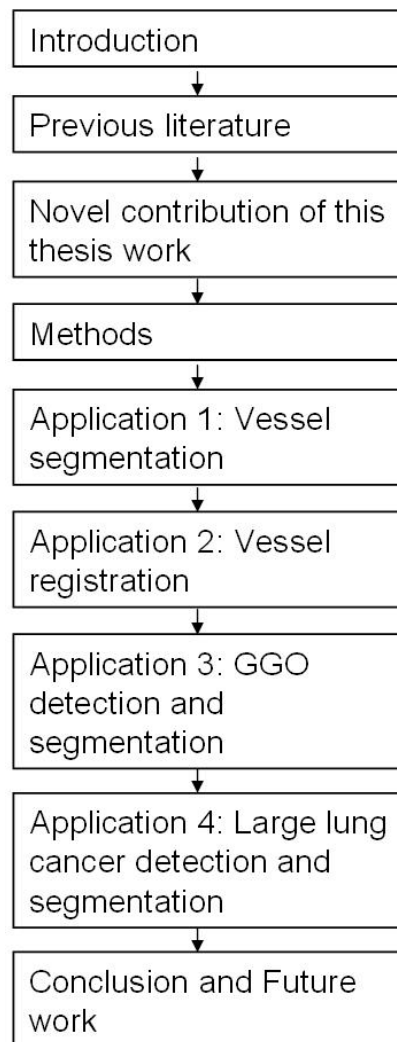


Figure 1.6: The flow chart of the organization of this thesis.

Chapter 2

Previous Literature

2.1 Segmentation of lung structures

2.1.1 Lung segmentation on CT

Any computer aided diagnosis system that analyzes the lungs needs an automatic lung segmentation. Armato and Sensakovic presented that the accurate segmentation of lung is a pre-processing step in a CAD scheme [23]. In a lung nodule detection system, they showed that 5 to 17% of the lung nodules in their test data was missed due to the pre-processing segmentation. This depended on whether or not the segmentation algorithm was adapted to the nodule detection procedure.

As the main part of the lung is full of air, it appears as a dark region in CT. This contrast between lung and surrounding tissues helps setup most of the segmentation methods. Most of the methods are region-based [24, 25, 26, 27] or contour-based [28, 29]. The main lung volume is found in two ways in region-based approach. One way is the thresholding based on the intensity values, followed by the connected component labeling (alternatively connected component analysis). After the method is applied, the lungs are identified by imposing rules on size and location. The other way is the region growing. The volume is found by region growing from the trachea. The trachea itself is found by searching for 2D circular air-filled regions in the first slices of the scan, or by searching for a 3D tubular air-filled object located centrally in the top half of the scan. After obtained the combined lung and airway volume, the separation of left and right lungs and removal of the trachea and the main stem bronchi are performed. This approach uses the mathematical morphology technique to obtain the smooth lung volumes without holes. Zhou et al. [29] proposed a robust active shape model to segment

lung areas that are distorted and occluded by large lung lesions. These large lung lesions are hard to segment due to the similarity of the intensities between the cancers and the surrounding structures in CT images. Li and Reinhardt proposed a 3D active shape model that provided an approximate segmentation of a single lung and was combined with multiple 2D refinements to capture details and shape variance not present in the statistics of the training data [28].

One difficulty is at what points the segmentations are supposed to cut through the major airways and vessels in the hilar area where they enter the lung. Manual segmentation also show much variance around the hilum, depending on smoothness we want. Ukil and Reinhardt used a segmentation of the bronchial tree to improve their lung segmentation in hilar area [30].

Other difficulties of the segmentation requiring special attention are the posterior and anterior junctions between left and right lung. These junctions can be very thin and consequently of low contrast due to the partial volume effects (PVE). The solution to this problem is to heuristically search a given region in each affected axial slice and find a separating junction line inside it. The line is either defined as a shortest distance in anterior-posterior direction [27, 31, 26].

Another challenge is the lungs affected by high density pathologies that are connected to the lung border. Due to a lack of contrast between lung and surrounding tissues, thresholding methods will fail to segment these pathological parts of the lung. Zhou et al. proposed a robust active shape model to segment lung areas that are distorted and occluded by large lung lesions [29]. Sluimer et al., proposed registration with a presegmented reference scan [32].

2.1.2 Segmentation of pulmonary airways on CT

The pulmonary airways have a tree structure (the tracheobronchial tree) of cylindrical branches of decreasing radius and divide into the left and right main bronchus. These bronchi repeatedly divide into smaller bronchi, up to the 23th branching generation [10]. The bronchi are filled with air and surrounded by the bronchial wall which has a relatively high CT value.

On a normal dose CT scan, a radiologist might trace bronchi up to branching generation 7. Lumen and bronchus wall combine into an indistinguishable mass after exceeding the generation 7. In the last decade, a number of methods have been proposed to automatically or semiautomatically segment the tracheobronchial tree [33, 34, 35, 36, 37]. Computerized schemes have been developed to label the different bronchi such that the branches with problems can be pinpointed anatomically [36, 38]. There are also a number of methods proposed to measure the geometrical properties of the bronchi at user given locations [39, 40, 41]. These methods can be used to diagnose a number of respiratory disease.

The existing methods for airways segmentation can be divided into four main categories: region growing [33, 34, 42], knowledge-based segmentation [33, 34], centreline extraction [37, 43, 44, 45] and mathematical morphology [46, 47]. Some methods combine two or more of these methods. For example, the region growing method called the explosion controlled (EC) region growing [48, 36, 46] is an iterative region growing process with increasing threshold value until the total number of voxels grown increases too much in one iteration step. In Table 2.1, the various studies on pulmonary airways (tracheobronchial tree) segmentation are presented. The variables in the table include the number of scans, slice thickness, the algorithm, whether the method is automatic or not, 2D or 3D, and the result.

Many challenges of the segmentation of pulmonary airways lie in the segmentation in the pathological and low-dose scans. The main problems are leakage and obstructions. The source of these problems might come from noise, tissue movement, high-density implants, PVE, mucus, atelectases and pathology.

2.1.3 Segmentation of vessels

Each lung includes an arterial and a venous vessel tree. When the pulmonary arteries and veins enter the lungs, their diameter can be up to 30 mm. As they divide, vessel diameters decrease. In a normal CT scan vessels can be measured up to 5-10 mm from the pleura. The arterial vessel tree lies along side the bronchial tree and each vessel is attached by a bronchus of approximately equal size. In perpendicular cross-sections,

Table 2.1: Papers on airways segmentation. The variables in the table include number of scans (#), slice thickness (mm), the algorithm, whether the method is automatic or not (Auto), 2D or 3D (Dim), and the result.

Paper	#	mm	Method	Dim	Auto	Result
Sonka et al. [33]	5	3	lung segmentation, region grow, rule-based candidate detection	2/3	-	count branches; TP=68.5%, FP=11.5%
Park et al. [34]	5	3	lung segmentation, region grow, fuzzy-logic candidate detection	2/3	-	count branches; TP=69.1%, FP=8.8%
Sato et al. [35]	1	1	cropping, threshold, multi-scale line filtering, connected components	3	-	count centreline points; ROC-curve
Mori et al. [36]	14	2/5	EC, thinning rule-based FP removal	3	Y	count branches; 67% detected, 85% of $\leq 4^{th}$
Deschamps and Cohen [37]	1	-	calculate minimal path between 2 points	3	N	path found
Aylward and Bullitt [43]	1	-	dynamic ridge traversal	3	N	qualitative analysis
Zhou et al. [45]	10	2.5	eigenanalysis, bifurcation detection,	3	N	qualitative analysis, bifurcations
Tschirren et al. [49]	33	-	VOI, multi-seeded fuzzy connectivity, minitor leaks,	3	-	compare to region grow

such a bronchovascular pair seems as one hole closed and one hole open which is often called a “signet ring”. There are also veins which do not accompany a bronchus. The segmentation of the vessel trees can be of interest for matching follow-up scans as landmarks to remove false positive (FP) of CAD schemes, for example in the case of lung nodule detection.

The number of studies on pulmonary vessel segmentation is limited. I will present the general vessel segmentation methods are discussed here, since these methods can be directly applied to pulmonary vessel segmentation [50]. The vessel segmentation methods can be divided into different categories, such as pattern recognition techniques, model based approaches, neural network based approaches, and tube-like object detection approaches. Multiple techniques are usually used together to solve the particular segmentation tasks.

Table 2.2: Papers on pattern recognition techniques. The variables in the table include the author name of the paper (Paper), the algorithm (Method), input type, whether the method is multi-scale (Multiscale), the result such as centerlines (Cen.), edges (Ed.), Junctions (Junc.). Whether the method segment the whole tree, whether the method has bifurcation detection (Bi).

Paper	Method	Input type	Mul.	Result			Whole tree	Bi
				Cen.	Ed.	Junc.		
MULTI-SCALE APPROACHES								
Sarwal et al. [51]	MSA	XRA	Y	Y	N	Y	Y	N
SKELETON-BASED APPROACHES								
TOZAKI et al. [52]	SBA	CT	N	Y	N	Y	Y	N
KAWATA et al. [53]	SBA DGBA	CBCT	N	Y	N	Y	Y	N
SORANTIN et al. [54]	SBA MMBA	CT	N	Y	N	N/A	N/A	N
RIDGE-BASED APPROACHES								
BULLITT et al. [55]	RBA SBA	MRA CT	Y	Y	Y	Y	Y	N
Aylward et al. [43]	RBA	MRA CT	Y	Y	Y	Y	Y	N
Zhou et al. [56]	RBA	CT	N	Y	Y	Y	N	Y

A. Pattern recognition techniques

Pattern recognition (PR) aims to classify data (patterns) based either on a priori knowledge or on the statistical information extracted from the patterns. The patterns to be classified are usually the groups of measurements or observations, defining points in an appropriate multidimensional space. Humans are very well adapted to carry out PR tasks. In the vessel extraction domain, PR techniques are concerned with the automatic detection of vessel structures and the vessel features. We divide PR techniques into several categories: (1) multi-scale approaches, (2) skeleton-based (centerline detection) approaches, (3) ridge-based approaches.

In Table 2.2, the various studies on the vessel tree segmentation are presented. The variables in the table include the author name of the paper (Paper), the algorithm (Method), input type, whether the method is multi-scale (Multiscale), the result such as centerline, edges, and junction, whether the method segments the whole tree, and

Table 2.3: Nomenclature of pattern recognition techniques.

DGBA	Differential Geometry-based Approaches.
MSA	Multi-Scale Approaches.
RBA	Ridge-Based Approaches.
SBA	Skeleton Based Approaches.
CBCT	Cone-beam CT
MRI	Magnetic Resonance Imaging.
XRA	X-Ray Angiography.
MRA	Magnetic Resonance Angiogra

whether the method has bifurcation detection (Bi). The nomenclature table of pattern recognition techniques is in Table 2.3.

Multi-scale approaches deal with the segmentation at different image resolutions. This technique has high processing speed. Large structures (large vessels in our application domain) are extracted from low resolution images while fine structures are extracted at high resolution. Second advantage is high robustness. After segmenting the strong structures at the low resolution, the weak structures in the neighborhood of the strong structures can be segmented at higher resolution.

Skeleton-based methods perform the extraction of the centerlines of blood vessel. The vessel tree is developed by connecting these centerlines. Different approaches are used to extract the centerline structure. These methods are: (i) threshold and object connectivity, (ii) threshold followed by a thinning procedure, and (iii) extraction based on graph description. The resulting centerline structure is used for the 3D reconstruction.

Ridge-based methods deal with grayscale images. It generates 3D elevation intensity maps in which intensity ridges approximate the skeleton of the tubular objects from the grayscale images [57]. After generating the intensity map, ridge points are identified as local peaks in the direction of the maximal surface gradient. The ridge points can be obtained by tracing the intensity map from an arbitrary point, along the steepest ascent direction. Ridges are invariant features to affine transformations and can be detected in different image modalities. These properties are exploited in medical image registration [57, 43]. Ridge-based approaches detect skeleton of tubular objects so it

Table 2.4: Papers on model based approaches. The variables in the table include the author name of the paper (Paper), the algorithm (Method), input type, whether the method is multi-scale (Multiscale), the result such as centerlines (Cen.), edges (Ed.), Junctions (Junc.). Whether the method segment the whole tree, whether the method has bifurcation detection (Bi).

Paper	Method	Input type	Multi scale	Result			Whole tree	Bi
				Cen.	Ed.	Junc.		
PARAMETRIC DEFORMABLE MODELS								
MOLINA et al. [58]	PDM	XRA	N	N	Y	N/A	N/A	N
RUECKERT et al. [59]	PDM	MRI	Y	N/A	Y	N/A	N/A	N
Kozerke et al. [60]	PDM	MRI	N	N	Y	N/A	N/A	N
Geiger et al. [61]	PDM	Medical Images	Y	Y	Y	N/A	N/A	N
PARAMETRIC MODELS								
CHAN et al. [62]	PM	XRA	N	N	Y	N/A	N/A	N
KRISSIAN et al. [63]	PM	MRA	Y	Y	N/A	Y	Y	N
BORS et al. [64]	PM	3D vol.	N	Y	Y	N/A	N/A	N
TEMPLATE MATCHING								
SUMMERS et al. [65]	TM MSA	MRA	Y	Y	Y	Y	Y	N
PETROCELLI et al. [66]	TM	XRA	N	Y	N/A	Y	N	N

can be thought of as a specialized skeleton-based approaches.

B. Model based approaches

Model-based approaches apply explicit vessel models to extract the vasculature. We divide model-based approaches into four categories: (1) Deformable models, (2) Parametric models, (3) Template matching.

In Table 2.4, the various studies on vessel tree segmentation are presented. The variables in the table include the author name of the paper (Paper), the algorithm (Method), input type, whether the method is multi-scale (Multiscale), the result such

Table 2.5: Nomenclature of model based approaches.

MSA	Multi-Scale Approaches.
PM	Parametric Models.
PDM	Parametric Deformable Models.
TM	Template Matching.
MRI	Magnetic Resonance Imaging.
MRA	Magnetic Resonance Angiography.
XRA	X-Ray Angiography.

as centerline, edges, and junction, whether the method segments the whole tree, and whether the method has bifurcation detection (Bi). The nomenclature table of model based approaches is in Table 2.5.

Deformable models are divided into two categories: parametric deformable models and geometric deformable models. Parametric deformable models are model-based techniques to find object contours using parametric curves that deform under the influence of internal and external forces. First introduced in [67], active contour models or snakes are a special case of a more general technique of matching a deformable model by means of energy minimization. Physically, a snake is a set of control points, called snaxels, in an image that are connected to each other. Each snaxel has an associated energy that either rises or falls depending upon the forces that act on it. Two forces involved are known as snake’s internal and external forces. Internal forces serve to impose the smoothness constraints on the contour, while external forces pull the snake towards the desired image features such as lines and edges. On the other hand, geometric deformable models use the propagating interfaces under a curvature dependent speed function to model anatomical shapes [68] and [69]. They use the Level Set Method (LSM) approach and adapt it to the shape recognition. The main idea behind the Level Set Method is to represent propagating curves as the zero level set of a higher dimensional function which is given in the Eulerian coordinate system. Hence, a moving front is captured implicitly by the level set function.

Parametric models (PM) approach models the objects of interest parametrically. Tubular objects are modeled as a set of overlapping ellipsoids. Some papers use a

circular vessel model [62]. The parameters of the model used are estimated from the image. Although the elliptic PM can approximate healthy vessels and stenoses, it has difficulties to approximate pathological irregular shapes and vessel bifurcations. [70] employs deformable elliptic model to model irregular vessels and bifurcations.

Template matching plans to identify a structural model (template) in an image. The method uses the template as a context. Thus, it is a contextual method and a top-down approach. In arterial extraction applications, the arterial tree template is usually shown as a series of nodes connected in segments. This template will be deformed to fit the structures in the scene optimally. Stochastic deformation process represented by a Hidden Markov Model (HMM) is a method to achieve the template deformation [71, 66].

C. Neural network based approaches

Artificial neural networks are made up of interconnecting artificial neurons (programming constructs that mimic the properties of biological neurons). Artificial neural networks may be used to gain an understanding of biological neural networks, or to solve artificial intelligence problems without necessarily creating a model of a real biological system. It is widely used in pattern recognition as a classification method. The network is a collection of elementary processor called nodes. Each node takes a number of inputs, performs elementary computations, and generates a single output. The output is a linear function which is the weighted sum of the inputs. These weights are learned through training process and then used in the recognition. A commonly used neural network learning algorithm is called the back-propagation algorithm. Neural networks have been used in many applications. In medical imaging, neural networks are mainly used as a classification method. The neural network system is trained with a set of medical images and the target image is segmented using the trained system. One of the advantages that makes neural networks attractive in medical image segmentation is their ability to use the nonlinear classification boundaries obtained during the training of the network. Another attractive feature is the ability to learn.

In Table 2.6, the various studies on vessel tree segmentation are presented. The variables in the table include the author name of the paper (Paper), the algorithm

Table 2.6: Papers on neural network based approaches. The variables in the table include the author name of the paper (Paper), the algorithm (Method), input type, whether the method is multi-scale (Multiscale), the result such as centerlines (Cen.), edges (Ed.), Junctions (Junc.). Whether the method segment the whole tree, whether the method has bifurcation detection (Bi).

Paper	Method	Input type	Multi scale	Result			Whole tree	Bi
				Cen. line	Ed.	Junc.		
PARAMETRIC MODELS								
Cronemeyer et al. [72]	NNBA	XRA	N	Y	Y	Y	Y	N
Nekovei et al. [73]	NNBA	XRA	N	N	N	Y	N/A	N
Hunter et al. [74]	NNBA PDM	ECG	Y	N/A	Y	N/A	N/A	N
Kottke et al. [75]	NNBA	XRA	N	N	N	Y	Y	N
Shiffman et al. [76]	NNBA	CTA	N	N	N	Y	N/A	N

Table 2.7: Nomenclature of neural network based approaches.

NNBA	Neural net based approach.
PDM	Parametric deformable model.
CTA	CT angiography.
XRA	X-Ray angiography.
ECG	Echocardiography

(Method), input type, whether the method is multi-scale (Multiscale), the result such as centerline, edges, and junction, Whether the method segments the whole tree, and whether the method has bifurcation detection (Bi). The nomenclature table of model based approaches is in Table 2.7.

2.1.4 Lobar segmentation

Lungs are composed of the distinct anatomical compartments called lobes. Humans have two lungs, with the left being divided into two lobes and the right into three lobes. Together, the lungs contain approximately 1500 miles of airways and 300 to 500 million alveoli, having a total surface area of about $75 m^2$ in adults, roughly the

same area as a tennis court [77]. Furthermore, if all of the capillaries that surround the alveoli were unwound and laid end to end, they would extend for about 620 miles. The lobes are separated by fissures. The fissures are thin sheets of tissue and are visible on thin-slice CT. Lobar segmentation and fissure detection are, however, not equivalent: the major and minor fissures can be incomplete but the fissures can be visible [78, 79]. It is important to determine whether a disease affects one or more lobes when lobar resection is considered. Lobe segmentation is also useful in inpatient registration.

There are several strategies to segment the lobes. First, the fissures can be detected directly, by locating sheet-like bright structures in 3D or curve-like structures in 2D slices. Second, the regions containing the lobe borders are almost devoid of larger blood vessels. So, the lobar boundaries can be inferred by vessel segmentation. [80, 81] represented fissure detection. First, a rough estimation of the fissure positions was provided by atlas registration. Subsequently, fissures were shown with ridge detection in 2-D slices. The method can manually provide anchor points. The method was evaluated by comparing computer results with manual results. In a recent paper [82], the vessels were first segmented using a line filter [35]. A set of filters were applied to enhance sheet-like structures in the volumes of interest. Second, the fissures were found by morphological processing. A qualitative evaluation on 20 low-dose scans was given. The previous work shows encouraging results but automatic lobe segmentation is still a challenging unsolved problem, especially in the presence of incomplete fissures and pathology, an issue not specifically addressed in any paper.

2.2 Registration

In computer aided diagnosis system, the data sets acquired by sampling the same scene or object at different times, or from different perspectives, will be in different coordinate systems. Image registration transforms the different data sets to one coordinate system. Registration is necessary in order to be able to compare or integrate the data obtained from different measurements.

Medical image registration (e.g. for data of the same patient taken at different points

in time) often additionally involves nonrigid registration to deal with deformation of the subject due to breathing, etc. Nonrigid registration of medical images can also be used to register a patient's data to an anatomical atlas, such as the Talairach atlas for neuroimaging. Medical image registration is one of the most active research areas in medical image analysis [83, 84, 85]. Many algorithms have been proposed, some of which could be applied to chest CT. Publications on chest CT most often develop nonrigid registration and typically include some dedicated modifications to standard approaches.

There are four kinds of registration of lung scans in CT: (1) registration of CT scan to another scan of the same patient from a different modality, (2) registration of CT scan to a follow-up CT scan of the same patient for effective visual or automatic comparison to detect the interval change and monitor the response to therapy, (3) inpatient registration of scans acquired at a different inspiration level to study ventilation or to extract functional information, and (4) interpatient registration of scans to an atlas to guide segmentations or detect deviations from normal appearance.

[86] is an example of the intermodality registration. PET and CT chest scans were registered with a rigid deformation followed by a nonrigid deformation based on cubic B-splines. Mutual information was applied as a similarity criterion in a hierarchical multiresolution framework with a quasi-Newton optimization algorithm. This method, similar to the system described in [87], is typical of contemporary volume-based nonrigid registration algorithms. Other papers of the intermodality registration used thresholding method to identify the lung contours and chamfer-matching [88], preprocessing to make both images similar in appearance followed by multi-resolution elastic matching based on minimization of the squared difference image [89].

Registration of follow-up scans has the purposes of pairing and comparing nodules [90, 91] or, more generally, displaying similar slices to a radiologist [92]. Some papers apply rigid deformations. [91] determined a rigid alignment based on a small number of automatically identified anatomical landmarks. [93] used an optical flow method. [94] represented hybrid registration scheme that combined feature- and intensity-based approaches which was applied to chest CT scans.

Some papers demonstrated the registration of the scans acquired at different moments of the respiratory cycle. Matching inspiration and expiration scans is challenging because of the substantial, locally varying deformations that take place during breathing. [95] described a system to assess several functional parameters from regional lung volume changes, local changes in air content. Other papers represented radiotherapy applications: correcting for tumor motion is a major challenge in radiotherapy treatment planning. [96] used the popular demons algorithm to validate the use of the active breath control during radiotherapy treatment.

Registration across individuals can use similar methods, but many anatomical landmarks that can be used for inpatient registration are not always available in two scans of different patients. [97] have constructed a human lung atlas as a general tool that can be used for many purposes. [98] showed that atlas registration could be used to pinpoint the approximate location of lobar fissures which was used later for fissure segmentation.

In any application, the registration method is a compromise between computation time and demands for accuracy and robustness. Providing the fast and fully automatic registration with an accuracy comparable to manual indication of corresponding points is still a major challenge, especially in the presence of large deformations, pathology and noise.

2.3 Computerized detection, quantification and classification

Segmentation and registration serve as precursors to the specific image analysis applications. In this section, the compound systems on automated detection, quantification and classification of lung cancers are presented.

2.3.1 Lung cancer: detection of lung nodules

The number of articles about automated nodule detection has roughly doubled each year in recent years. Many of these articles develop methods with a small extension to a previously published method, or a different database is used for testing. If the

Table 2.8: Papers on approaches of detection of lung nodules and false positive reduction. The variables in the table include the author name of the paper (Paper), the false positive reduction algorithm (FP reduction), Data description, the performance.

Paper	FP reduction	Data	Performance
Kanazawa et al. [99]	rule-based	450 screenings, 10 mm, low dose	90% expert findings
Suzuki et al. [100]	massive training ANN	101 scans from 71 patients, 10 mm, low dose	80.3% of expert findings with 4.8 FPs/scan
Brown et al. [101]	-	31 scans, 5-10 mm, normal dose	86% of expert findings with 11 FPs/scan
Lee et al. [102]	new 5 gray-scale features, tuned parameters	20 scans, 10mm, low dose	72.4% of expert findings with 5.5 FPs/scan
Tanino et al. [103]	principal component analysis clustering	39 scans, 10mm	100% with 33 FPs/scan
Saita et al. [104]	new features: relative positions to anatomical structures	12 scans, 2mm, low dose	100% of expert findings with 2.6 FPs/scan

performances in the follow-up paper are not significantly improved from the earlier results, we only present the latest version.

The lung nodule detection systems generally consist of some common steps: (a) image preprocessing; (b) nodule candidate detection; (c) false positive reduction; (d) nodule classification. The image preprocessing step is used to restrict the search space to the lung area and to reduce vessels, airways, noise and image artifacts. There are many methods developed to generate nodule candidates, but there are always many false positives among these candidates. Thus, the next step tries to reduce the number of these false positive (FP) candidates before the more computationally expensive classification step. Even after the classification step, many false positives exist, and much of current research on nodule detection is in fact not focused on the detection part, but on FP reduction instead. Steps (b)-(d) of nodule detection systems will be covered below.

Table 2.8 gives some publications of the different CAD models. If the paper mentions

the false positive reduction scheme in the study description, we put it in the table.

The following techniques have been reported in order to find nodule candidates: multiple gray-level thresholding [105, 106, 107], mathematical morphology [108, 109, 103, 110], genetic algorithm template matching of Gaussian spheres [111, 112], clustering [99, 113, 114, 115], connected component analysis [116, 104], thresholding [117, 118, 119], detection of circles [120], gray-level distance transform [115], and filters enhancing structures [121, 122, 123].

The multiple gray-level thresholding technique are used to find connected components of similar intensity values, and to remove attached vessels. Mathematical morphology contains many image filters: variable N-Quoit filter [108, 103, 124, 125], selective marking and depth constrained cost map [109], top-hat and sieve filter [110]. The used clustering methods differed in clustering technique and in the features used for clustering: [99, 114, 115] presented fuzzy clustering and [113] used k-means clustering on intensities in the original and filtered images.

The following techniques have been reported in order to reduce false positives: the rule-based false positives reduction [126, 127], the Linear Discriminant Analysis (LDA) scheme [127, 128], and the massive training Artificial Neural Network (ANN) scheme [127, 100].

The following techniques have been reported in order to classify the lung nodules: the rule-based or linear classifier [106, 111, 99, 117, 118, 121, 122], template matching [101], nearest cluster [108, 103], Markov random field [124], neural network [110, 129], and Bayesian classifier [112, 130]. The commonly used features for classification were gray-level features, shape descriptions, and spatial and size information.

One recently interested area is nodule matching, a kind of nodule detection. This specific problem pertains to the localization of previously detected nodules in a follow-up scan [101, 106].

With the FDA approval of some commercial CAD systems for nodule detection, it seems that CAD in this field has come to an acceptable performance.

2.3.2 Lung cancer: characterization of lung nodules

The characterization of lung nodules is a dilemma for the radiologist. Most large nodules (diameter ≥ 1 cm) in patients are at high risk for cancer or malignant, however, current CT scanners allow for the detection of small nodules (diameter < 1 cm). Such small nodules are extremely common and the vast majority of them are benign [131]. Follow-up procedures to determine the malignancy are often invasive, and induce risks for the patient [132]. It is very important for patient management to determine as soon as possible whether nodules are malignant.

Several papers have been made to design computer systems that can help estimate the probability of cancer. For the design of such systems, it is obviously of crucial importance to know which characteristics point toward malignancy. This is also important for radiologists, and the subject of clinical research. It is becoming clear that rules of thumb that apply to larger nodules do not always hold for smaller nodules [131, 133, 134, 135, 136].

Clinical variables such as old age, male sex, a history of smoking, a history of cancer, and exposure to certain chemical compounds increases the probability of cancer, while other factors decrease this probability. Bayesian analysis to include this information in the diagnostic process was proposed [137], but applied to nodule characterization in chest radiographs only.

Table 2.9 provides an overview of published studies on nodule characterization. All studies used a combination of features to characterize the size, shape and internal structure of the nodules. In that way, they indirectly encoded radiologists' knowledge about the indicators of malignancy [131, 143, 144]. The presence of fat in a nodule points toward benign hamartoma [133]. The boundary of nodules can be smooth or spiculated. The former points toward benignity, and the latter to malignancy [145, 146].

It is a trend to switch from 2D analysis on thick slices to 3D analysis on thin-slice data and the performance depends heavily on the data. It is interesting to note that in some studies [147], stand-alone CAD systems outperformed radiologists.

Some systems for content-based image retrieval (CBIR) that retrieve similar cases

Table 2.9: Papers on approaches of characterization of lung nodules. The variables in the table include the author name of the paper (Paper), Data description, Features used, Dimension (Dim), Classifier and the result.

Paper	Data	Features	Dim	Classifier	Result
Henschke et al. [138]	14 benign/14 malignant, thick slices	pixel data used directly as features	2,3	ANN	classification system, 89% accuracy, no comparison with radiologist
McNitt-Gray et al. [139, 140]	14 benign/17 malignant, 3 mm slices	semi-automatic segmentation, size, shape, attenuation and a large number of texture features derived from cooccurrence matrices	2	LDC	classification system, 90.3% accuracy, no comparison with radiologist
Kawata et al. [141, 142]	100-200 nodules, thin-slice data	automatic segmentation, histogram analysis, curvature shape measurement	3		the separating power of various combinations of features is investigated; nodules are clustered in five classes

from a database for a given nodule at hand have also been proposed. Display of similar cases with known classification may help radiologists make a diagnosis. Modest improvements in observer performance, when such similar cases were reported in [148].

2.3.3 Lung cancer: nodule size measurements

The size of a nodule correlates with the chance of malignancy. Growth rate is another important indicator. Benign nodules typically have either a very small (1 month, e.g., for inflammation or pneumonia) or a very large doubling time (16 months). The volume doubling time for cancers is typically between 40 and 360 days [133].

For these reasons, nodule segmentation has received considerable attention. Older studies use 2-D outlines, but recent algorithms segment in 3-D. The major industrial vendors currently all provide automatic nodule segmentation in their chest workstations, although they typically require a manually indicated seed point.

It is difficult or impossible to obtain a ground truth for nodule segmentations in real clinical data. Manual outlines, provided by experts, have been used often, but it has been shown that there can be interobserver and intraobserver differences in such outlines [149].

Algorithms can also be evaluated in terms of their reproducibility when a ground truth is absent. Most published algorithms require a manually indicated seed point, and a slightly different seed point should not lead to substantially different segmentation. This has been investigated in several studies [150, 131, 151].

Note also that algorithms that make errors in volume measurements. For example when compared to manual segmentation, it can still be reliable to determine growth rates, if the errors are systematic. The excellent contrast between tissue and air on CT makes segmentation of an isolated solid nodule of a reasonable size a simple task. But difficulties arise when a) the nodule is small; b) the nodule is connected to vasculature or other structures such as the pleura, fissures or abnormalities; c) the nodule is part-solid or nonsolid, in which case it can be difficult to define the boundary; d) the data is noisy (typical for low-dose scans).

Typically, the segmentation of solid nodules is performed by a dedicated algorithm that performs thresholding or region growing while constraining the shape of the grown nodule, or by template matching or in the case of 2-D processing, dynamic programming [152, 153, 154]. In the case of part-solid or nonsolid nodules, these approaches typically fail. Several alternative approaches have been proposed to deal particularly with such nodules [155, 156].

An advanced system for nodule segmentation will likely consist of multiple algorithms, each tailored for a particular type of nodule and attachments and a recipe for choosing the best algorithm for a nodule at hand. Systems that allow more user interaction to correct segmentation errors made by automatic algorithms with a simple

and intuitive user interface could be very valuable in clinical practice and deserve more research. Other future challenges are the automatic correction for inspiration level and the suppression of inaccuracies caused by acquisition noise.

Chapter 3

Novel Contribution of This Thesis Work

3.1 Segmentation of tubular organs

We propose the improved segmentation method of vascular structures and the same method can be applied to segment pulmonary tracheobronchial tree (also called lung airways).

The segmentation of tubular organs (pulmonary tracheobronchial tree or vasculature) of 3D medical images is critical in various clinical applications such as the diagnosis of the vessel stenosis, surgical planning, therapy planning and treatment, and medical image registration. For example, the pulmonary vascular structures can be used as the land marks in tumor resection planning. The detection of vessel bifurcations plays a critical role in clinical practices as well. First, the usual way of handling solid nodules attached to vessels is to use morphological operations, such as opening, to detach nodules from vessels [117]. Vessel bifurcations, however, when repeatedly opened, may exhibit similar shapes as nodules, and thus cause false detection of solid nodule. Bifurcations detection can thus be used to reduce the false positive in detection of solid nodules. Second, atherosclerotic disease at the bifurcation has been widely known as a risk factor for cerebral ischemic episodes and infarction [157].

Although many researchers have developed various methods for vessel extraction from medical images [50], automatic detection of bifurcation points remains a major difficulty. In [158], centerlines are extracted by applying a 3D line-tracing method and the vessel hull is determined by 2D active contours. However, this approach does not handle bifurcation points. In [159, 160], 3D centerlines of tubular structures are extracted based on local extrema of multiscale medialness responses. This method cannot ensure the continuity of the junction detection, which may lead to an incorrect

estimation of vessels. In [161], a vessel enhancement filter based on eigenanalysis is developed and a geodesic path on the isosurface is calculated. Then, a B-spline surface model is used to reconstruct vessels. However, bifurcations are not incorporated in their B-spline surface model. In [43], the effects of initialization, noise, singularities and scale on intensity ridge traversal are evaluated when vessel centerlines are extracted. The advantages of his method are that (1) it results in the most information, such as centerlines, edges and junctions, among other vessel extraction methods; (2) ridges are invariant to affine transformations; (3) ridges can be detected in different modalities; (4) ridges-based method is less sensitive to noise. However, this method only uses recovery heuristics to continue ridge traversal past discontinuities. It uses the optimal-scale selection to coarsely estimate the vessel radii and does not include bifurcation information.

We propose improved ridge-based methods for vessel segmentation by adding radii estimation by spherical deformable model and fully automatic detection of bifurcation points. The detection of bifurcation points ensures the continuity of vessel centerlines. Our first method is based on scan-conversion method [162, 163] and our second method is based on pattern recognition technique called Adaboost [164, 165]. Since medical images contain anatomical structures of various shapes, we first perform a preselection method to identify the region containing the structures of our interest (i.e., vessels) and extract the centerlines of vessels by applying intensity ridge tracing method. These steps are based on the eigenanalysis of the Hessian matrix, which provides an estimation of the elongated direction of vessels as well as cross-sectional planes orthogonal to vessels. While tracing vessels, bifurcation points are automatically detected from the cross-sectional planes by applying scan-conversion method or Adaboost algorithm with specially designed filters. We show that scan-conversion method can be used to detect bifurcation points, but we find that this method has low sensitivity. Then we develop a robust pattern recognition method: Adaboost with steerable filters has a very high success rate and high sensitivity for automatic detection of bifurcation points from cross-sectional planes orthogonal to vessels. We present very promising results of applying our robust method to clinical chest CT image datasets (10 datasets contains 10 GGO

nodules).

3.2 Registration of tubular organs

The registration of tubular organs (pulmonary tracheobronchial tree or vasculature) of 3D medical images is critical in various clinical applications such as surgical planning and radiotherapy. For example, the pulmonary tracheobronchial tree or vascular structures can be used as the landmarks in lung tumor resection planning; the quantifying treatment effectiveness of the radiotherapy on lung nodules is based on the registration of the pulmonary tracheobronchial tree or vessels; the planning inter-patients partial liver transplants use registered contrast injection angiography to create digital-subtraction contrast injection angiography of liver vessels. The bifurcations of the tubular organs play a critical role in clinical practices as well. Inflammation caused by bronchitis alters the airway branching configuration which causes various breathing problems [166]. Atherosclerotic disease at the bifurcation has been widely known as a risk factor for cerebral ischemic episodes and infarction [157]. The bifurcation points (or the branching points) have been chosen to build the validation protocol of the registration methods [167].

Many researchers have developed various methods for registration of tubular organs from medical images. There are three categories of methods for registering images: image to image methods, feature to feature methods, and model to image methods.

Image to image registration methods are volumetric registration methods. They optimize a similarity measure that directly compares voxel intensities between two images. One of the most well known registration methods is to optimize mutual-information similarity measures which are favored for registering tissue images. These voxel matching methods may not be well suited for registering vascular images in which the tissues in the image are poorly differentiated, the predominant features are sparse and the vascular networks may minimally correspond.

Feature to feature registration methods are heavily investigated for tissue images and many methods have been developed for vascular images. The speed and accuracy

of feature to feature registration methods may be limited by the speed and accuracy of the similar features extracted from both images. There is always a strong inverse correlation between feature extraction speed and feature localization accuracy.

Model to image registration methods register models of the tubes in the source image directly with the target images. Centerline traversal is the basis of vessel modeling. In [168], the method extracted an accurate model of the tubes in the source image and multiple target images without extractions could be registered with that model. The registration method registers vascular images with sub-voxel consistency with fast speed and is insensitive to non-rigid deformations. However, this method does not utilize the information in the bifurcation points of the tubular organs. Further, the optimization strategy presents that the number of centerline samples used is further reduced, and the quality of the registration metric is actually improved.

We present a 3D-3D model based rigid registration method of the tubular organs based on the automatically detected bifurcation points of the tubular organs. The improvements of our method are that the information in the bifurcation is added and the minimal centerline samples are used to increase the quality of the registration metric. There are two steps in our approach. We first perform a 3D tubular organ segmentation method to extract the centerlines of tubular organs and radius estimation in both planning and respiration-correlated CT images. This segmentation method automatically detects the bifurcation points by applying Adaboost algorithm with specially designed filters. We then apply a rigid registration method which minimizes the least square error of the corresponding bifurcation points between the planning CT images and the respiration-correlated CT (RCCT) images. Our method has over 96% success rate for detecting bifurcation points. We present very promising results of our method applied to the registration of the planning and respiration-correlated CT images. On average, the mean distance and the root-mean-square error (RMSE) of the corresponding bifurcation points between the respiration-correlated images and the registered planning images are less than 2.7 mm.

3.3 Detection and segmentation of lung GGO nodules

Ground Glass Opacity is defined as hazy increased attenuation within a lung that is not associated with obscured underlying vessels, but with preservation of bronchial and vascular margins [169]. It can reflect minimal thickening of the septal or alveolar interstitium, thickening of alveolar walls, or the presence of cells or fluid filling the alveolar spaces. It can represent active disease such as pulmonary edema, pneumonia, or diffuse alveolar damage. The results of the Early Lung Cancer Action Project, or ELCAP, suggested that nodules with pure (non-solid) or mixed (partially solid) GGO at the thin-section CT are more likely to be malignant than are those with solid opacity [3]. A focal area of pure GGO on the thin-section CT seems to be an early sign of bronchoalveolar carcinoma (BAC) [170]. Pure GGO is useful for differentiating small localized BAC from small adenocarcinomas not having a replacement growth pattern [171]. Early detection and treatment of pure GGO can also improve a prognosis of lung cancer [172].

The appearances of GGO on CT images such as its shape, pattern, and boundary are very different from solid nodules. Thus, algorithms developed for segmentation of solid nodules are most likely to produce inaccurate results when applied to GGO. In [173], a hybrid neural network of three single nets and an expert rule are applied to detect GGO. This method underestimates GGO area due to its improper cut-off of the edges of GGO. Hence, this method may be used only for large GGO and may not be able to obtain accurate segmentation for small GGO. [103] detected GGO using automatic clustering techniques and focused only on GGO detection. The GGO segmentation was not discussed in their work. On the other hand, [156] proposed a GGO segmentation method based on Markov random field and vessel removal method based on shape analysis. However, they only focused on GGO segmentation. The GGO detection was not discussed in their work.

We propose a novel method for automatic detection and segmentation of GGO from CT images. For GGO detection, we develop a classifier by boosting k -Nearest Neighbor (k -NN), whose distance measure is the Euclidean distance between the nonparametric

density estimates of two regions. The detected GGO region is then automatically segmented by analyzing the 3D texture likelihood map of the region. We also present the statistical validation of the proposed classifier for automatic GGO detection as well as the very promising results of automatic GGO segmentation. The proposed method provides a new powerful tool for automatic detection as well as accurate and reproducible segmentation of GGO.

3.4 Detection and segmentation of large lung cancers

The evaluation of therapy response is critical for determining whether a particular treatment is effective on a specific cancer type in a patient. Traditionally, the ways to assess the response are based on measuring size changes of cancer in a transverse image using computed tomography (CT) before and after a treatment [174, 175]. However, the traditional uni-dimensional (maximal diameter of tumor) and bi-dimensional (product of maximal diameter and its perpendicular maximal diameter) measurements can be biased especially when a tumor is not spherical in shape and does not change its shape in a spherical fashion. The preliminary result in a lung cancer study [176] showed that the changes in tumor volume could be determined as early as 3 weeks after a novel chemotherapy, whereas the changes of tumor volume measured in the traditional methods were significantly less sensitive in the same time period. In addition, manual delineation of tumor contours is time-consuming and lacks the reproducibility. Therefore, there is an urgent need for automatic detection and accurate segmentation methods for the volumetric assessment of therapy response.

Unlike small lung nodules, lung cancers to be treated are often large in size, present spiculate edges, and grow against surrounding structures such as the chest wall, the mediastinum, and blood vessels, which make automatic detection and segmentation difficult [176]. Thus, the algorithms developed for automatic detection and segmentation of small solid lung nodules are most likely to fail when applied to large lung cancers [126, 101, 111, 124, 177, 178, 179, 180, 153]. In those studies, larger lung lesions that were attached to the chest wall and mediastinum could be easily and mistakenly excluded from the segmented lungs in which the subsequent lesion detection

would be performed [126, 101, 111, 124]. Also, the existing segmentation algorithms often assumed that small lung nodules would possess spherical shape, which is not adequate for describing large lung cancers. Furthermore, inability to separate a larger lesion from its surrounding structures of similar intensities was another shortcoming of the existing segmentation algorithms.

We propose novel methods for automatic segmentation of lung areas as well as automatic detection and segmentation of large lung cancers from CT images for the purpose of therapy response assessment. The difference between the large lung cancers method and the GGO method is the method used to segment the lung area. In the large lung cancers method, we apply a robust active shape model instead of the thresholding method used in GGO method, to segment the lung area.

First, we propose a robust active shape model for the accurate segmentation of lung areas that are distorted and occluded by large lung cancers. Next, we develop a classifier for the detection of cancers in the segmented lung areas by boosting a k -Nearest Neighbor (k -NN) classifier, whose distance measure is the Euclidean distance between the nonparametric density estimates of two regions. The statistical validation of the proposed classifier is also provided. Finally, the classified cancers are automatically segmented by analyzing 3D texture likelihood maps of the surrounding areas. We present the promising experimental results of our method applied to various clinical data. The proposed methods would provide a new powerful tool for automatic detection as well as accurate and reproducible segmentation of lung cancers for therapy response assessment in lung cancers.

Chapter 4

Methods

4.1 Segmentation

4.1.1 Eigenanalysis of the Hessian matrix

This method is used to segment the tubular organs and remove the vessels overlapped with lung GGO nodules and large lung cancers. Without loss of generality, we assume that vessels appear brighter than the background and their centerlines coincide with the ridges in the intensity profile.

The eigenanalysis of the Hessian matrix is a widely used method for vessel detection [158, 181]. The signs and ratios of the eigenvalues provide the indications of various shapes of interest, as summarized in Table 4.1. Also, the eigenvector corresponding to the largest eigenvalue can be used as an indicator of the elongated direction of vessels.

Given an image $I(x)$, the local intensity variations in the neighborhood of a point x_0 can be expressed with its Taylor expansion:

$$I(x_0 + h) \approx I(x_0) + h^T \nabla I(x_0) + h^T H(x_0) h$$

where, $\nabla I(x_0)$ and $H(x_0)$ denote the gradient and the Hessian matrix of I at x_0 , respectively. Let $\lambda_1, \lambda_2, \lambda_3$ and $\mathbf{e}_1, \mathbf{e}_2, \mathbf{e}_3$ be the eigenvalues and eigenvectors of H such

Table 4.1: Criteria for eigenvalues and corresponding shapes.

Eigenvalues	Shape
$\lambda_1 \leq 0, \lambda_2 \leq 0, \lambda_3 \leq 0$	blob
$\lambda_1 \leq 0, \lambda_2 \leq 0, \lambda_3 \approx 0$	tube
$\lambda_1 \leq 0, \lambda_2 \approx 0, \lambda_3 \approx 0$	plane
$\lambda_1 \leq 0, \lambda_2 \leq 0, \lambda_3 \geq 0$	double cone

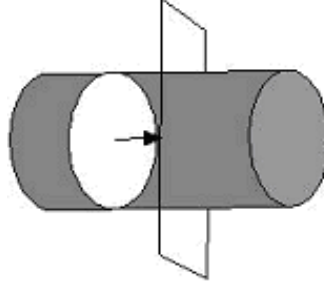


Figure 4.1: Tracing along the direction of the vessel. Figure shows \mathbf{e}_3 and the normal plane defined by \mathbf{e}_1 and \mathbf{e}_2 .

that $\lambda_1 \leq \lambda_2 \leq \lambda_3$ and $|\mathbf{e}_i| = 1$.

Vessel centerline tracing by integrating along the elongated direction of vessels may be less sensitive to image noise [43]. Our vessel tracing starts from a preselected point (and, thereafter, from the point selected in the previous step) and follows the estimated direction of vessels to extract intensity ridges. The intensity ridges in 3D must meet the following constraints:

$$\begin{aligned} \lambda_1 &\ll 0, & \lambda_2 &\ll 0 \\ \mathbf{e}_1 \cdot \nabla I(x) &\approx 0 & \text{and} & \mathbf{e}_2 \cdot \nabla I(x) \approx 0 \end{aligned}$$

Note that the intensity reduces away from the ridge: $\lambda_1/\lambda_2 \approx 0$. Also note that the ridge point must be a local maximum of the plane defined by \mathbf{e}_1 and \mathbf{e}_2 , while \mathbf{e}_3 is normal to the plane. Thus, \mathbf{e}_1 and \mathbf{e}_2 define the cross-sectional plane orthogonal to the vessel, while \mathbf{e}_3 provides the estimate of the vessel direction. Therefore, to trace vessel centerlines, the cross-sectional plane defined by \mathbf{e}_1 and \mathbf{e}_2 is shifting a small step along the direction of the vessel given by \mathbf{e}_3 (Fig. 4.1).

4.1.2 3D texture likelihood map method

This method is used to segment the lung GGO nodules and large lung cancers.

We first extract the ROI (Region Of Interest) surrounding a classified lung GGO nodule. For each voxel in the ROI, we evaluate the likelihood of the voxel belonging to the lung GGO nodule by measuring 3D texture consistency between the lung GGO nodule and a small spherical region (called 3D texon) centered at the voxel.

Let Φ_M be the region of a volumetric sample of a classified lung GGO nodule bounded by a sphere. Using Eq.4.1, we estimate the pdf of the intensity values of the interior of Φ_M , that is, $p_M = P(i|\Phi_M)$. Similarly, let Φ_T be the region of the 3D texon centered at the given voxel in the ROI. Using Eq.4.1, we also estimate the pdf of the intensity values of the interior of Φ_T , that is, $p_T = P(i|\Phi_T)$. To measure the dissimilarity between the two pdfs, we use an information theoretic distance measure called Kullback-Leibler Divergence (KLD) [182]. The Bhattacharya distance (Eq.4.2), which is a symmetrized variation of KLD, between p_M and p_T is:

$$P(i|\Psi_M) = \frac{1}{V(\Psi_M)} \iiint_{\Psi_M} \frac{1}{\sqrt{2\pi\sigma^2}} \exp\left(-\frac{(i - I(y))^2}{2\sigma^2}\right) dy \quad (4.1)$$

$$\begin{aligned} B(p_M \| p_T) &= -\log \rho(p_M \| p_T) \\ &= -\log \int [p_M(i)]^{\frac{1}{2}} [p_T(i)]^{\frac{1}{2}} di \end{aligned}$$

We now evaluate the 3D texture likelihood of the 3D texon at every voxel in ROI. We define this likelihood using ρ , since it increases as the Bhattacharya distance between two distributions decreases. The radius of 3D texons used in our paper is 3 pixels and the model interior texture is mostly homogeneous with some level noise. Thus, it is not necessary to consider the spatial correlation between pixels.

4.1.3 Robust active shape models (RASM)

This method is used to segment the lung area of large lung cancers.

Large lung cancers often grow against surrounding structures, such as the chest wall and mediastinum. Lung areas that are distorted and occluded by such tumors are hard to segment due to the similarity of the intensities between the cancers and the surrounding structures in CT images. We develop a robust method to accurately segment lung areas occluded by large lung cancers by improving the active shape model framework.

An active shape model (ASM) represents the shapes of interest as a Point Distribution Model (PDM) [183]. Then, it constructs a shape space as a set of orthogonal basis \mathbf{P} by applying the Principal Component Analysis (PCA) and finds an optimal shape for a new example of the shapes with PCA reconstruction. Given the shape space \mathbf{P} , the projection \mathbf{C} of a new example shape \mathbf{X} is given as $\mathbf{C} = \mathbf{P}^T d\mathbf{X}$, where $d\mathbf{X} = \mathbf{X} - \bar{\mathbf{S}}$ and $\bar{\mathbf{S}}$ is the mean shape from the aligned shapes of the training set. Based on the projection \mathbf{C} , we can easily find a corresponding shape in the shape space as $\tilde{\mathbf{X}} = \mathbf{P}\mathbf{C} + \bar{\mathbf{S}}$. For simplicity, we denoted $d\tilde{\mathbf{X}} = \mathbf{P}\mathbf{C}$. Since $\bar{\mathbf{S}}$ is constant, the accuracy of $\tilde{\mathbf{X}}$ depends on \mathbf{C} which is related to $d\mathbf{X}$. In many applications, $d\mathbf{X}$ is often optimized with some low-level image features such as the gradient along normal directions to the boundary of an initial shape toward the strongest edge in the image [183].

The ASM method as described above, however, is not suitable for the accurate segmentation of lung areas with large cancers attached on their walls, since the cancers occlude the real boundary of the lung and appear as the strongest edge. To overcome this difficulty, we develop a robust ASM (RASM) based on the robust M-estimator [184]. The goal is to recover the projection \mathbf{C} with the majority of the correct $d\mathbf{X}$ and to restrain the outlier points of $d\mathbf{X}$. Mathematically, it computes \mathbf{C} by minimizing the following robust energy function:

$$\mathbf{E}_{rpca}(\mathbf{C}) = \min_{\mathbf{C}} G(\|\mathbf{dX} - \mathbf{P}\mathbf{C}\|, \sigma) \quad (4.2)$$

where, $G(x, \sigma) = x^2/(x^2 + \sigma^2)$ is the Geman-McClure error function and σ is a scale parameter that controls the convexity of the robust function. The solution for \mathbf{C} can be obtained by an iterative gradient descent search on \mathbf{E}_{rpca} :

$$\mathbf{C}^{(n+1)} = \mathbf{C}^{(n)} + \lambda \Delta \mathbf{C} \quad (4.3)$$

where, λ is a small constant that determines the step size and

$$\Delta \mathbf{C} = \frac{\partial \mathbf{E}_{rpca}}{\partial \mathbf{C}} = -2\mathbf{P}(d\mathbf{X} - \mathbf{P}\mathbf{C}) \frac{\sigma^2}{(\|\mathbf{dX} - \mathbf{P}\mathbf{C}\|^2 + \sigma^2)^2}$$

The iterative process is performed until $\|\mathbf{E}_{rpca}^{(t+1)} - \mathbf{E}_{rpca}^{(t)}\| < \epsilon$, where ϵ is a pre-selected tolerance. Using the robust projection \mathbf{C}^* , we obtain a robust shape in the shape space

as:

$$\tilde{\mathbf{X}} = \mathbf{P}\mathbf{C}^* + \bar{\mathbf{S}}$$

4.2 Reconstruction

4.2.1 Vessel radii estimation by spherical deformable model

This vessel radii estimation is an improvement of the ridge-based method. We use a deformable sphere model to estimate the radii of the vessels for 3D vessel reconstruction.

At each of the detected center points as well as the detected bifurcation points (also called branching points), a deformable sphere is initialized. The position of points on the model are given by a vector-valued, time varying function of the model's intrinsic coordinates \mathbf{u} :

$$\mathbf{x}(\mathbf{u}, t) = (x_1(\mathbf{u}, t), x_2(\mathbf{u}, t), x_3(\mathbf{u}, t))^T = \mathbf{c}(t) + \mathbf{R}(t)\mathbf{s}(\mathbf{u}, t)$$

where, $\mathbf{c}(t)$ is the origin of a noninertial, model-centered reference frame Φ , $\mathbf{R}(t)$ is the rotation matrix for the orientation of Φ , and $\mathbf{s}(\mathbf{u}, t)$ denotes the positions of points on the reference shape relative to the model frame [185]. The reference shape of a sphere is generated in spherical coordinate system with fixed intervals along longitude and latitude directions in the parametric (u, v) domain:

$$\mathbf{e}(u, v) = \begin{pmatrix} x \\ y \\ z \end{pmatrix} = a_0 \cdot \begin{pmatrix} a_1 \cdot \cos u \cdot \cos v \\ a_2 \cdot \cos u \cdot \sin v \\ a_3 \cdot \sin u \end{pmatrix}$$

where, $a_0 \geq 0$ is a scale parameter and $0 \leq a_1, a_2, a_3 \leq 1$ are deformation parameters that control the aspect ratio of the cross section of the sphere. We collected the parameters in $\mathbf{e}(u, v)$ into the parameter vector

$$\mathbf{q}_s = (a_0, a_1, a_2, a_3)^T$$

The velocity of a point on the model is

$$\dot{\mathbf{x}} = \dot{\mathbf{c}} + \dot{\mathbf{R}}\mathbf{s} + \mathbf{R}\dot{\mathbf{s}} = \dot{\mathbf{c}} + \mathbf{B}\dot{\boldsymbol{\theta}} + \mathbf{R}\dot{\mathbf{s}} = [\mathbf{I} \ \mathbf{B} \ \mathbf{R}\mathbf{J}] \dot{\mathbf{q}} = \mathbf{L}\dot{\mathbf{q}}$$

where, $\boldsymbol{\theta}$ is the vector of rotational coordinates of the model, $\mathbf{B} = [\partial(\mathbf{R}s)/\partial\boldsymbol{\theta}]$, $\mathbf{J} = [\partial s/\partial \mathbf{q}_s]$, $\mathbf{q} = (\mathbf{q}_c^T, \mathbf{q}_\theta^T, \mathbf{q}_s^T)^T$, $\mathbf{q}_c = \mathbf{c}$, $\mathbf{q}_\theta = \boldsymbol{\theta}$, and \mathbf{L} is the model's Jacobian matrix that maps generalized coordinates \mathbf{q} into 3D vectors. When initialized near a vessel, the model deforms to fit to the vessel due to the overall forces exerted from the edge of the vessel and comes to rest when \mathbf{q} is found that minimizes the simplified Lagrangian equation of motion:

$$\mathbf{q} = \mathbf{f}_\mathbf{q} = \int \mathbf{L}^T \mathbf{f} du$$

where, $\mathbf{f}_\mathbf{q}$ is the generalized external forces associated with the degrees of freedom \mathbf{q} of the model and \mathbf{f} is the external force exerted from the images. In this method, we use Gradient Vector Flow (GVF) field computed from the images as the external force [186].

4.3 Registration

4.3.1 3D-3D model based rigid registration

The registration is formulated as a 3D-3D model based rigid global deformation. We denote the bifurcation points in the planning CT images as the source points and the corresponding bifurcation points in the respiration-correlated CT images as the target points. Since our tubular organs tracing starts from preselected points, the correspondence between the source points and the target points can be easily determined. The global deformation is a transformation of a point \mathbf{x} in the planning CT image coordinate system into a point \mathbf{x}' in the respiration-correlated CT image coordinate system, that is, $\mathbf{x}' = \mathbf{M} \cdot \mathbf{x}$, where \mathbf{M} is the transformation matrix. Let \mathbf{X}^P and \mathbf{X}^B be the bifurcation points for the planning CT images and respiration-correlated CT images, respectively. The global deformation of \mathbf{X}^P onto \mathbf{X}^B is achieved by finding the parameters of a 3D transformation that minimizes the least square error:

$$\varepsilon = \sum_{i=0}^n \left\| \mathbf{x}_i^B - \mathbf{M} \cdot \mathbf{x}_i^P \right\|^2$$

where, \mathbf{x}_i is the i -th point of a deformable model in the homogeneous coordinate system. We use Levenberg-Marquardt optimization method with the following Jacobian of the

transformation as the metric to provide transformation parameter gradients:

$$\frac{\partial \varepsilon}{\partial \mathbf{M}} = - \sum_{i=0}^n 2(\mathbf{x}_i^B - \mathbf{M} \cdot \mathbf{x}_i^P)(\mathbf{x}_i^P)^T$$

4.4 CAD methods

4.4.1 Vessel and noise suppression with 3D cylinder filters

This method is used to suppress the vessels and noise in the detection of the lung GGO nodules and large lung cancers.

The accuracy of lung GGO nodule detection may be hindered by various structures within a lung. To avoid this difficulty, we first develop a 3D cylinder filter to suppress intensity values of vessels and other elongated structures as well as noise inside a lung, while maintaining lung GGO nodule intensity values intact [121]. The cylinder filter F_{cyl} is defined as:

$$F_{\text{cyl}}(x) = \min_{\theta} \left(\min_{y \in \Omega_{\theta}^x} I(y) \right)$$

where, Ω_{θ}^x is the domain of the cylinder centered at x with orientation θ . F_{cyl} is a hybrid neighborhood proximity filter that produces strong responses to blob-like objects (i.e. GGO or large lesions). We have selected the parameters of F_{cyl} empirically and used a cylinder with the radii of 1, 2 and 3 voxels and the length of 7 voxels at 7 different orientations.

4.4.2 Scan-conversion method

This method is used in the detection of the bifurcations of tubular organs.

Scan-conversion method is a gradient-based ridge point detection method [162]. The gradient of a point generally points toward the ridge and reverses its direction as it crosses the ridge. Consider a line with the orientation passing through only one ridge point (Fig. 4.2(a)). If we consider three continuous points on the line, $p(x-1)$, $p(x)$, $p(x+1)$, and $p(x)$ is on the ridge, the gradients at $p(x-1)$ and $p(x+1)$ must point toward $p(x)$, forming a sign barrier between them. That is, two gradient vectors point head-to-head, forming HH barrier.

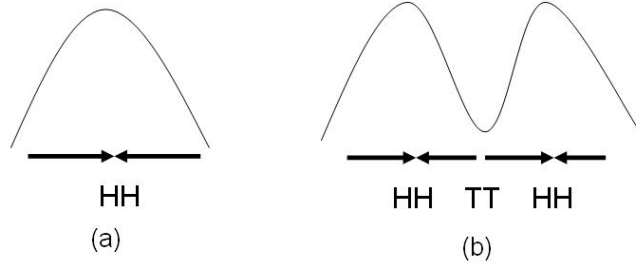


Figure 4.2: HH barriers and TT barriers. (a) in one ridge. (b) in two ridges.

Next, consider a line passing through two ridges located closely (Fig. 4.2(b)). If we consider six continuous points on the line, $p(x-2), p(x-1), p(x), p(x+1), p(x+2), p(x+3)$, and $p(x-1)$ is on the one ridge, while $p(x+2)$ is on the other, then the gradients at $p(x-2)$ and $p(x)$ must point toward $p(x-1)$, forming an HH barrier between them. The gradients at $p(x+1)$ and $p(x+3)$ must point toward $p(x+2)$, also forming an HH barrier. What is more important is the sign variation at $p(x)$ and $p(x+1)$. Since the two ridges are closely located, the gradient at $p(x)$ points toward $p(x-1)$ and the gradient at $p(x+1)$ points toward $p(x+2)$. This forms another type of the sign barrier, called TT barrier, where two gradient vectors point away from each other.

The shape of a vessel without bifurcation in the cross-sectional plane is approximately ellipsoidal. On the other hand, the shape of a vessel with bifurcation appears as two intersecting ellipses (Fig. 4.3).

Note that only one crest exists in the cross-section of a vessel without bifurcation (forming HH barrier), while two crests exist in the cross-section of the vessel with bifurcation (forming both TT and HH barriers) (see Fig. 4.3). We apply a simple scan-conversion algorithm for bifurcation detection using these properties. Given a gradient vector field $\nabla I(x, y) = \langle v_x, v_y \rangle$ around the center of the vessel in the cross-sectional plane, the algorithm scans horizontally ($\theta = 0^\circ$) from left to right and vertically ($\theta = 90^\circ$) from top to bottom. For each scan, we search for TT barriers. Since only the vessel cross-sectional plane with two crests will have TT barriers, they can be used as indicators for bifurcation. We eliminate false positive by set the size of the vessel cross-sectional plane below α and the size of vector field around the mass center of the

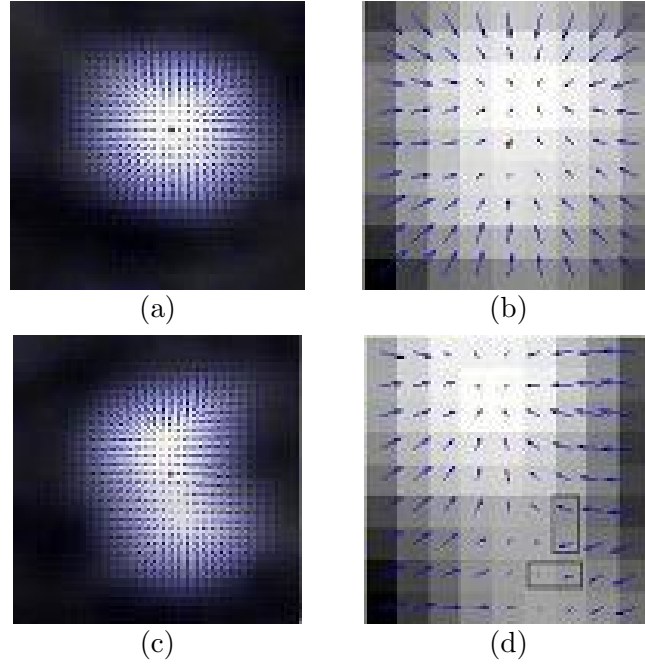


Figure 4.3: The vessel cross-sectional planes without bifurcation (a) and with bifurcation (c). The gradient field only has HH barriers (b), and the gradient field has HH and TT barriers (d). The red point is the mass center. The squares in (d) denote the TT barriers.

vessel-sectional plane below β . The algorithm is in Algorithm 1. Here, we set $\alpha = 32$ voxels and $\beta = 9$ voxels.

4.4.3 Adaboost learning method

This method is used in the detection of the bifurcations of tubular organs.

Boosting is a method for improving the performance of any weak learning algorithm which, in theory, only needs to perform slightly better than random guessing. A boosting algorithm called Adaboost improves the performance of a given weak learning algorithm by repeatedly running the algorithm on the training data with various distributions and then combining the classifiers generated by the weak learning algorithm into a single strong classifier [164, 165]. The proposed method uses Adaboost with specially designed steerable filters for fully automatic detection of bifurcation points.

Algorithm 1 Scan-conversion algorithm

Input: The cross sectional plane A ($m \times n$), Number of TT = 0, position array.
 Calculate the gradient vector field of plane A.
for $i = 1$ to m **do**
 for $j = 1$ to n **do**
 if Find TT barriers **then**
 Save (i,j) in the position array.
 Number of TT ++.
end if
end for
end for
Output: Number of TT and the position array

A. Feature design

We design three types of linear filters to capture the local appearance characteristics: 2D Gaussian filters to capture low frequency information; the first order derivatives of 2D Gaussian filters to capture high frequency information, i.e., edges; the second order derivatives of 2D Gaussian filters to capture local maxima, i.e., ridges [187]. These filters function as weak classifiers for Adaboost.

Let $G = G(\mu_x, \mu_y, \sigma_x, \sigma_y, \theta)$ be an asymmetric 2D Gaussian, where

$$\begin{pmatrix} \mu_x \\ \mu_y \end{pmatrix} = R \times \begin{pmatrix} x - x_0 \\ y - y_0 \end{pmatrix}, \quad R = \begin{pmatrix} \cos \theta & -\sin \theta \\ \sin \theta & \cos \theta \end{pmatrix}$$

and, (σ_x, σ_y) , (x_0, y_0) , and θ are the standard deviation, translation, and rotational parameters of G , respectively. We set the derivatives of G to have the same orientation as G :

$$G' = G_x \cos(\theta) + G_y \sin(\theta)$$

$$G'' = G_{xx} \cos^2(\theta) + 2 \cos(\theta) \sin(\theta) G_{xy} + G_{yy} \sin^2(\theta)$$

From the above equations, we tune x_0 , y_0 , σ_x , σ_y , and θ to generate the desired filters. For a 15×15 sized window, we designed the total of 16,200 filters— $x_0 \times y_0 \times (\sigma_x, \sigma_y) \times \theta = 10 \times 10 \times 3 \times 18 = 5,400$ filters for each of G , G' , and G'' . Some of the filter are shown in Fig. 4.4.

B. Adaboost learning

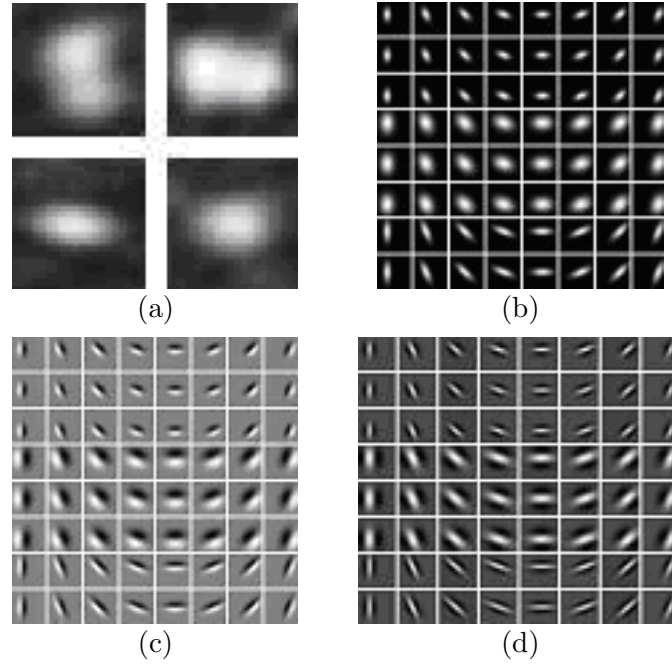


Figure 4.4: (a) The vessel cross-sectional planes with bifurcation (top row) and without bifurcation (bottom row), (b) 2D Gaussian used for low frequency information detection, (c) the first derivatives of Gaussian used for edge detection, and (d) the second derivatives of Gaussian used for ridge detection.

The algorithm is in Algorithm 2. We first normalized the cross-sectional planes obtained from the previous step to the size of the filters and collected an example set containing both positive (i.e., samples with bifurcation) and negative (i.e., samples without bifurcation) examples from the normalized planes. The Adaboost method is used to classify positive training examples from negative examples by selecting a small number of critical features from a huge feature set previously designed and creating a weighted combination of them to use as a strong classifier. Even when the strong classifier consists of a large number of individual features, Adaboost encounters relatively few overfitting problems [188].

During the boosting process, every iteration selects one feature from the entire feature set and combines it with the existing classifier obtained from previous iterations. After a sufficient number of iterations, the weighted combination of the selected features become a strong classifier with high accuracy. That is, the output of the strong classifier is the weighted sum of the outputs of the selected features (i.e., weak classifiers): $S(x) =$

Algorithm 2 Adaboost algorithm

Given training cross-sectional planes $(x_1, y_1), \dots, (x_n, y_n)$ where $y_i \in \{0, 1\}$ for samples without bifurcation (negative samples) and samples with bifurcation (positive samples) respectively.

Initialize weights $w_i = \frac{1}{2m}, \frac{1}{2l}$ for $y_i \in \{0, 1\}$ respectively, where m and l are the number of negatives and positives respectively.

for $t = 1$ to T **do**

1. Normalize the weights, $w_i = \frac{w_i}{\sum_{j=1}^n w_j}$

2. Select the best weak classifier with respect to the weighted error

$$\varepsilon = \min_i \sum w_i |h(x_i) - y_i|$$

3. Update the weights:

$$w_i = w_i \beta^{1-e_i}$$

where $e_i = 0$ if example x_i is classified correctly, $e_i = 1$ otherwise, and $\beta = \frac{\varepsilon}{1-\varepsilon}$

end for

$$\text{The final strong classifier is: } S(x) = \begin{cases} 1 & \sum_{t=1}^T \alpha_t h_t(x) \geq \text{threshold} \\ 0 & \text{otherwise} \end{cases}$$

where $\alpha_t = \log \frac{1}{\beta_t}$

$\sum_t \alpha_t h_t(x)$, where α_t and h_t are weights and outputs of weak classifiers, respectively.

We call S the bifurcation criterion. Adaboost classifies an example plane as a sample with bifurcation when $S > \text{threshold}$ and as a sample without bifurcation when $S < \text{threshold}$.

4.4.4 Boost k -NN

This method is used in the detection of the lung GGO nodules and large lung cancers.

To apply supervised learning framework, we first collected volumetric samples of positive and negative instances. Let Ψ_M be the region of a volumetric sample bounded by a cube. We estimate the probability density function (pdf) of the intensity values of the interior of Ψ_M . We use a nonparametric kernel based method to approximate the pdf. Let $i, i = 0, \dots, 255$, denote the random variable for intensity values. The intensity pdf of Ψ_M is defined by Eq.4.1, where, $V(\Psi_M)$ denotes the volume of Ψ_M , y are the interior voxels of Ψ_M , and σ is the standard deviation of a Gaussian kernel.

For the candidate lung GGO nodules areas isolated, the learning for their classification has a discrete target function of the form $f : \mathcal{R}^n \mapsto \mathcal{V}$, where $\mathcal{V} = \{\oplus, \ominus\}$, with the label \oplus for lung GGO nodules and \ominus for non lung GGO areas. For k -NN,

an instance x is represented as a point in n -dimensional space \mathcal{R}^n by a feature vector $\langle a_1(x), a_2(x), \dots, a_n(x) \rangle$, where $a_i(x) = P(i|\Psi_M)$. The standard Euclidean distance is used as the distance measure between two instance vectors. Given a query instance x_q to be classified, k -NN returns $\hat{f}(x_q)$, as its estimate of $f(x_q)$, which is the most common value of f among the k training instances nearest to x_q :

$$\hat{f}(x_q) = \arg \max_{v \in \mathcal{V}} \sum_{i=1}^k \delta(v, f(x_i))$$

where, x_1, \dots, x_k denote the k instances from the training samples that are nearest to x_q , and $\delta(a, b) = 1$ if $a = b$ and $\delta(a, b) = 0$ otherwise. To obtain an accurate classification, k -NN requires a large training set, which results in slow classification due to the large number of distance calculations. We overcome this difficulty by boosting k -NN [164].

Boosting k -NN combines Adaboost and a variant of the nearest-neighbor classifier. As in [164], boosting k -NN improves the speed of k -NN by reducing the number of prototype instances and thus reducing the required number of distance calculation without affecting the error rate. The weak learner is to use a random set of examples as prototypes chosen according to the distribution provided by the Adaboost algorithm. The details of boosting k -NN is given in [164].

4.5 Evaluation techniques

4.5.1 Receiver Operating Characteristic Curves (ROC) Curve

A ROC curve is a graphical plot of the sensitivity vs. (1 - specificity) for a binary classifier system as its discrimination threshold is varied. This is represented equivalently by plotting the true positives (TP) rate vs. the false positives (FP) rate [22]. Many statistical software can be used to generate ROC curve, such as, Weka and R-stat.

The area under the ROC curve (AUC) is the probability that a classifier will rank a randomly chosen positive instance higher than a randomly chosen negative one. In machine learning field, ROC AUC statistic are often used which can be interpreted as the probability that when we randomly pick one positive and one negative example, the classifier will assign a higher score to the positive example than to the negative.

4.5.2 Overlap rate

Overlap rate is an under merging error measure that describes the difference between the reference image and the segmented image [189]. The discrepancy measure proposed is proportional to the amount by which the regions in the segmented image overlap the regions in the reference image.

4.5.3 Bhattacharya distance

The Bhattacharyya distance measures the similarity of two probability distributions. It is normally used to measure the separability of classes in classification.

For discrete probability distributions p and q over the same domain X , it is defined as:

$$BD(p, q) = -\ln\left(\sum_{x \in X} \sqrt{p(x)q(x)}\right)$$

4.5.4 Mean distance

The mean distance is a quantity measure how close forecasts or predictions are to the eventual outcomes. The mean distance is given by:

$$MeanD = \frac{1}{N} \sum_{i=1}^N d_i$$

where d_i is the distance of the i th sample point, N is the number of sample points.

4.5.5 Root mean square error

The root mean square error (RMSE)) is a measure of the differences between values predicted by a model or an estimator and the values actually observed from the thing being modeled or estimated. These individual differences are also called residuals, and the RMSD serves to aggregate them into a single measure of predictive power.

The RMSD of an estimator $\hat{\theta}$ with respect to the estimated parameter θ is defined as the square root of the mean squared error:

$$RMSE(\hat{\theta}) = \sqrt{E((\hat{\theta} - \theta)^2)}$$

Chapter 5

Tubular Objects Segmentation with Bifurcation Detection in Lung

The flow charts of vessel segmentation method are show in Fig. 5.1 and Fig. 5.2. The difference between these two flow charts is the bifurcation detection method used. The segmentation method of airways which is same as the segmentation method of blood vessels is presented in the Chapter 6.

5.1 Vessel direction estimation

Eigenanalysis of the Hessian matrix method is used to estimate the vessel direction.

5.2 Vessel normal plane extraction

Eigenanalysis of the Hessian matrix method is used to extract the vessel normal planes.

5.3 Vessel bifurcation detection using scan-conversion method

Scan-conversion method is used to detect vessel bifurcations.

5.4 Vessel bifurcation detection using Adaboost learning method

Adaboost learning method is used to detect vessel bifurcations.

5.5 3D reconstruction

Spherical deformable model is used to estimate vessel radii for 3D reconstruction.

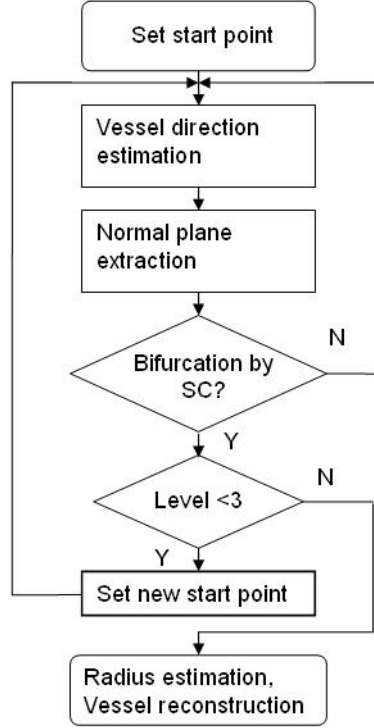


Figure 5.1: The flow chart of vessel segmentation method using scan-conversion method to detect bifurcation points.

5.6 Results

We evaluate the method using 10 CT volumes of lungs. The CT volumes were acquired by multi-slice HRCT scanners with 1 mm slice collimation. The number of slices in each CT scan ranges from 23 to 29 (interpolated to 92 to 116), each of which consists of a 512×512 pixels, with in-plane resolution ranging from 0.57mm to 0.71mm. The CT images are digitally resliced to make cubic voxels and three volumes of interest (VOI). The voxel dimensions are $0.49 \times 0.49 \times 0.49\text{mm}^3$. Two VOIs are $100 \times 100 \times 90$ voxels and one VOI is $50 \times 50 \times 30$ voxels. All experiments are performed on a Dell computer with 1.8GHz processor and 1.5GB of memory. We reconstruct the vessel into the third branching generation which is required by the radiologists. The evaluation of the methods are based on the expert-defined ground truth provided by the radiologists.

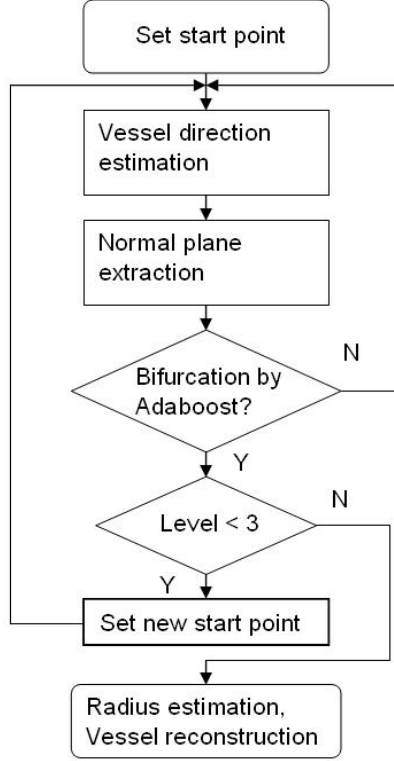


Figure 5.2: The flow chart of vessel segmentation method using Adaboost method to detect bifurcation points.

5.6.1 Qualitative Results

Fig. 5.3 shows further visual validation of our method. We superpose the cross-sectional planes of the detected vessels (Fig. 5.3(a)) and the extracted centerlines (Fig. 5.3(b)) onto the isosurface of the initial images. Fig. 5.4 shows the results of our method applied to complex vascular structures. In Fig. 5.4(a), the extracted centerlines are superimposed on the isosurface of the initial images along with the detected bifurcation points by our Adaboost learning method (shown in blue). Fig. 5.4(b) shows the 3D reconstruction of vessels from the centerlines and bifurcation points in (a). These promising results demonstrate the potential of our method for complex vascular system reconstruction as well as fully automatic bifurcation detection.

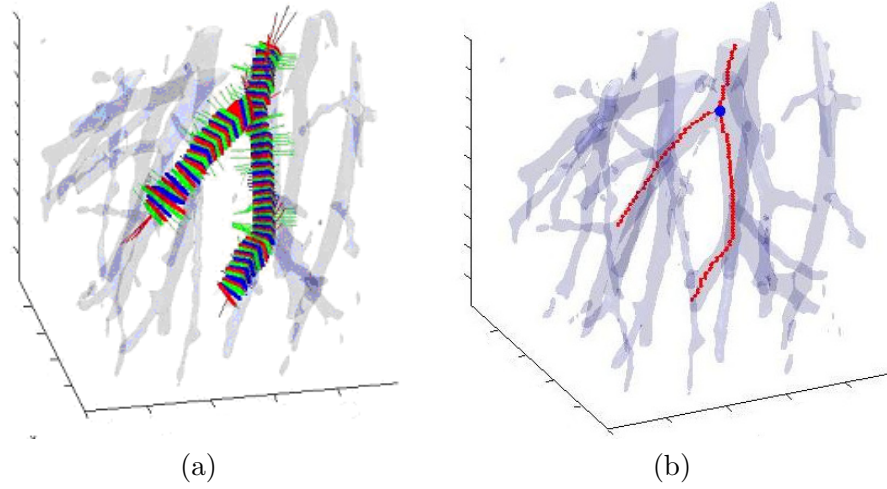


Figure 5.3: Visual validation. (a) cross-sectional planes, (b) centerlines superimposed on an isosurface of the initial image. The blue point in (b) shows the bifurcation point detected.

5.6.2 Quantitative Results

A. Scan-conversion method

The size of the vessel cross-sectional plane is 32×32 pixels and the size of the vector field around the mass center is 9×9 pixels. Totally, 176 cross-sectional planes are derived using cross-sectional planes extraction method. The smallest diameter of vessel in our samples is 6 pixels (approximately 3 mm). There are 40 correct predictions of bifurcation (out of 46) and 130 correct predictions of non-bifurcation (out of 130). So, there is a 3.41% error rate for detecting bifurcation correctly. The results are summarized in Table 5.1. The accuracy is 96.59% for detecting bifurcation. However, the false negative rate is 13.04% which means this method has low sensitivity.

Table 5.1: Results of bifurcation detection using scan-conversion algorithm.

	No bifurcation detected by SC	Bifurcation detected by SC
Bifurcation detected by expert	6	40
No bifurcation detected by expert	130	0

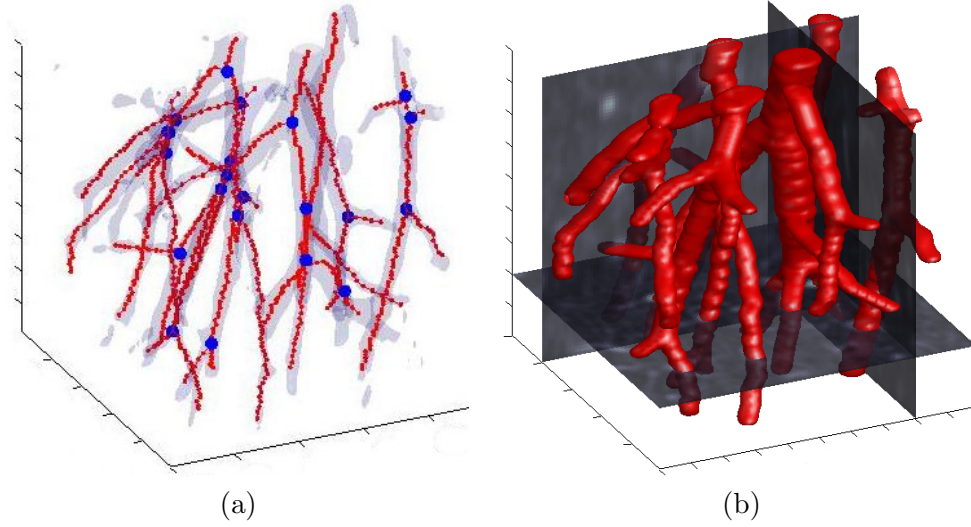


Figure 5.4: Vessel segmentation and bifurcation detection. (a) centerlines superimposed on an isosurface of the initial image, (b) 3D reconstruction of vessels from the graph representation of vessels in (a). Blue points in (a) shows the bifurcation points detected by our method.

B. Adaboost learning method

We first extract 303 cross-sectional planes from the VOIs using cross-sectional plane extraction method. The extracted planes are originally of size 30×30 pixels and are normalized to be the same size as the filter, i.e., 15×15 pixels. The smallest diameter of vessels in our samples is 6 pixels (approximately 3 mm). These example planes contain 150 positive (i.e., with bifurcation) and 153 negative (i.e., without bifurcation) examples. Our method is trained with 100 positive and 100 negative examples and tested on 50 positive and 53 negative examples. We perform bootstrapping to estimate the generalization error of our method, obtaining the mean error rate of 3.16% to 3.63%, which is 95% confidence interval. Fig 5.5(a) shows the result. The accuracy is 96.37% to 96.84% , which is 95% confidence interval, for detecting bifurcation and the ROC curve is presented in Fig. 5.6. The ROC curve is drawn by a free data mining software called Weka and the area under the ROC curve is 0.98.

We also compare Adaboost (20 boosting steps) to other classifiers, i.e., k -Nearest Neighbor classifier with Euclidean distance measure between input images ($k = 3$),

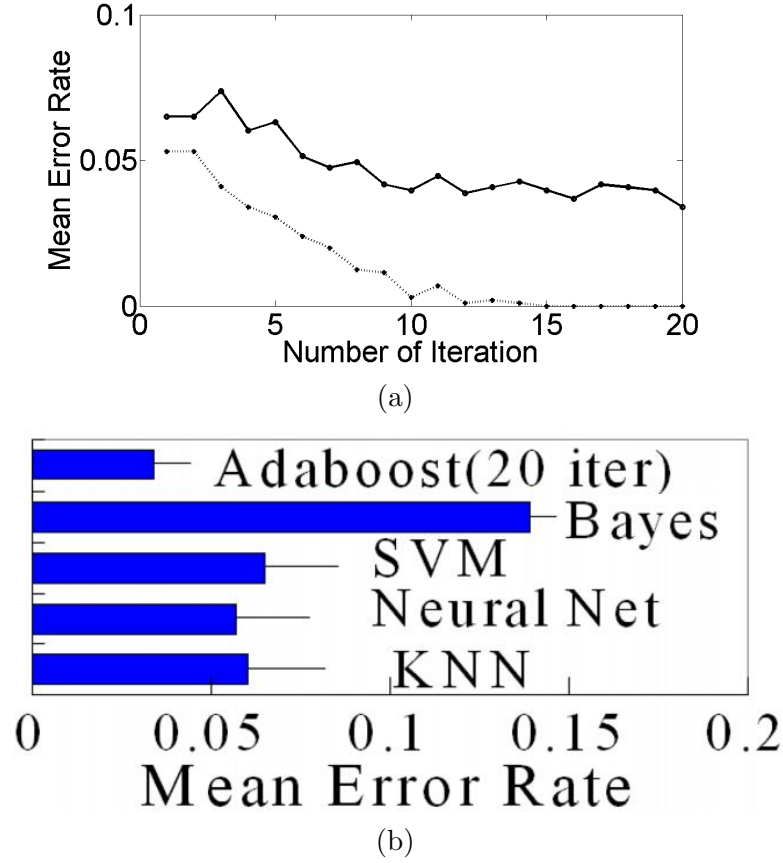


Figure 5.5: Error rate. (a) Mean training and test error curves of Adaboost (training error: lower curve, test error: upper curve), (b) Comparison of the mean error rates of Adaboost and various classifiers

naive Bayes classifier, neural network (1 hidden layer, learning rate of 0.3), and support vector machine (Radial Basis Function (RBF)). Fig. 5.5(b) shows the result. The multiple comparison test ($p = 0.05$) shows that Adaboost is significantly superior to other methods, while k -NN ($k = 3$), neural network (1 hidden layer, learning rate of 0.3), and SVM (RBF) are not significantly different from each other and naive Bayes is significantly inferior to other methods.

For the task of bifurcation detection, the features selected by Adaboost are meaningful and easily interpreted. The first weak feature selected is a second order derivatives of 2D Gaussian filter which is used to capture the ridge. The second weak feature selected is a first order derivatives of 2D Gaussian filter which is used to capture the edge. A normal plane of a vessel bifurcation and two selected weak features are presented in

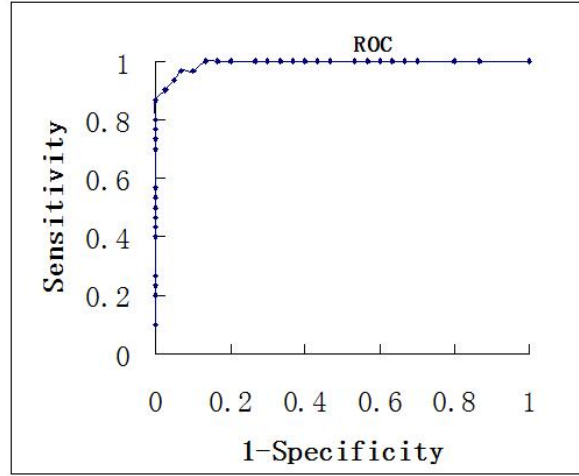


Figure 5.6: ROC curve measures the performance of the Adaboost learning method.

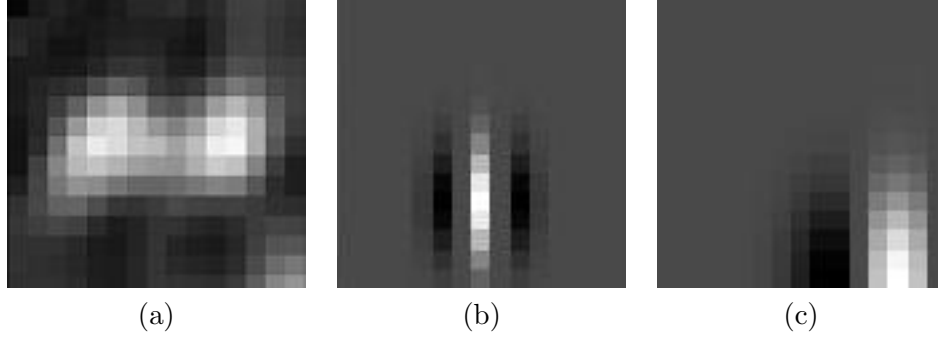


Figure 5.7: A normal plane of a vessel bifurcation and two selected weak features are presented. (a) a normal plane of a vessel bifurcation. (b) the first selected weak feature. (c) the second selected weak feature.

Fig. 5.7.

C. Comparison of two bifurcation detection method

From the result above, the accuracy of the scan-conversion bifurcation detection method is 96.59% in one specific data set and the false negative rate of the scan-conversion method is 13.04% which means this method has low sensitivity.

The accuracy of the Adaboost learning bifurcation detection method is from 96.37% to 96.84%, which is 95% confidence interval (CI) under bootstrapping evaluation method and the Adaboost method can get higher sensitivity by adjusting the threshold.

Chapter 6

Tubular Objects Registration in Lung

The flow chart is in Fig. 6.1.

6.1 Tubular organ direction estimation and normal plane extraction

Eigenanalysis of the Hessian matrix method is used to estimate the vessel direction and extract the normal planes.

6.2 Bifurcation detection using Adaboost

Adaboost learning method is used to detect vessel bifurcations.

6.3 Tubular organs radius estimation for 3D reconstruction

Spherical deformable model is used to estimate vessel radii for 3D reconstruction.

6.4 Tubular organs registration

3D-3D model based rigid registration method is used to register airways.

6.5 Results

We apply our method on clinical lung CT data from 6 different patients. Each patient has one planning CT data set and ten respiration-correlated CT (RCCT) data sets taken in one complete respiratory cycle. They represent CT images at ten different points in the patient's breathing cycle. However, in this chapter, we only use the planning CT data set and the first RCCT data set from each patient. The number of slices in each

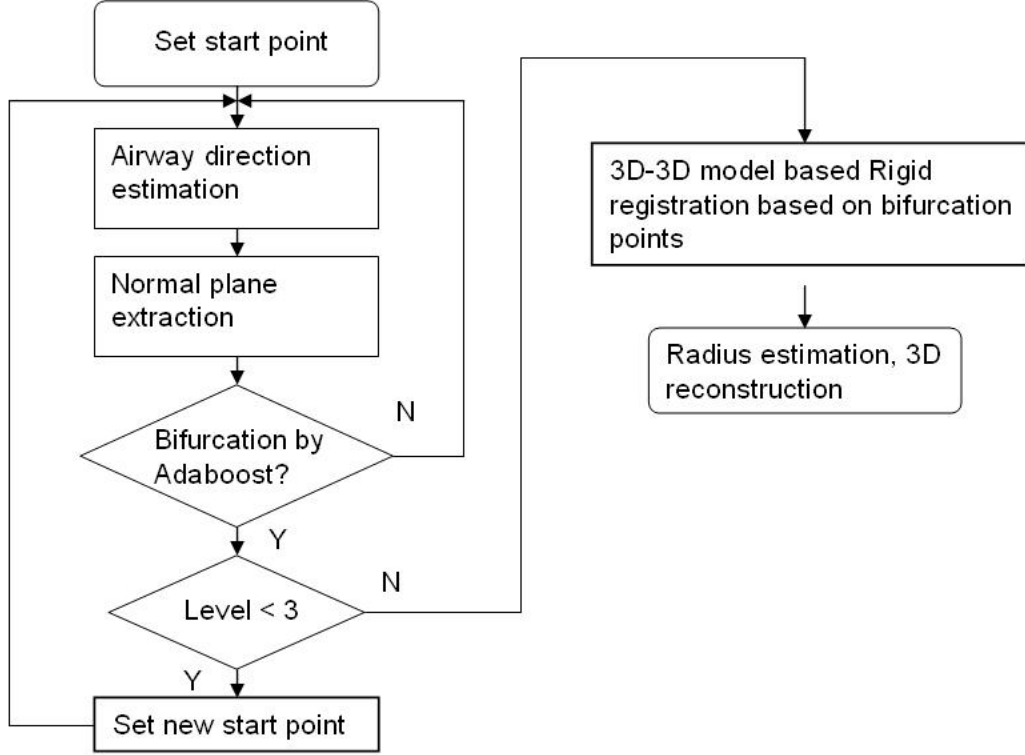


Figure 6.1: The flow chart of airways registration method.

CT scan ranges from 83 to 103 with 2.5mm slice thickness (and also digitally resliced to obtain cubic voxels, resulting in 206 to 256 slices), with size 512×512 pixels, and with in-plane resolution of 0.9mm. All experiments are performed on a PC with 2.0GHz processor and 2.0GB of memory. We reconstruct the airways into the third branching generation which is required by the radiologists. The evaluation of the methods is based on the expert-defined ground truth provided by the radiologists.

6.5.1 Qualitative Results

Fig. 6.2 illustrates further visual validation of our segmentation method applied to the pulmonary tracheobronchial structures. In Fig. 6.2(a), the extracted centerlines are superimposed on the isosurface of the original CT images along with the detected bifurcation points by the Adaboost learning method (shown in blue). Fig. 6.2(b) shows the 3D reconstruction of the pulmonary tracheobronchial tree from the centerlines and bifurcation points in Fig. 6.2(a). Fig. 6.3 shows the registration results between the

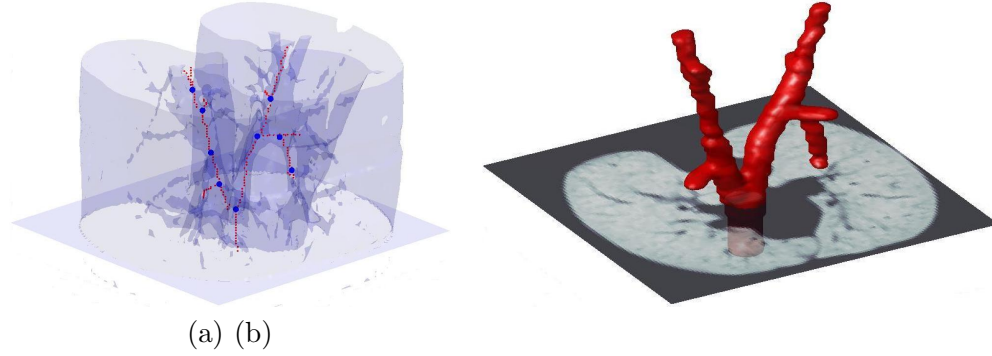


Figure 6.2: Pulmonary tracheobronchial tree segmentation and bifurcation detection. (a) centerlines superimposed on an isosurface of the initial image, (b) 3D reconstruction of pulmonary tracheobronchial tree from the graph representation in (a). Blue points in (a) shows the bifurcation points detected by our method.

planning CT images and the respiration- correlated CT (RCCT) images.

6.5.2 Quantitative Results

We first extract 507 cross-sectional planes from the VOIs using cross-sectional plane extraction method. The extracted planes are originally of size 30*30 pixels and are normalized to be the same size as the filter, i.e., 15*15 pixels. The smallest diameter of bronchi in our samples is 3 pixels. These example planes contain 250 positive (i.e., with bifurcation) and 257 negative (i.e., without bifurcation) examples. Our method is trained with 150 positive and 150 negative examples and tested on 100 positive and 107 negative examples. We perform bootstrapping to estimate the generalization error of our method, obtaining the mean error rate of 3.1% to 4.6%, which is 95% confidence interval, as described in previous section. The accuracy is 95.4% to 96.9% , which is 95% confidence interval, for detecting bifurcation and the ROC curve is presented in Fig. 6.4. The ROC curve is drawn by a free data mining software called Weka and the area under the ROC curve is 0.90.

The results are also summarized in Table 6.1. It shows that, on average, the mean distance and the root-mean-square error (RMSE) of the corresponding bifurcation points between the respiration-correlated images and the registered planning images are

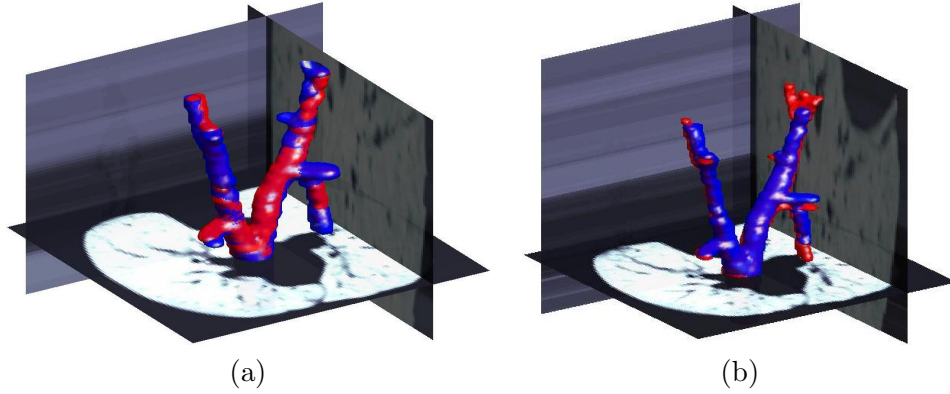


Figure 6.3: Registration results. Blue shows the 3D reconstruction of pulmonary tracheobronchial tree in the registered planning images and red shows 3D reconstruction of pulmonary tracheobronchial tree in the respiration-correlated images.

Table 6.1: Results of the registration method on clinical datasets.

Dataset	Mean distance (mm)	Root mean square error (mm)
Best	1.51	1.63
Worst	3.08	3.38
Average	2.17	2.63

less than 2.7 mm. It shows in the manual registration (ground truth provided by radiologists) that, on average, the mean distance and the root-mean-square error (RMSE) of the corresponding bifurcation points between the respiration-correlated images and the registered planning images are less than 3.0 mm. There are breathing-induced deformations in the tracheobronchial tree, owing to the different amount of lung inflation in the different RCCT data sets. These may partly explain the mean distance and the root-mean-square error (RMSE) in Table 6.1.

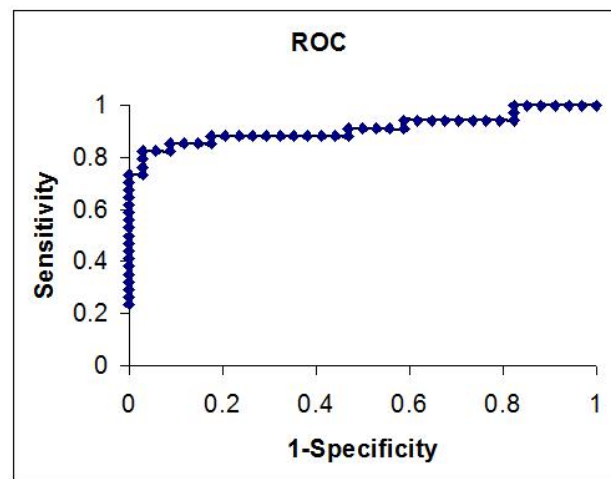


Figure 6.4: ROC curve measures the performance of the Adaboost learning method.

Chapter 7

Lung GGO Nodules Detection and Segmentation

In this chapter, we propose a novel method for automatic detection and segmentation of GGO from chest CT images. The flow chart of our method is show in Fig. 7.1.

7.1 Threshold for lung area segmentation

Grey level thresholding methods are used to segment the lung area from the background in CT images [105, 121].

7.2 Vessel and noise suppression with 3D cylinder filters

3D cylinder filters are used to suppress the vessels and noise. This is because the accuracy of lung abnormalities detection may be hindered by various structures within a lung. To avoid this difficulty, we first develop a 3D cylinder filter to suppress intensity values of vessels and other elongated structures as well as noise inside a lung, while maintaining lung abnormalities intensity values intact [121].

The effect of F_{cyl} is shown in Fig.7.2. In the figure, (b) shows the filter-response volume of F_{cyl} applied to (a). We can see from (b) that vessels and noise are effectively suppressed while GGO remains intact. To isolate candidate GGO regions, i.e., regions of high response values, we apply a simple thresholding to the filter-response volume (Fig.7.2(c)). The threshold value is automatically determined by analyzing the histogram of the filter-response image, as illustrated in Fig.7.3.

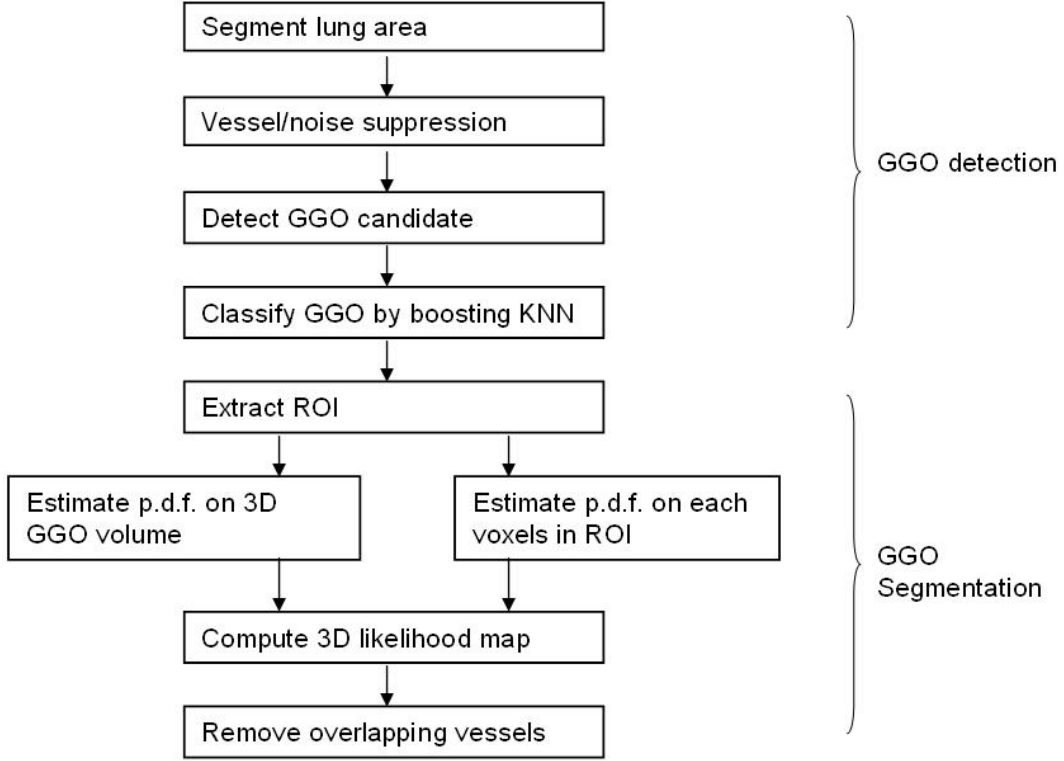


Figure 7.1: The flow chart of GGO detection and segmentation method.

7.3 Detection of GGO

To apply supervised learning framework, we first collected volumetric samples of positive (lung abnormalities) and negative (non lung abnormalities) instances, as shown in Fig.7.4. Boosting k -NN is used to detect GGO. Fig.7.5 shows the typical intensity pdf of positive and negative instances. We can see from the figure that positive and negative instances are well separable using the pdf. For this reason, we use as an instance the intensity pdf of the volumetric samples.

7.4 Segmentation of GGO using nonparametric density estimation

3D texture likelihood map method is used to segment GGO. Fig.7.6(b) shows the 3D texture likelihood map of the volume in (a). The radius of 3D texons used in our paper is 3 pixels and the model interior texture is mostly homogeneous with some level noise. Thus, it is not necessary to consider the spatial correlation between pixels.

7.5 Removal vessels overlapped with lung abnormalities

The eigenanalysis of the Hessian matrix is used to remove vessels overlapped with lung abnormalities. Fig.7.6(c) shows the texture likelihood map after the removal of vessels in (b).

7.6 Results and Discussion

The data sets we used are the same data sets used in vessel segmentation.

7.6.1 Qualitative Results

Fig.7.9 shows the GGO segmentation results overlaid on the original CT images and 3D reconstruction for four GGOs as examples. From the figure, we can see that the surrounding vessels are accurately removed from the GGO segmentation.

7.6.2 Quantitative Results

To test the GGO detection method, we collect 600 volumetric samples, containing 400 training samples and 200 testing samples. The samples are of size $9 \times 9 \times 3$ voxels extracted from the CT volumes. Each sample is converted to an instance vector in \mathcal{R}^{256} , representing its nonparametric density estimate. For the boosted k -NN, we use the standard Euclidean distance as the distance measure between two instances.

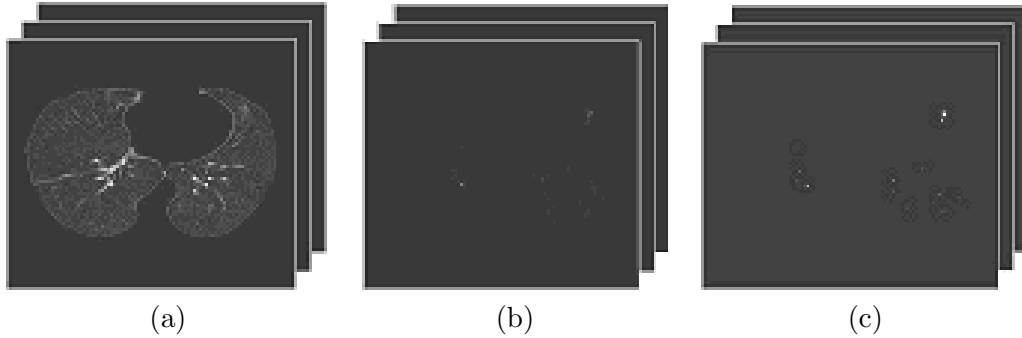


Figure 7.2: Effect of F_{cyl} . (a) Original volume, (b) Volume filtered with F_{cyl} , (c) After thresholding.

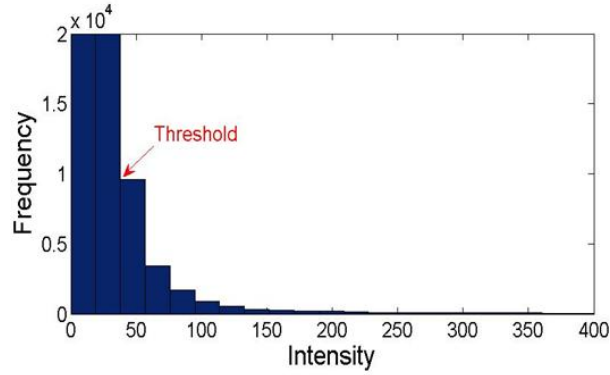


Figure 7.3: Histogram of a cylinder filtered volume.

We perform bootstrapping to estimate the generalization error of our GGO detection method [190]. We train and test the proposed method on bootstrap samples. After 20 steps of boosting, the test error rate converges to 3.70%. The accuracy is 96.3% for classification GGO and the ROC curve is presented in Fig.7.7. The ROC curve is drawn by a free data mining software called Weka and the area under the ROC curve is 0.98.

We also compare the boosted k -NN (20 boosting steps with $k = 3$) to other classifiers, i.e., k -NN classifier ($k = 3$), decision tree, support vector machine (RBF), neural network (1 hidden layer, learning rate of 0.3), and Bayes network. Fig.7.8 summarizes the results. The multiple comparison test ($p = 0.05$) shows that the boosted k -NN and k -NN are significantly superior to other classifiers. Note that, although our purpose for boosting k -NN is not to improve the classification accuracy but rather to speed up the classification process, the results show that boosting k -NN also improves the classification accuracy over k -NN.

We apply the trained GGO classifier to 10 CT volumes containing 10 nodules. The CT volumes were acquired by multi-slice HRCT scanners with 1 mm slice collimation. The number of slices in each CT scan ranges from 23 to 29 (interpolated to 92 to 116), each of which consists of a 512×512 pixels, with in-plane resolution ranging from 0.57mm to 0.71mm. The classifier detects the total of 11 nodules, containing all of the 10 nodules and one false positive nodule.

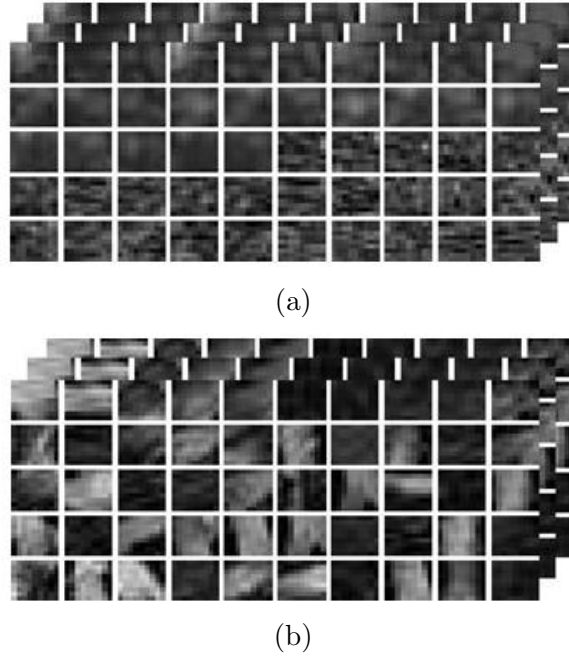


Figure 7.4: Volumetric samples for learning. (a) Positive (GGO) samples, (b) Negative (non GGO) samples.

Table 7.1 compares the greatest diameters, their greatest perpendicular diameters and tumor volumes of the 10 lung GGOs from the results of the manual segmentation by experts and the automatic segmentation by the proposed method. The table shows that the mean relative error of the greatest diameter and its greatest perpendicular diameter are 2.4% and 3.2% and shows that the mean relative error of the tumor volume is 3.2%. We also compare the overlapping ratios of the GGO regions segmented manually and automatically, which range from 87.5% to 95.7%. The mean overlapping ratio is 92.3%.

7.6.3 Discussion

Many texture features that have been described and used [191, 192, 193], including kurtosis, surface curvature, inertia, maximum probability, momentum and gaussian curve fitting. Kurtosis is the extent to which a histogram is peaked. Surface curvature is defined as the rate of change of the slope of the tangent to the surface. Inertia, maximum probability, and momentum are defined as features that present the spatial dependence of gray-scale distributions. Gaussian curve fitting is computed according

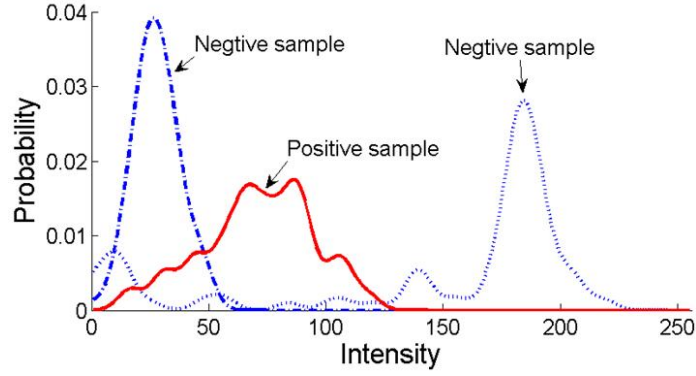


Figure 7.5: Typical probability density functions of positive (solid line, GGO), negative (dash-dot line, typical background), and negative (dotted line, typical vessels) examples.

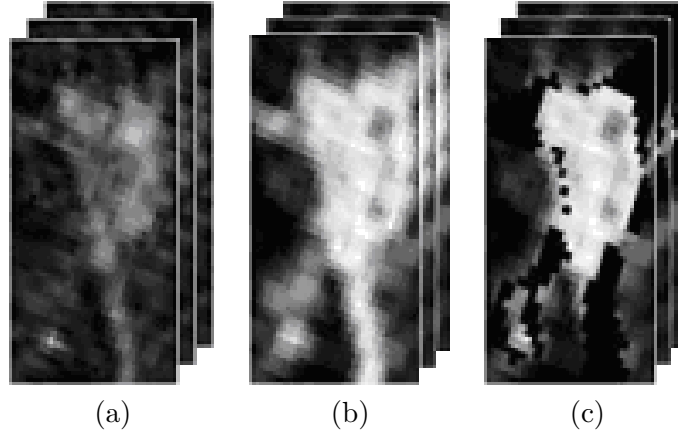


Figure 7.6: GGO segmentation. (a) ROI containing a classified GGO, (b) 3D likelihood map in ROI, (c) 3D likelihood map in ROI after vessel removal.

to the attenuation histogram of pixels within each ROI. Because of the characteristic pixel attenuation distribution of GGO, the use of gaussian curve fitting features enables the differentiation of GGO from background pulmonary parenchyma. In this section, the feature we used is the probability density function (pdf) of the intensity values of the interior of GGO volume. The nonparametric kernel based method is used to approximate the pdf.

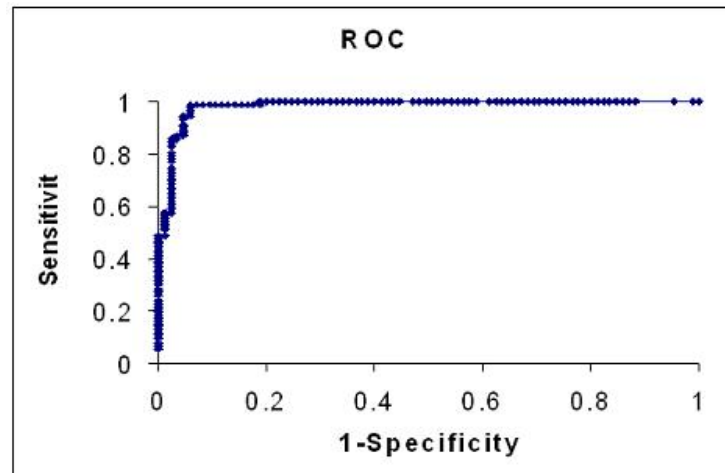


Figure 7.7: ROC curve measures the performance of the Boosted k -NN method for GGO detection.

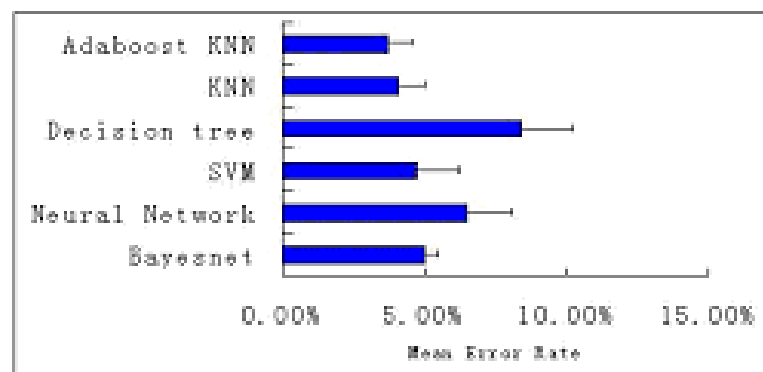


Figure 7.8: Comparison of the mean error rates of various classifiers by bootstrapping.

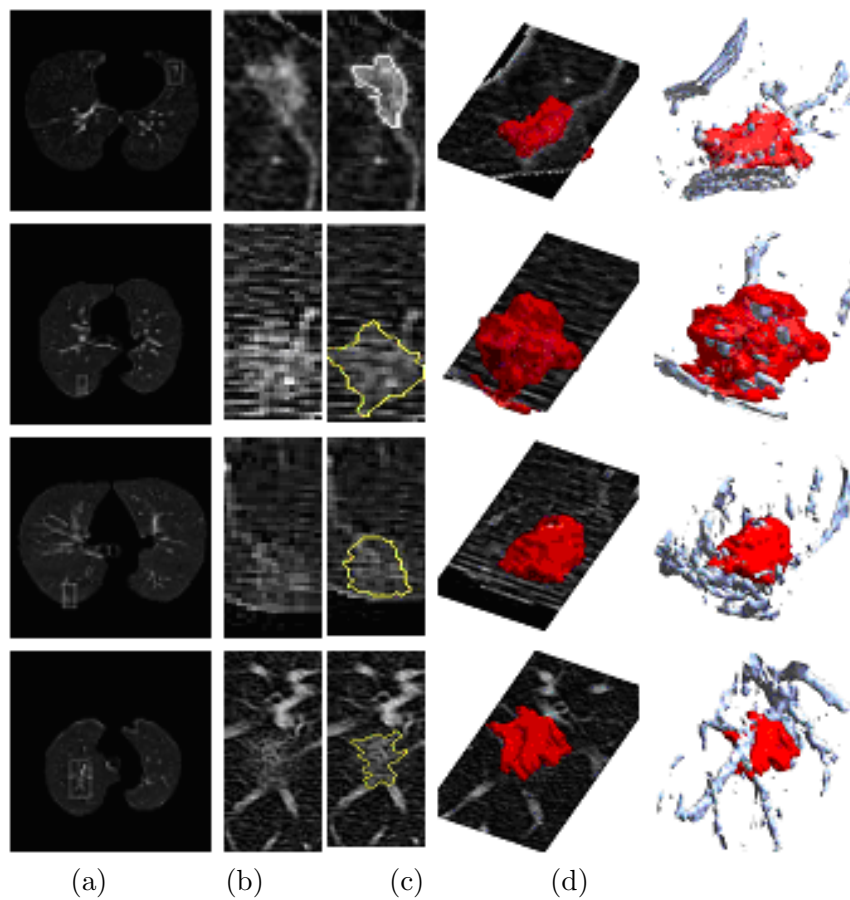


Figure 7.9: GGO segmentation—four segmented GGO nodules are shown. (a) original CT images containing GGO nodules, (b) enlarged GGO areas, (c) segmented GGO, (d) 3D reconstruction of segmented GGO overlaid with original CT images in (a), and (e) 3D reconstruction of segmented GGO with other nearby structures.

Table 7.1: Comparisons. $d1$ and $d2$ are the greatest diameter and its greatest perpendicular distance of each GGO. Vol is the volume of each GGO. Overlap ratio is the volume overlap ratio of the manual segmentation results and automatic segmentation results. Manual and Auto are the measurements on the manual segmentation results and the automatic segmentation results, respectively.

Dataset	d1 (mm)		d2 (mm)		Vol (mm ³)		Overlap Ratio (%)
	Manual	Auto	Manual	Auto	Manual	Auto	
1	17.0	17.6	15.8	16.4	717.6	763.4	91.6
2	15.1	15.8	12.0	12.6	655.4	699.9	94.5
3	15.8	16.4	11.3	11.9	436.1	466.1	91.5
4	13.9	13.8	8.2	7.6	542.6	487.3	94.3
5	10.1	9.5	8.2	7.6	440.8	404.1	90.7
6	34.0	35.3	20.8	21.4	2610.0	2766.52	95.0
7	6.3	5.7	4.4	3.8	85.3	78.8	95.7
8	7.6	6.9	6.3	5.7	218.0	192.0	92.5
9	10.1	9.5	5.7	5.6	201.8	187.3	90.1
10	6.93	6.3	6.3	5.7	167.3	145.5	87.5
mean error (%)	2.4		3.2		3.2		92.3

Chapter 8

Large lung cancers detection and segmentation

In this section, we propose novel methods for automatic segmentation of lung areas as well as automatic detection and segmentation of large lung cancers from CT images for the purpose of therapy response assessment. The flow chart of our method is show in Fig. 8.1. The difference between the large lung cancers method and the GGO method is the method used to segment the lung area. In the large lung cancers method, we apply robust active shape model instead of the thresholding method used in GGO method, to segment the lung area.

8.1 Robust active shape models (RASM) for lung area segmentation

The ASM method is not suitable for the accurate segmentation of lung areas with large cancers attached on their walls, since the cancers occlude the real boundary of the lung and appear as the strongest edge, as illustrated in Fig. 8.2(a) and (b).

Robust active shape models are used to accurately segment lung areas occluded by large cancers. The result of this process is illustrated in Fig. 8.2(c), where the lung area occluded by a large lesion is accurately segmented.

8.2 Detection of large lung cancers

In this section, we present a novel method for automatic detection of large lung cancers from the segmented lung areas. The method is based on 3D texture analysis using a machine learning framework, i.e., boosting the k -NN classifier. However, the accuracy of the detection may be hindered by various structures within a lung. Thus, we first apply a 3D cylinder filter to suppress the intensity values of vessels and other elongated

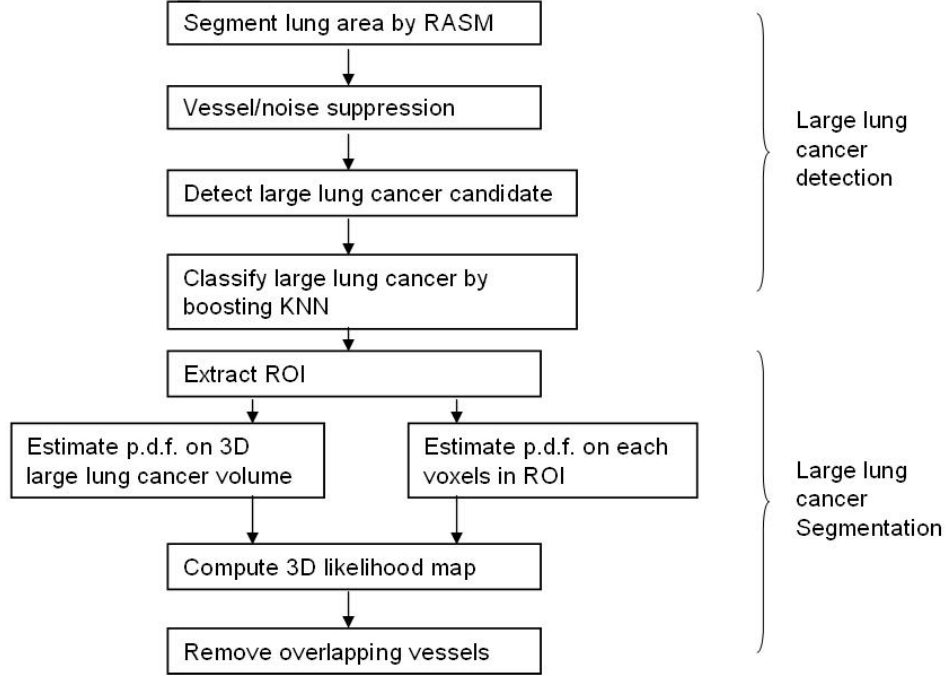


Figure 8.1: The flow chart of large lung cancers detection and segmentation method.

structures as well as noise inside a lung, while maintaining the intensity values of large lung cancers intact [121, 194].

In Fig. 8.3(a) and (b), we can see that vessels and noise are effectively suppressed while the large lung cancers remains intact. After the filtering, we isolate the candidate regions for large lung lesions by simple thresholding (Fig. 8.3(c)). The threshold value is automatically determined by analyzing the histogram of the filter response image [121]. Each candidate region is then classified with a learning framework described below.

8.3 Segmentation of large lung cancers

We now segment the classified large lung cancers. Because of the hazy appearance and irregular shape of large lung cancers and the large overlap of intensity values between large lung cancers and surrounding vessels, simple thresholding and contour based segmentation method do not provide accurate segmentation. The proposed method involves the analysis of a 3D texture likelihood map using a nonparametric density estimation.

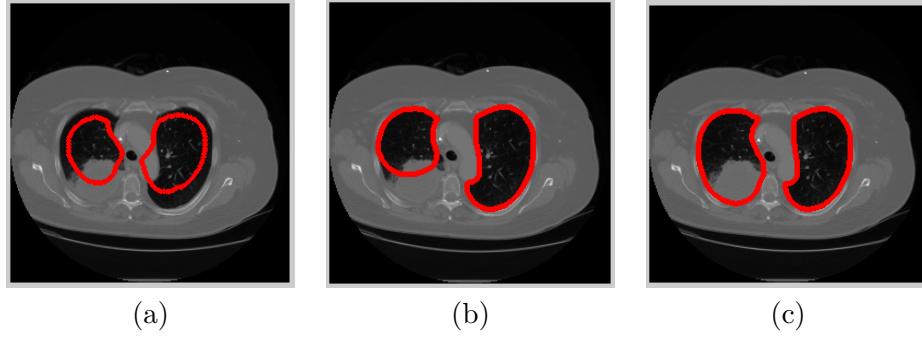


Figure 8.2: The segmented lung area using RASM. Red points are active shape model and green lines are the connected contour. (a) Large cancers attached to the chest wall and mediastinum (large red circle) and the initialization of the ASM, (b) ASM finding the false boundary of lung, and (c) RASM finding the correct boundary of lung and the large white area in the left lung is a large lung cancer.

8.4 Removal vessels overlapped with large lung cancers

The eigenanalysis of the Hessian matrix is used to remove vessels overlapped with large lung cancers.

8.5 Results

We evaluate the method using 10 chest CT images containing 16 large lung cancers. The CT volumes were acquired by multi-slice HRCT scanners with 1 mm slice collimation. The number of slices in each CT scan range from 44 to 69 (interpolated to 130 to 205), each of which consists of a 512×512 pixels, with in-plane resolution 0.82mm. The CT images are digitally resliced to make cubic voxels and three volumes of interest (VOI). All experiments are performed on a Dell computer with 1.8GHz processor and 1.5GB of memory. The evaluation of the methods are based on the expert-defined ground truth provided by the radiologists.

8.5.1 Qualitative Results

Fig. 8.4 illustrates four representative cases of the segmented large lung cancers. In the figure, the 3D reconstruction of the segmented 3D large lung cancers (middle and bottom row) as well as their 2D projections on one of the slices (top row) are shown.

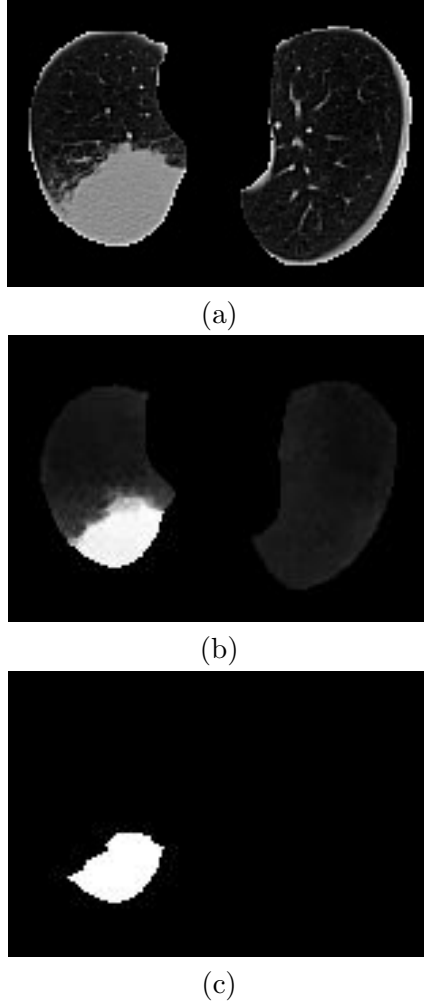


Figure 8.3: Effects of F_{cyl} (only one slice from the whole volume is shown). (a) Original volume, (b) Volume filtered with F_{cyl} , and (c) Volume after thresholding.

From the figure, we can also see that the surrounding vessels are accurately removed from the large lung lesions segmented.

8.5.2 Quantitative Results

To test the proposed machine learning method, we collect 500 volumetric samples, containing 300 training samples and 200 testing samples, from 4 training clinical chest CT images. The samples are of size $15 \times 15 \times 3$ voxels from the CT volumes. Each sample is converted to an instance vector in \mathcal{R}^{256} , representing its nonparametric density estimate. For the boosted k -NN, we use the standard Euclidean distance as the

Table 8.1: Comparisons. $d1$ and $d2$ are the greatest diameter and its greatest perpendicular distance of each tumor. Vol is the volume of each tumor. Overlap ratio is the volume overlap ratio of the manual segmentation results and automatic segmentation results. Manual and Auto are the measurements on the manual segmentation results and the automatic segmentation results, respectively.

Dataset	d1 (mm)		d2 (mm)		Vol (mm ³)		Overlap Ratio (%)
	Manual	Auto	Manual	Auto	Manual	Auto	
1	95	94	37	36	9676	9043	92.5
2	74	73	35	33	13357	12237	90.2
3	84	83	25	24	12704	11753	91.2
4	34	35	32	33	1643	1819	93.6
5	21	20	16	16	278	254	92.1
6	13	13	11	11	305	291	92.5
7	15	16	13	13	462	503	90.0
8	51	52	18	18	2152	2228	91.6
9	21	20	12	12	258	235	82.2
10	21	20	19	18	1402	1226	97.3
11	7	7	7	6	61	57	80.9
12	68	67	59	58	5988	5583	94.3
13	36	37	27	28	6268	6783	91.4
14	22	23	13	13	291	320	88.3
15	27	26	17	16	657	591	95.6
16	39	38	33	32	4583	4212	91.6
mean error (%)	2.8		2.2		8.4		90.9

distance measure between two instances. We perform bootstrapping to estimate the generalization error of our large lesion detection method [190]. We train and test the proposed method on bootstrap samples. After 20 steps of boosting, the mean error rate converges to 3.50%. The accuracy is 96.5% for classifying large lung cancer and the ROC curve is presented in Fig.8.5. The ROC curve is drawn by a free data mining software called Weka and the area under the ROC curve is 0.99.

We apply the trained classifier to all 10 CT volumes containing 16 large lung cancers. The CT volumes are acquired by multi-slice HRCT scanners with 5mm slice collimation. The number of slices in each CT scan ranges from 44 to 69 (and digitally resliced to obtain cubic voxels, resulting in 130 to 205 slices), each of which are of size 512×512 pixels, with in-plane resolution of 0.82mm. The classifier detects all 16 lesions successfully with no false negatives (Fig. 8.4). However, it also detects 2 false positive

lesions, which the trained radiologists classify as atelectases.

Table 8.1 compares the greatest diameters, their greatest perpendicular diameters and tumor volumes of the 16 lung cancers from the results of the manual segmentation by experts and the automatic segmentation by the proposed method. The table shows that the mean relative error of the greatest diameter and its greatest perpendicular diameter are 2.8% and 2.2% and shows that the mean relative error of the tumor volume is 8.4%. We also compare the overlapping ratios of the tumor regions segmented manually and automatically, which range from 80.9% to 97.3%. The low overlapping ratios are resulted from the cases in which the cancers are heavily occluded by blood vessels, where the expert radiologists also find difficulty. The mean overlapping ratio is 90.9%. These results demonstrate the potential of our method to correctly segment occluded lung areas as well as the accuracy of the classification and segmentation of the large lung cancers. These results demonstrate the potential of our method to correctly segment occluded lung areas as well as the accuracy of the classification and segmentation of the large lung cancers.

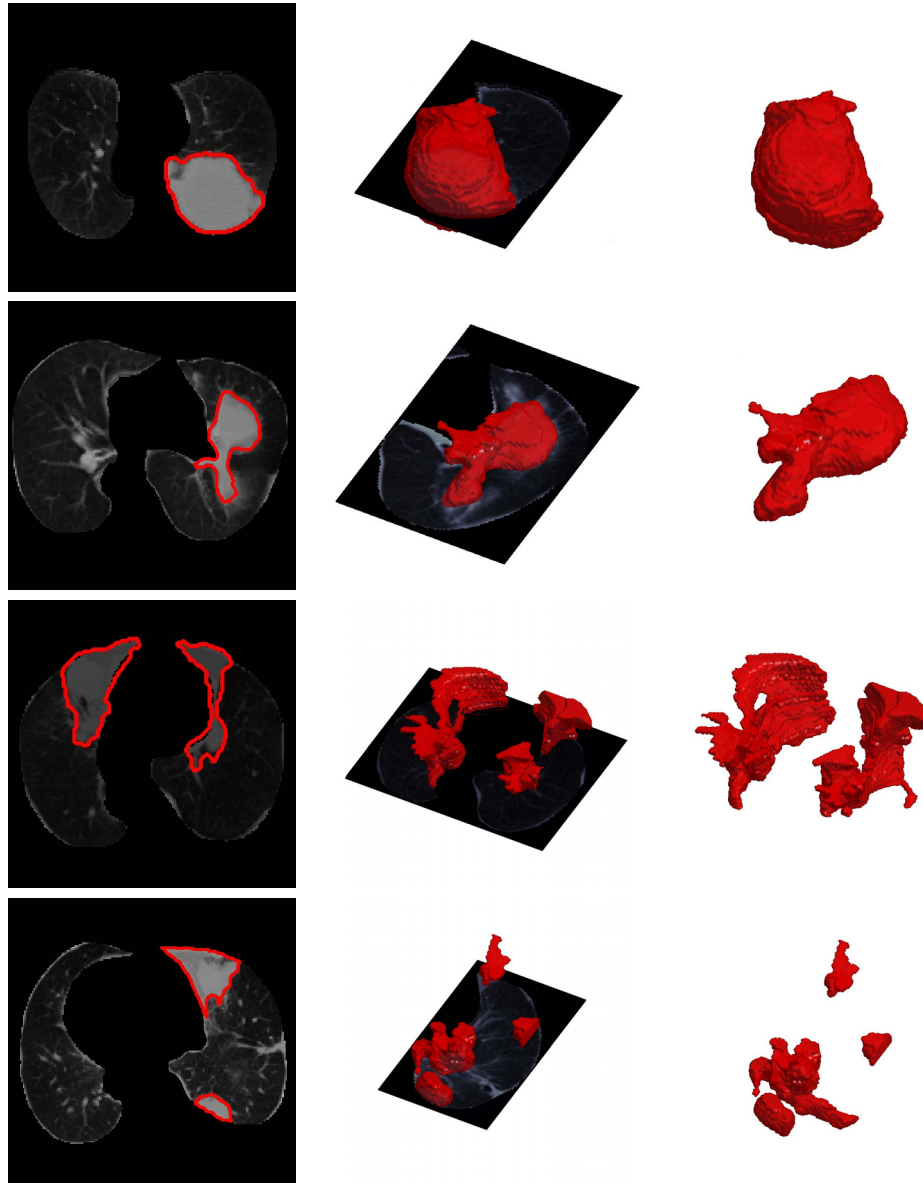


Figure 8.4: Results. Segmented large lung lesions projected onto a slice (left) and corresponding 3D lesions (middle and right).

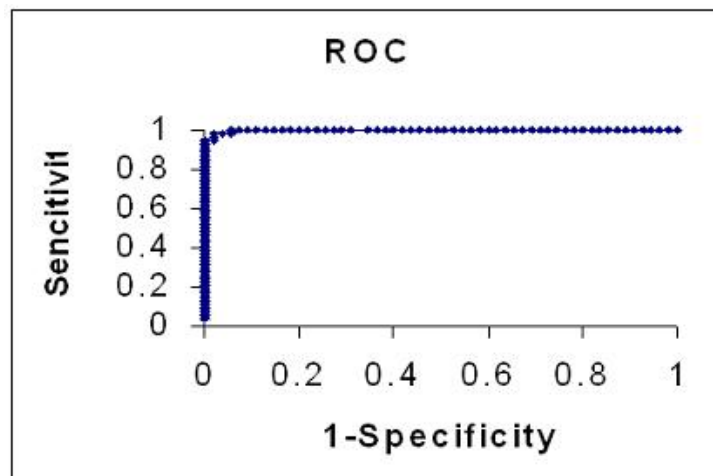


Figure 8.5: ROC curve measures the performance of the Boosted k -NN method for large lung cancer detection.

Chapter 9

Concluding Remarks and Future Work

In this chapter, the main conclusions and results that have been derived during the thesis work are summarized, as well as future tasks in the image analysis of non-rigid registration and tumor motion on CT are proposed.

- We have described an improved ridge-based methodology for segmentation of tubular organs. The novel contributions of the methodology are that the radii of tubular organs are estimated by spherical deformable model and the bifurcations of tubular organs are fully automatic detected by scan-conversion method or Adaboost learning method. We also present very promising results of applying our method to clinical chest CT image datasets (10 datasets contains 10 GGO nodules).

- We have presented a 3D-3D model based rigid registration methodology for the tubular organs registration based on the automatically detected bifurcation points of the tubular organs. The contributions of our method are that the information of the bifurcations is added and the minimal centerline samples are used to increase the quality of the registration metric. We present very promising results of our method applied to the registration of the planning and respiration-correlated CT images.

- We have proposed novel methodologies for the automatic detection and segmentation of lung GGO nodules and large lung cancers from chest CT images. We develop classifiers by boosting k-Nearest Neighbor in the detection and the detected ROI region is then automatically segmented by analyzing the 3D texture likelihood map of the region. We also present the statistical validation of the proposed classifier for automatic detection as well as the very promising results of automatic segmentation.

- The proposed rigid registration method is considered to be a preliminary stage which minimizes the least square error of the corresponding bifurcation points between

the planning CT images and the respiration-correlated CT (RCCT) images. The intensity information of the images are not considered in this process. We have some preliminary ideas to develop a deformable registration method on CT. This method will combine both rigid and non-rigid transformations and the physical structure and properties of the vessels will be taken into account to drive the registration process.

- Novel methods will be developed for diagnosis of lung diseases on 4D RCCT. Information on the extent of tumor motion, such as appropriate margins assignment in radiotherapy, is often difficult to obtain with standard fluoroscopy. However, 4D RCCT can be used to produce three-dimensional image sets at multiple phases. We will investigate the characteristics of lung tumor motion as measured with 4D RCCT.

References

- [1] American Cancer Society: Cancer Facts and Figures. Atlanta: American Cancer Society (2006)
- [2] American Cancer Society: Breast Cancer Facts & Figures. Atlanta: American Cancer Society (2005-2006)
- [3] Henschke, C., Yankelevitz, D., Mirtcheva, R.: CT screening for lung cancer: frequency and significance of part-solid and nonsolid nodules. *Am. J. Roentgenol.* **178** (2002) 1053–1057
- [4] Kalender, W.: Computed Tomography: Fundamentals, System technology, Image quality, Applications. Hoboken, NJ: Wiley (2000)
- [5] Natterer, F.: The Mathematics of Computerized Tomography (Classics in Applied Mathematics vol. 32). Philadelphia, PA: Soc. for Industrial & Applied Math (2001)
- [6] Kak, A.: Principles of Computerized Tomographic Imaging (Classics in Applied Mathematics vol. 33). Philadelphia, PA: Soc. for Industrial & Applied Math (2001)
- [7] Robb, W.: Perspective on the first 10 years of the ct scanner industry. *Academic Radiology* **10** (2003) 756–760
- [8] Pugatch, R., Faling, L.: Computed tomography of the thorax: a status report. *Chest* **80** (1981) 618–626
- [9] Aziz, Z., Padley, S., Hansell, D.: Ct techniques for imaging the lung: recommendations for multislice and single slice computed tomography. *European Journal of Radiology* **52** (2004) 119–136
- [10] Prokop, M., Galanski, M., Van Der Molen, A., Schaefer-Prokop, C.: Spiral and multislice computed tomography of the body. Thieme (2001)
- [11] Minna, J.: Harrison's Principles of Internal Medicine. McGraw-Hill (2004)
- [12] Vaporciyan, A., Nesbitt, J., Lee, J.: Cancer Medicine. B C Decker (2000)
- [13] Gorlova, O., Weng, S., Zhang, Y.: Aggregation of cancer among relatives of never-smoking lung cancer patients. *International Journal of Cancer* **121** (2007) 111–118
- [14] Hackshaw, A., Law, M., Wald, N.: The accumulated evidence on lung cancer and environmental tobacco smoke. *British Medical Journal* **315** (2007) 980–988

- [15] Catelinois, O., Rogel, A., Laurier, D.: Lung cancer attributable to indoor radon exposure in france: Impact of the risk models and uncertainty analysis. *Environmental Health Perspectives* **114** (2006) 1361–1366
- [16] O'Reilly, K., McLaughlin, A., Beckett, W., Sime, P.: Asbestos-related lung disease. *American Family Physician* **75** (2007) 683–688
- [17] Kabir, Z., Bennett, K., Clancy, L.: Lung cancer and urban air-pollution in dublin: a temporal association? *Irish Medical Journal* **100** (2007) 367–369
- [18] Coyle, Y., Minahjuddin, A., Hynan, L., Minna, J.: An ecological study of the association of metal air pollutants with lung cancer incidence in texas. *Journal of Thoracic Oncology* **1** (2006) 654–661
- [19] Chiu, H., Cheng, M., Tsai, S.: Outdoor air pollution and female lung cancer in taiwan. *Inhalation Toxicology* **18** (2006) 1025–1031
- [20] Gonzalez, R., R.E., W.: *Digital Image Processing*. New York, NY: Addison-Wesley publishing company (2002)
- [21] Bishop, C.: *Neural Networks for Pattern Recognition*. Oxford, UK: Oxford University Press (1995)
- [22] Duda, R., Hart, P., Stork, D.: *Pattern Classification*. New York, NY: John Wiley and Sons (2001)
- [23] Armato, S., Sensakovic, W.: Automated lung segmentation for thoracic ct. *Academic Radiology* **11** (2004) 1011–1021
- [24] Brown, M., McNitt-Gray, M., Mankovich, N., Goldin, J., Hiller, J., Wilson, L., Aberle, D.: Method for segmenting chest ct image data using an anatomical model: Preliminary results. *IEEE Transactions on Medical Imaging* **16** (1997) 828–839
- [25] Hu, S., Hoffman, E., Reinhardt, J.: Automatic lung segmentation for accurate quantitation of volumetric x-ray ct images. *IEEE Transactions on Medical Imaging* **20** (2001) 490–498
- [26] Leader, J., Zheng, B., Rogers, R., Sciurba, F., Perez, A., Chapman, B., Patel, S., Fuhrman, C., Gur, D.: Automatic lung segmentation for accurate quantitation of volumetric x-ray ct images. *Academic Radiology* **10** (2003) 1224–1236
- [27] Silva, A., Silva, J., Santos, B., Ferreira, C.: Fast pulmonary contour extraction in x-ray ct images: A methodology and quality assessment. In: *SPIE*. Volume 4321. (2001) 216–224
- [28] Li, B., Reinhardt, J.: Automatic generation of 3-d shape models and their application to tomographic image segmentation. In: *SPIE*. Volume 4322 of *Medical Imaging*. (2001) 311–322
- [29] Zhou, J., Chang, S., Metaxas, D., Zhao, B., Ginsberg, M., Schwartz, L.: Automatic detection and segmentation of large lung cancers from chest ct images. *Workshop of 11th International conference on Medical Image Computing and Computer Assisted Intervention* (2008)

- [30] Ukil, S., Reinhardt, J.: Smoothing lung segmentation surfaces in 3d x-ray ct images using anatomic guidance. In: SPIE. Volume 5370 of Medical Imaging. (2004) 1066–1075
- [31] Zheng, B., Leader, J., Maitz, G., Chapman, B., Fuhrman, C., Rogers, R., Scieurba, F., Perez, A., Thompson, P., Good, W., Gur, D.: A simple method for automated lung segmentation in x-ray ct images. In: SPIE. Volume 5032 of Medical Imaging. (2003) 1455–1463
- [32] Sluimer, I., Niemeijer, M., van Ginneken, B.: Lung field segmentation from thinslice ct scans in presence of severe pathology. In: SPIE. Volume 5370 of Medical Imaging. (2004) 1447–1455
- [33] Sonka, M., Park, W., Hoffman, E.: Rule-based detection of intrathoracic airway trees. *IEEE Transactions on Medical Imaging* **15** (1996) 314–326
- [34] Park, W., Hoffman, E., Sonka, M.: Segmentation of intrathoracic airway trees: a fuzzy logic approach. *IEEE Transactions on Medical Imaging* **17** (1998) 489–497
- [35] Sato, Y., Nakajima, S., Shiraga, N., Atsumi, H., Yoshida, S., Koller, T., Gerig, G., Kikinis, R.: Three-dimensional multi-scale line filter for segmentation and visualization of curvilinear structures in medical images. *Medical Image Analysis* **2** (1998) 143–168
- [36] Mori, K., Hasegawa, J., Suenaga, Y., Toriwaki, J.: Automated anatomical labeling of the bronchial branch and its application to the virtual bronchoscopy system. *IEEE Transactions on Medical Imaging* **19** (2000) 103–114
- [37] Deschamps, T., Cohen, L.: Fast extraction of minimal paths in 3d images and applications to virtual endoscopy. *Medical Image Analysis* **1** (2001) 1–19
- [38] Kitaoka, H., Park, Y., Tschirren, J., Reinhardt, J., Sonka, M., McLennan, G., Hoffman, E.: Automated nomenclature labeling of the bronchial tree in 3d-ct lung images. *Medical Image Computing and Computer-Assisted Intervention* **2489** (2002) 1–11
- [39] Reinhardt, J., D’Souza, N., Hoffman, E.: Accurate measurement of intrathoracic airways. *IEEE Transactions on Medical Imaging* **16** (1997) 820–827
- [40] Nakano, Y., Muro, S., Sakai, H., Hirai, T., Chin, K., Tsukino, M., Nishimura, K., Itoh, H., Paré, P., Hogg, J., Mishima, M.: Computed tomographic measurements of airway dimensions and emphysema in smokers. *American Journal of Respiratory and Critical Care Medicine* **162** (2000) 1102–1108
- [41] Ederle, J., Heussel, C., Hast, J., Fischer, B., van Beek, E., Ley, S., Thelen, M., Kauczor, H.U.: Evaluation of changes in central airway dimensions, lung area and mean lung density at paired inspiratory/expiratory high-resolution computed tomography. *European Radiology* **13** (2003) 2454–2461
- [42] Zidowitz, S., Schmidt, A.H., Kriete, A., Krass, S., Peitgen, H.O.: Steps towards a patient individual geometric model of the bronchial-tree used for functional simulations. In: SPIE. Volume 5369 of Medical Imaging. (2004) 125–131

- [43] Aylward, S., Bullitt, E.: Initialization, noise, singularities, and scale in height ridge traversal for tubular object centerline extraction. *IEEE Transactions on Medical Imaging* **21** (2002) 61–75
- [44] Swift, R., Kiraly, A., Sherbondy, A., Austin, A., Hoffman, E., McLennan, G., Higgins, W.: Automatic axis generation for virtual bronchoscopic assessment of major airway obstructions. *Computerized Medical Imaging and Graphics* **26** (2002) 103–118
- [45] Zhou, J., Chang, S., Metaxas, D., Mageras, G.: 3d-3d tubular organs registration based on bifurcations for the ct images. *IEEE Engineering in Medicine and Biology Society* (2008)
- [46] Kiraly, A., Higgins, W., McLennan, G., Hoffman, E., Reinhardt, J.: Threed imensional human airway segmentation methods for clinical virtual bronchoscopy. *Academic Radiology* **9** (2002) 1153–1168
- [47] Fetita, C., Prêteux, F.: Quantitative 3d ct bronchography. *IEEE International Symposium on Biomedical Imaging* (2002) 221–224
- [48] Mori, K., Hasegawa, J.i., Toriwaki, J.i., Anno, H., Katada, K.: Recognition of bronchus in three-dimensional x-ray ct images with application to virtualized bronchoscopy system. *International Conference on Pattern Recognition* **3** (1996) 528–532
- [49] Tschirren, J., Hoffman, E., McLennan, G., Sonka, M.: Airway tree segmentation using adaptive regions of interest. In: *SPIE. Volume 5369 of Medical Imaging*. (2004) 117–124
- [50] Kirbas, C., Quek, F.: A review of vessel extraction techniques and algorithms. *ACM Comput. Surv.* **36**(2) (2004) 81–121
- [51] Sarwal, A., Dhawan, A.: 3-d reconstruction of coronary arteries. *IEEE Conference Engineering in Medicine and Biology Society* **1** (1994) 504–505
- [52] Tozaki, T., Kawata, Y., Niki, N., Ohmatsu, H., Moriyama, N.: 3-d visualization of blood vessels and tumor using thin slice ct. *IEEE Nuclear Science Symposium and Medical Imaging Conference* **3** (1995) 1470–1474
- [53] Kawata, Y., Niki, N., Kumazaki, T.: An approach for detecting blood vessel diseases from cone-beam ct image. *IEEE Int. Conf. on Image Processing* **3** (1995) 500–503
- [54] Sorantin, E., Halmai, C., Erdohelyi, B., Palagyi, K., Nyul, L., Olle, K., Geiger, B., Lindbichler, F., Friedrich, G., Kiesler, K.: Spiral-ct based assessment of tracheal stenoses using 3-d skeletonization. *IEEE Trans. on Med. Img.* **21** (2002) 263–273
- [55] Bullitt, E., Aylward, S.: Analysis of timevarying images using 3d vascular models. *Applied Imagery Pattern Recognition Workshop* (2001) 9–14
- [56] Zhou, J., Chang, S., Metaxas, D.N., Axel, L.: Vascular structure segmentation and bifurcation detection. *IEEE International Symposium on Biomedical Imaging* (2007) 872–875

- [57] Aylward, S., Pizer, S., Bullitt, E., Eberl, D.: Intensity ridge and widths for tubular object segmentation and description. *Proceedings of the Workshop on Mathematical Methods in Biomedical Image Analysis* (1996) 131–138
- [58] Molina, C., Prause, G., Radeva, P., Sonka, M.: 3-d catheter path reconstruction from biplane angiograms. In: *SPIE. Volume 3338*. (1998) 504–512
- [59] Rueckert, D., Burger, P., Forbat, S.M., Mohiaddin, R.D., Yang, G.Z.: Automatic tracking of the aorta in cardiovascular mr images using deformable models. *IEEE Trans. on Med. Img.* **16** (1997) 581–590
- [60] Kozerke, S., Botnar, R., Oyre, S., Scheidegger, M.B., Pedersen, E., Boesinger, P.: Automatic vessel segmentation using active contours in cine phase contrast flow measurements. *Journal of Magnetic Resonance Imaging* **10** (1999) 41–51
- [61] Geiger, D., Gupta, A., Costa, L., Vlontzos, J.: Dynamic programming for detecting, tracking, and matching deformable contours. *PAMI* **17** (1995) 294–302
- [62] Chan, R., Karl, W., Lees, R.: A new model-based technique for enhanced small-vessel measurements in x-ray cine-angiograms. *IEEE Trans. on Med. Image* **19** (2000) 243–255
- [63] Krissian, K., Malandain, G., Vaillant, R., Troussset, Y., Ayache, N.: Model-based multiscale detection of 3d vessels. *IEEE Computer Society Conference on Computer Vision and Pattern Recognition* (1998) 722–727
- [64] Bors, A.G., Pitas, I.: Object segmentation and modeling in volumetric images. In *Proc. Wksp on Non-Linear Model Based Image Analysis* (1998) 295–300
- [65] Summers, P., Bhalerao, A.: Derivation of pressure gradients from magnetic resonance angiography using multi-resolution segmentation. *International Conference on Image Processing and its Applications* (1995) 404–408
- [66] Petrocelli, R., Manbeck, K., Elion, J.: Three dimensional structure recognition in digital angiograms using gauss-markov methods. *IEEE Computers in Cardiology* (1993) 101–104
- [67] Kass, M., Witkin, A., Terzoopoulos, D.: Snakes: Active contour models. *Int. J. Comput. Vision* **1** (1988) 321–331
- [68] Caselles, V., Catte, F., Coll, T., Dibos, F.: A geometric model for active contours in image processing. *Numer. Math.* **66** (1993) 1–32
- [69] Malladi, R., Sethian, J.A., Vemuri, B.C.: Shape modeling with front propagation: A level set approach. *PAMI* **17** (1995) 158–175
- [70] Pellot, C., Herment, A., Sigelle, M.: A3d reconstruction of vascular structures from two x-ray angiograms using an adapted simulated annealing algorithm. *IEEE Trans. on Med. Img.* **13** (1994) 48–60
- [71] Petrocelli, R., Elion, J., Manbeck, K.M.: A new method for structure recognition in unsubtracted digital angiograms. *IEEE Computers in Cardiology* (1992) 207–210

- [72] Cronemeyer, J., Heising, G., Orglmeister, R.: A fast skeleton finder for parallel hardware. *IEEE Computers in Cardiology* (1992) 23–26
- [73] Nekovei, R., Sun, Y.: Back-propagation network and its configuration for blood vessel detection in angiograms. *IEEE Trans. on Neural Nets* **6** (1995) 64–72
- [74] Hunter, I., Soraghan, J., McDonagh, T.: Fully automatic left ventricular boundary extraction in echocardiographic images. *IEEE Computers in Cardiology* (1995) 741–744
- [75] Kottke, D., Sun, Y.: Segmentation of coronary arteriograms by iterative ternary classification. *IEEE Trans. on Biomed. Engr.* **37** (1990) 778–785
- [76] Shiffman, S., Rubin, G.D., Napel, S.: Semiautomated editing of computed tomography sections for visualization of vasculature. In: *SPIE. Volume 2707.* (1996)
- [77] Rhoades, R., Tanner, G.: *Medical Physiology.* Lippincott Williams and Wilkins (2003)
- [78] Hayashi, K., Aziz, A., Ashizawa, K., Hayashi, H., Nagaoki, K., Otsuji, H.: Radiographic and ct appearances of the major fissures. *Radiographics* **21** (2001) 861–874
- [79] Yildiz, A., Gölpinar, F., Calikoğlu, M., Ducea, M., Ozer, C., Apaydin, F.: Hrcr evaluation of the accessory fissures of the lung. *European Journal of Radiology* **49** (2004) 245–249
- [80] Zhang, L., Hoffman, E., Reinhardt, J.: Lung lobe segmentation by graph search with 3d shape constraints. In: *SPIE. Volume 4321.* (2001) 204–215
- [81] Zhang, L., Hoffman, E., Reinhardt, J.: Atlas-driven lung lobe segmentation in volumetric x-ray ct images. *IEEE Transactions on Medical Imaging* **25** (2006) 1–16
- [82] Saita, S., Yasutomo, M., Kubo, M., Kawata, Y., Niki, N., Eguchi, K., Ohmatsu, H., Kakinuma, R., Kaneko, M., Kusumoto, M., Moriyama, M., Sasagawa, M.: An extraction algorithm of pulmonary fissures from multi-slice ct image. In: *SPIE. Volume 5370.* (2004) 1590–1597
- [83] Maintz, J., Viergever, M.: A survey of medical image registration. *Medical Image Analysis* **2** (1998) 1–36
- [84] Pluim, J., Maintz, J., Viergever, M.: Mutual-information-based registration of medical images: a survey. *IEEE Transactions on Medical Imaging* **22** (2003) 986–1004
- [85] Lester, H., Arridge, S.: A survey of hierarchical non-linear medical image registration. *Pattern Recognition* **32** (1999) 129–149
- [86] Mattes, D., Haynor, D., Vesselle, H., Lewellen, T., Eubank, W.: Pet-ct image registration in the chest using free-form deformations. *IEEE Transactions on Medical Imaging* **22** (2003) 120–128

- [87] Rueckert, D., Sonoda, L.I., Hayes, C., Hill, D.L.G., Leach, M.O., Hawkes, D.J.: Nonrigid registration using free-form deformations: application to breast mr images. *IEEE Transactions on Medical Imaging* **18** (1999) 712–721
- [88] Cai, J., Chu, J.C.H., Recine, D., Sharma, M., Nguyen, C., Rodebaugh, R., Saxena, V.A., Ali, A.: Ct and pet lung image registration and fusion in radiotherapy treatment planning using the chamfer-matching method. *International Journal of Radiation Oncology, Biology, Physics* **43** (1999) 883–891
- [89] Tai, Y.C., Lin, K.P., Hoh, C.K., Huang, S.C.H., Hoffman, E.J.: Utilization of 3-d elastic transformation in the registration of chest x-ray ct and whole body pet. *IEEE Transactions on Nuclear Science* **44** (1997) 1606–1621
- [90] Blaffert, T., Wiemker, R.: Comparison of different follow-up lung registration methods with and without segmentation. In: *SPIE*. Volume 5370. (2004) 1701–1708
- [91] Betke, M., Hong, H., Ko, J.: Landmark detection in the chest and registration of lung surfaces with an application to nodule registration. *Medical Image Analysis* **7** (2003) 265–281
- [92] Yamamoto, T., Kubo, M., Kawata, Y., Niki, N., Eguchi, K., Ohmatsu, H., Kakinuma, R., Kaneko, M., Kusumoto, M., Moriyama, N., Mori, K., , Nishiyama, H.: Automatic slice image matching algorithm for comparative reading using data of the pulmonary structure. In: *SPIE*. Volume 5370. (2004) 1091–1100
- [93] Dougherty, L., Asmuth, J.C., , Gefter, W.B.: Alignment of ct lung volumes with an optical flow method. *Academic Radiology* **10** (2003) 249–254
- [94] Stewart, C.V., Lee, Y.L., , Tsai, C.L.: An uncertainty-driven hybrid of intensity-based and feature-based registration with application to retinal and lung ct images. *Medical Image Computing and Computer-Assisted Intervention* **3216** (2003) 870–877
- [95] Fan, L., Chen, C., M.Reinhardt, J., Hoffman, E.A.: Evaluation and application of 3d lung warping and registration model using hrct images. In: *SPIE*. Volume 4321. (2001) 234–243
- [96] Boldea, V., Sarrut, D., Clippe, S.: Lung deformation estimation with non-rigid registration for radiotherapy treatment. *Medical Image Computing and Computer-Assisted Intervention* **2878** (2003) 770–777
- [97] Li, B., Christensen, G.E., Hoffman, E.A., McLennan, G., Reinhardt, J.M.: Establishing a normative atlas of the human lung: Intersubject warping and registration of volumetric ct images. *Academic Radiology* **10** (2003) 255–265
- [98] Zhang, L., Reinhardt, J.: 3d pulmonary ct image registration with a standard lung atlas. In: *SPIE*. Volume 3978. (2000) 67–77
- [99] Kanazawa, K., Kawata, Y., Niki, N., Satoh, H., Ohmatsu, H., Kakinuma, R., Kaneko, M., Moriyama, N., Eguchi, K.: Computer-aided diagnosis for pulmonary nodules based on helical ct images. *Computerized Medical Imaging and Graphics* **22** (1998) 157–167

- [100] Suzuki, K., Armato, S.G., Li, F., Sone, S., Doi, K.: Massive training artificial neural network (mtann) for reduction of false positives in computerized detection of lung nodules in low-dose computed tomography. *Medical Physics* **30** (2003) 1602–1617
- [101] Brown, M.S., McNitt-Gray, M.F., Goldin, J.G., Suh, R.D., Sayre, J.W., Aberle, D.R.: Patient-specific models for lung nodule detection and surveillance in ct images. *IEEE Transactions on Medical Imaging* **20** (2001) 1242–1250
- [102] Lee, Y., Tsai, D.Y., Hara, T., Fujita, H., Itoh, S., Ishigaki, T.: Improvement in automated detection of pulmonary nodules on helical x-ray ct images. In: *SPIE*. Volume 5370. (2004) 824–832
- [103] Tanino, M., Takizawa, H., Yamamoto, S., Matsumoto, T., Tateno, Y., Iinuma, T.: A detection method of ground glass opacities in chest x-ray ct images using automatic clustering techniques. In: *SPIE*. Volume 5032. (2003) 1728–1737
- [104] Saita, S., Oda, T., Kubo, M., Kawata, Y., Niki, N., Sasagawa, M., Ohmatsu, H., Kakinuma, R., Kaneko, M., Kusumoto, M., Eguchi, K., Nishiyama, H., Mori, K., Moriyama, N.: Nodule detection algorithm based on multi-slice ct images for lung cancer screening. In: *SPIE*. Volume 5370. (2004) 1083–1090
- [105] Armato, S.G., Giger, M.L., Moran, C.J., Blackburn, J.T., Doi, K., MacMahon, H.: Computerized detection of pulmonary nodules on ct scans. *Radiographics* **19** (1999) 1303–1311
- [106] Ko, J.P., Betke, M.: Chest ct: Automated nodule detection and assessment of change over time-preliminary experience. *Radiology* **218** (2001) 267–273
- [107] Zhao, B., Ginsberg, M.S., Lefkowitz, R.A., Jiang, L., Cooper, C., Schwartz, L.H.: Application of the ldm algorithm to identify small lung nodules on low-dose msct scans. In: *SPIE*. Volume 5370. (2004) 818–823
- [108] Ezoe, T., Takizawa, H., Yamamoto, S., Shimizu, A., Matsumoto, T., Tateno, Y., Iinuma, T., Matsumoto, M.: An automatic detection method of lung cancers including ground glass opacities from chest x-ray ct images. In: *SPIE*. Volume 4684. (2002) 1672–1680
- [109] Fetita, C.I., Prêteux, F., Beigelman-Aubry, C., Grenier, P.: 3d automated lung nodule segmentation in hrct. *Medical Image Computing and Computer-Assisted Intervention* **2878** (2003) 626–634
- [110] Awai, K., Murao, K., Ozawa, A., Komi, M., Hayakawa, H., Hori, S., Nishimura, Y.: Pulmonary nodules at chest ct: Effect of computer-aided diagnosis on radiologists' detection performance. *Radiology* **230** (2004) 347–352
- [111] Lee, Y., Hara, T., Fujita, H., Itoh, S., Ishigaki, T.: Automated detection of pulmonary nodules in helical ct images based on an improved template-matching technique. *IEEE Transactions on Medical Imaging* **20** (2001) 595–604
- [112] Farag, A., El-Baz, A., Gimel'farb, G.G., Falk, R., Hushek, S.G.: Automatic detection and recognition of lung abnormalities in helical ct images using deformable

- templates. *Medical Image Computing and Computer-Assisted Intervention* **3217** (2004) 856–864
- [113] Gurcan, M.N., Sahiner, B., Petrick, N., Chan, H.P., Kazerooni, E.A., Cascade, P.N., Hadjiiski, L.: Lung nodule detection on thoracic computed tomography images: Preliminary evaluation of a computer-aided diagnosis system. *Medical Physics* **29** (2002) 2552–2558
 - [114] Kubo, M., Kubota, K., Yamada, N., Kawata, Y., Niki, N., Eguchi, K., Ohmatsu, H., Kakinuma, R., Kaneko, M., Kusumoto, M., Mori, K., Nishiyama, H., Moriyama, N.: A cad system for lung cancer based on low dose single-slice ct image. In: *SPIE. Volume 4684*. (2002) 1672–1680
 - [115] Yamada, N., Kubo, M., Kawata, Y., Niki, N., Eguchi, K., Omatsu, H., Kakinuma, R., Kaneko, M., Kusumoto, M., Nishiyama, H., Moriyama, N.: Roi extraction of chest ct images using adaptive opening filter. In: *SPIE. Volume 5032*. (2003) 869–876
 - [116] Oda, T., Kubo, M., Kawata, Y., Niki, N., Eguchi, K., Ohmatsu, H., Kakinuma, R., Kaneko, M., Kusumoto, M., Moriyama, N., Mori, K., Nishiyama, H.: A detection algorithm of lung cancer candidate nodules on multi-slice ct images. In: *SPIE. Volume 4684*. (2002) 1354–1361
 - [117] Wei, G.Q., Fan, L., Qian, J.: Automatic detection of nodules attached to vessels in lung ct by volume projection analysis. *Medical Image Computing and Computer-Assisted Intervention* **2488** (2002) 746–752
 - [118] Mekadaa, Y., Kusanagi, T., Hayase, Y., Mori, K., i. Hasegawa, J., i. Toriwaki, J., Mori, M., Natori, H.: Detection of small nodules from 3d chest x-ray ct images based on shape features. *Computer Assisted Radiology and Surgery* **1256** (2003) 971–976
 - [119] Enquobahrie, A.A., Reeves, A.P., Yankelevitz, D.F., Henschke, C.I.: Automated detection of pulmonary nodules from whole lung helical ct scans: Performance comparison for isolated and attached nodules. In: *SPIE. Volume 5370*. (2004) 791–800
 - [120] Wiemker, R., Rogalla, P., Zwartkruis, A., Blaffert, T.: Computer aided lung nodule detection on high resolution ct data. In: *SPIE. Volume 4684*. (2002) 677–688
 - [121] Chang, S., Emoto, H., Metaxas, D.N., Axel, L.: Pulmonary micronodule detection from 3d chest ct. *Medical Image Computing and Computer-Assisted Intervention* **3217** (2004) 821–828
 - [122] Li, Q., Doi, K.: New selective enhancement filter and its application for significant improvement of nodule detection on computed tomography. In: *SPIE. Volume 5370*. (2004) 1–9
 - [123] Paik, D.S., Beaulieu, C.F., Rubin, G.D., Acar, B., Jeffrey, R.B.J., Yee, J., Dey, J., Napel, S.: Surface normal overlap: A computer-aided detection algorithm with application to colonic polyps and lung nodules in helical ct. *IEEE Transactions on Medical Imaging* **23** (2004) 661–675

- [124] Takizawa, H., Yamamoto, S., Matsumoto, T., Tatenno, Y., Iinuma, T., Matsumoto, M.: Recognition of lung nodules from x-ray ct images using 3d markov random field models. In: SPIE. Volume 4684. (2002) 716–725
- [125] Fukano, G., Takizawa, H., Shigemoto, K., Yamamoto, S., Matsumoto, T., Tatenno, Y., Iinuma, T.: Recognition method of lung nodules using blood vessel extraction techniques and 3d object models. In: SPIE. Volume 5032. (2003) 190–196
- [126] Armato, S.G., Giger, M.L., MacMahon, H.: Automated detection of lung nodules in ct scans: Preliminary results. *Medical Physics* **28** (2001) 1552–1561
- [127] Arimura, H., Katsuragawa, S., Suzuki, K., Li, F., Shiraishi, J., Sone, S., Doi, K.: Computerized scheme for automated detection of lung nodules in low-dose computed tomography images for lung cancer screening. *Academic Radiology* **11** (2004) 617–629
- [128] Armato, S.G., Li, F., Giger, M.L., MacMahon, H., Sone, S., Doi, K.: Lung cancer: performance of automated lung nodule detection applied to cancers missed in a ct screening program. *Radiology* **225** (2002) 685–692
- [129] Zhang, X., McLennan, G., Hoffman, E.A., Sonka, M.: Computerized detection of pulmonary nodules using cellular neural networks in ct images. In: SPIE. Volume 5370. (2004) 30–41
- [130] McCulloch, C.C., Kaucic, R.A., Mendonça, P.R., Walter, D.J., Avila, R.S.: Model-based detection of lung nodules in computed tomography exams. *Academic Radiology* **11** (2004) 258–266
- [131] Wormanns, D., Diederich, S.: Characterization of small pulmonary nodules by ct. *European Radiology* **14** (2004) 1380–1391
- [132] Diederich, S., Wormanns, D., Semik, M., Thomas, M., Lenzen, H., Roos, N., Heindel, W.: Screening for early lung cancer with low-dose spiral ct: Prevalence in 817 asymptomatic smokers. *Radiology* **222** (2002) 773–781
- [133] Tan, B.B., Flaherty, K.R., Kazerooni, E.A., Iannettoni, M.D.: The solitary pulmonary nodule. *Chest* **123** (2003) 89S–96S
- [134] Ost, D., Fein, A.: Evaluation and management of the solitary pulmonary nodule. *American Journal of Respiratory and Critical Care Medicine* **162** (2000) 782–787
- [135] Yankelevitz, D.F., Henschke, C.I.: Lung cancer: small pulmonary nodules. *Radiologic Clinics of North America* **38** (2000) 1–9
- [136] Erasmus, J.J., Connolly, J.E., McAdams, H.P., Roggli, V.L.: Solitary pulmonary nodules: Part i. morphologic evaluation for differentiation of benign and malignant lesions. *Radiographics* **20** (2000) 43–58
- [137] Gurney, J.: Determining the likelihood of malignancy in solitary pulmonary nodules with bayesian analysis. part i. theory. *Radiology* **186** (1993) 405–413
- [138] Henschke, C.I., Yankelevitz, D.F., Mateescu, I., Brettle, D.W., Rainey, T.G., Weingard, F.S.: Neural networks for the analysis of small pulmonary nodules. *Clinical Imaging* **21** (1997) 390–399

- [139] McNitt-Gray, M.F., Hart, E., Wyckoff, N., Sayre, J.W., Goldin, J.G., Aberle, D.R.: A pattern classification approach to characterizing solitary pulmonary nodules imaged on high resolution ct: Preliminary results. *Medical Physics* **26** (1999) 880–888
- [140] McNitt-Gray, M.F., Wyckoff, N., Sayre, J., Goldin, J.G., Aberle, D.R.: The effects of co-occurrence matrix based texture parameters on the classification of solitary pulmonary nodules imaged on computed tomography. *Computerized Medical Imaging and Graphics* **23** (1999) 339–348
- [141] Kawata, Y., Niki, N., Ohmatsu, H., Kusumoto, M., Kakinuma, R., Mori, K., Nishiyama, H., Eguchi, K., Kaneko, M., Moriyama, N.: Searching similar images for classification of pulmonary nodules in three-dimensional ct images. *IEEE International Symposium on Biomedical Imaging* (2002) 189–193
- [142] Kawata, Y., Niki, N., Ohmatsu, H., Kusumoto, M., Kakinuma, R., Mori, K., Yamada, K., Nishiyama, H., Eguchi, K., Kaneko, M., Moriyama, N.: Pulmonary nodule classification based on ct density distribution using 3d thoracic ct images. In: *SPIE*. Volume 5369. (2004) 413–422
- [143] Erasmus, J.J., McAdams, H.P., Connolly, J.E.: Solitary pulmonary nodules: Part ii. evaluation of the indeterminate nodule. *Radiographics* **20** (2000) 59–66
- [144] Ko, J.P., Naidich, D.P.: Lung nodule detection and characterization with multi-slice ct. *Radiologic Clinics of North America* **41** (2003) 575–597
- [145] Takashima, S., Sone, S., Li, F., Maruyama, Y., Hasegawa, M., Kadoya, M.: Indeterminate solitary pulmonary nodules revealed at population-based ct screening of the lung: using first follow-up diagnostic ct to differentiate benign and malignant lesions. *American Journal of Roentgenology* **180** (2003) 1255–1263
- [146] Takashima, S., Sone, S., Li, F., Maruyama, Y., Hasegawa, M., Matsushita, T., Takayama, F., Kadoya, M.: Small solitary pulmonary nodules (≤ 1 cm) detected at population-based ct screening for lung cancer: reliable high-resolution ct features of benign lesions. *American Journal of Roentgenology* **180** (2003) 955–964
- [147] Matsuki, Y., Nakamura, K., Watanabe, H., Aoki, T., Nakata, H., Katsuragawa, S., Doi, K.: Usefulness of an artificial neural network for differentiating benign from malignant pulmonary nodules on high-resolution ct: Evaluation with receiver operating characteristic analysis. *American Journal of Roentgenology* **178** (2002) 657–663
- [148] Li, Q., Li, F., Shiraishi, J., Katsuragawa, S., Sone, S., Doi, K.: Investigation of new psychophysical measures for evaluation of similar images on thoracic computed tomography for distinction between benign and malignant nodules. *Medical Physics* **30** (2003) 2584–2593
- [149] Wormanns, D., Diederich, S., Lentschig, M.G., Winter, F., Heindel, W.: Spiral ct of pulmonary nodules: interobserver variation in assessment of lesion size. *European Radiology* **10** (2000) 710–713

- [150] Fan, L., Qian, J., Odry, B., Shen, H., Naidich, D., Kohl, G., Klotz, E.: Automatic segmentation of pulmonary nodules by using dynamic 3d cross-correlation for interactive cad systems. In: SPIE. Volume 4684. (2002) 1362–1369
- [151] Kuhnigk, J.M., Dicken, V., Bornemann, L., Wormanns, D., Krass, S., Peitgen, H.O.: Fast automated segmentation and reproducible volumetry of pulmonary metastases in ct-scans for therapy monitoring. *Medical Image Computing and Computer-Assisted Intervention* **3217** (2004) 933–941
- [152] Mullally, W., Betke, M., Wang, J.: Segmentation of nodules on chest computed tomography for growth assessment. *Medical Physics* **31** (2004) 839–848
- [153] Kostis, W., Reeves, A., Yankelevitz, D., Henschke, C.: Three-dimensional segmentation and growth rate estimation of small pulmonary nodules in helical ct images. *IEEE Trans. Med. Imag.* **22**(10) (2003) 1259–1274
- [154] Zhao, B., Yankelevitz, D., Reeves, A., Henschke, C.: Two-dimensional multi-criterion segmentation of pulmonary nodules on helical ct images. *Medical Physics* **26** (1999) 889–895
- [155] Okada, K., Comaniciu, D., Krishnan, A.: Robust 3d segmentation of pulmonary nodules in multislice ct images. *Medical Image Computing and Computer-Assisted Intervention* **3217** (2004) 881–889
- [156] Zhang, L., Fang, M., Naidich, D.P., Novak, C.L.: Consistent interactive segmentation of pulmonary ground glass nodules identified in ct studies. In: SPIE. Volume 5370. (2004) 1709–1719
- [157] Binaghi, S., Maeder, P., Uské, A., Meuwly, J.Y., Devuyt, G., Meuli, R.: Three-dimensional computed tomography angiography and magnetic resonance angiography of carotid bifurcation stenosis. *European Neurology* **46** (2001) 25–34
- [158] Lorenz, C., Carlsen, I.C., Buzug, T., Fassnacht, C., Weese, J.: Multi-scale line segmentation with automatic estimation of width, contrast and tangential direction in 2d and 3d medical images. In: *Proceedings of the First Joint Conference on Computer Vision, Virtual Reality and Robotics in Medicine and Medical Robotics and Computer-Assisted Surgery*. Volume 1205. (1997) 233–242
- [159] Krissian, K., Malandain, G., Ayache, N., Vaillant, R., Troussset, Y.: Model-based detection of tubular structures in 3d images. *Computer Vision and Image Understanding* **80**(2) (2000) 130–171
- [160] Pock, T., Beichel, R., Bischof, H.: A novel robust tube detection filter for 3d centerline extraction. In: *SCIA*. (2005) 481–490
- [161] Frangi, A.: *Three-Dimensional Model-Based Analysis of Vascular and Cardiac Images*. PhD thesis, University Medical Center Utrecht, Netherlands (2001)
- [162] Chang, S., Metaxas, D., Axel, L.: Scan-conversion algorithm for ridge point detection on tubular objects. *MICCAI* **2** (2003) 158–165

- [163] Zhou, J., Chang, S., Metaxas, D., Axel, L.: Vessel boundary extraction using ridge scan-conversion and deformable model. *IEEE International Symposium on Biomedical Imaging* (2006) 189–192
- [164] Freund, Y., Schapire, R.: Experiments with a new boosting algorithm. the 13th International Conference on Machine Learning (1996) 148–156
- [165] Schapire, R.: The boosting approach to machine learning: An overview. In: *MSRI Workshop on Nonlinear Estimation and Classification*. (2002)
- [166] Luo, H., Liu, Y., Yang, X.: Particle deposition in obstructed airways. *Journal of Biomechanics* **40** (2007) 3096–3104
- [167] Gee, J., Sundaram, T., Hasegawa, I., Uematsu, H., Hatabu, H.: Characterization of regional pulmonary mechanics from serial mri data. *MICCAI* (2002) 762–769
- [168] Aylward, S., Jomier, J., Weeks, S., Bullitt, E.: Registration and analysis of vascular images. *IJCV* **55** (2003) 123–138
- [169] Austin, J., Muller, N., Friedman, P.e.a.: Glossary of terms for CT of the lung: recommendations of the nomenclature committee of the fleischner society. *Radiology* **200** (1996) 327–331
- [170] Jang, H., Lee, K., Kwon, O., Rhee, C., Shim, Y., Han, J.: Bronchioloalveolar carcinoma: focal area of ground-glass attenuation at thin-section CT as an early sign. *Radiology* **199** (1996) 485–488
- [171] Kuriyama, K., Seto, M., Kasugai, T., Higashiyama, M., Kido, S., Sawai, Y., Kodama, K., Kuroda, D.: Ground-glass opacity on thin-section CT: value in differentiating subtypes of adenocarcinoma of the lung. *Am. J. Roentgenol.* **173** (1999) 465–469
- [172] Watanabe, S., Watanabe, T., Arai, K., Kasai, T., Haratake, J., Urayama, H.: Results of wedge resection for focal bronchioloalveolar carcinoma showing pure ground-glass attenuation on computed tomography. *Ann. Thorac. Surg.* **73** (2002) 1071–1075
- [173] Heitmann, K., Kauczor, H.U., Mildenerberger, P., Uthmann, T., Perl, J., Thelen, M.: Automatic detection of ground glass opacities on lung HRCT using multiple neural networks. *European Radiology* **7** (1997) 1463–1472
- [174] Miller, A., Hogestraeten, B., Staquet, M., et al.: Reporting results of cancer treatment. *Cancer* **47** (1981) 207–214
- [175] Therasse, P., Arbuck, S., Eisenhauer, E., et al.: New guidelines to evaluate response to treatment in solid tumors. *J. Natl. Cancer Inst.* **92** (2000) 205–216
- [176] Zhao, B., Schwartz, L., Moskowitz, C., Ginsberg, M., Rizvi, N., Kris, M.: Lung Cancer: Computerized Quantification of Tumor Response—Initial Results. *Radiology* **241** (2006) 892–898

- [177] Zhao, B., Gamsu, G., Ginsberg, M., Jian, L., Schwartz, L.: Automatic detection of small lung nodules on ct utilizing a local density maximum algorithm. *J. Appl. Clin. Med. Phys.* **4**(3) (2003) 248–260
- [178] Zhao, B., Yankelevitz, D., Reeves, A., Henschke, C.: Two-dimensional multi-criterion segmentation of pulmonary nodules on helical ct images. *IEEE Trans. Med. Imag.* **22**(10) (2003) 1259–1274
- [179] Boscolo, R., Brown, M., McNitt-Gray, M.: Medical image segmentation with knowledge-guided robust active contours. *RadioGraphics* **33** (2002) 437–448
- [180] Ko, J.P., Rusinek, H., Jacobs, E.L., Babb, J.S., Betke, M., McGuinness, G., Naidich, D.P.: Small pulmonary nodules: volume measurement at chest ct-phantom study. *Radiology* **228** (2003) 864–870
- [181] Danielsson, P.E., Lin, Q.: Efficient detection of second-degree variations in 2d and 3d images. *Journal of Visual Communication and Image Representation* **12** (2001) 255–305
- [182] Ali, S., Silvey, S.: A general class of coefficients of divergence of one distribution from another. *J. Roy. Stat. Soc.* **28** (1966) 131–142
- [183] Cootes, T., Taylor, C., Cooper, D., Graham, J.: Active shape models—their training and application. *Comp. Vis. Imag. Under.* **61**(1) (1995) 38–59
- [184] De La Torre, F., Black, M.: A framework for robust subspace learning. *Int. J. Comput. Vis.* **54**(1-3) (2003) 117–142
- [185] Metaxas, D.N.: *Physics-Based Deformable Models: Applications to Computer Vision, Graphics and Medical Imaging*. Kluwer Academic Publishers (1997)
- [186] Xu, C., Prince, J.: Snakes, shapes, and gradient vector flow. *IEEE Transactions on Image Processing* **7**(3) (1998) 359–369
- [187] Lindeberg, T.: Principles for automatic scale selection. In et al., B.J., ed.: *Handbook on Computer Vision and Applications*. Academic Press, Boston, USA (1999) 239–274
- [188] Viola, P., Jones, M.: Robust real-time object detection. *Second International Workshop on Statistical and Computational Theories of Vision—Modeling, Learning, and Sampling* (2001)
- [189] Levine, M., Nazif, A.: An experimental rule based system for testing low level segmentation strategies. *Multi-Computers and Image Processing: Algorithms and Programs* (1982) 149–160
- [190] Efron, B.: Estimating the error rate of a prediction rule: Improvement on cross-validation. *Journal of the American Statistical Association* **78** (1983) 316–331
- [191] Haralick, R.: Statistical and structural approaches to texture. *Proc IEEE* **67** (1979) 785–804
- [192] Parker, J.: *Algorithms for image processing and computer vision*. New York, NY: Wiley (1997)

- [193] Kim, K.G., Goo, J.M., Kim, J.H., Lee, H.J., Min, B.G., Bae, K.T., Im, J.G.: Computer-aided diagnosis of localized ground-glass opacity in the lung at ct: Initial experience. *Radiology* **237** (2005) 657–661
- [194] Zhou, J., Chang, S., Metaxas, D.N., Zhao, B., Schwartz, L.H., Ginsberg, M.S.: Automatic detection and segmentation of ground glass opacity nodules. *International conference on Medical Image Computing and Computer Assisted Intervention (MICCAI)* (2006)

Vita

Jinghao Zhou

1993-1998 B. Sc. in Electrical Engineering from Tsinghua University, China

2003-2006 M. S. in Statistics, Rutgers University

2002-2008 Ph. D. in Biomedical Engineering, Rutgers University

2002-2008 Graduate Assistant, Department of Biomedical Engineering, Rutgers, the State University of New Jersey, New Brunswick, NJ, USA

MICCAI'08 Jinghao Zhou, Sukmoon Chang, Dimitris Metaxas, Binsheng Zhao, Michelle Ginsberg, Lawrence Schwartz, "Automatic Detection and Segmentation of Large Lung Cancers from Chest CT Images", Workshop of 11th International conference on Medical Image Computing and Computer Assisted Intervention (MICCAI), 2008.

EMBS'08 Jinghao Zhou, Sukmoon Chang, Dimitris Metaxas, Gig Mageras, "3D-3D Tubular Organs Registration based on Bifurcations for the CT Images", IEEE Engineering in Medicine and Biology Society (EMBS), 2008.

ISBI'08 Jinghao Zhou, Sukmoon Chang, Qingshan Liu, George Pappas, Vasilios Boronikolas, Michael Michaelides, Nora Volkow, Panayotis Thanos, Dimitris Metaxas, "A Novel Learning Based Segmentation Method For Rodent Brain Structures Using MRI", IEEE International Symposium on Biomedical Imaging (ISBI), pp. 61-64, 2008.

ISBI'07 Jinghao Zhou, Sukmoon Chang, Dimitris N. Metaxas, Leon Axel, "Vascular Structure Segmentation and Bifurcation Detection", IEEE International Symposium on Biomedical Imaging (ISBI), pp. 872-875, 2007.

MICCAI'07 Sukmoon Chang, Jinghao Zhou, Qingshan Liu, Dimitris Metaxas, Bruce Haffty, Sung Kim, Salma Jabbour, Ning Yue, "Registration of lung tissue between fluoroscope and CT images: determination of beam gating parameters in radiotherapy", 10th International conference on Medical Image Computing and Computer Assisted Intervention (MICCAI), pp. 751-758, 2007.

- CVPR'07** Shaohua Zhou, Jinghao Zhou, Dorin Comaniciu, "A boosting regression approach to medical anatomy detection", IEEE Conference on Computer Vision and Pattern Recognition (CVPR), pp. 1-8, 2007.
- BMES'06** Jinghao Zhou, Sukmoon Chang, Dimitris N. Metaxas, Binsheng Zhao, Michelle S. Ginsberg, Lawrence H. Schwartz, "An Automatic Detection and Level Set Segmentation Method for Ground Glass Opacity Nodule from CT Studies", in Proceedings of Biomedical Engineering Society (BMES), 2006.
- NSS/MIC'06** Vasilios Boronikolas, Michael Michaelides, Jinghao Zhou, Gene-Jack Wang¹, Steve Blackband, Samuel C. Grant, Dimitris Metaxas, Nora D. Volkow and Panayotis K. Thanos, "Validation of the Active Shape Model (ASM) for Automatic Brain Region Segmentation", in Proceedings of IEEE Nuclear Science Symposium and Medical Imaging Conference (NSS/MIC), 2006.
- EMBS'06** Jinghao Zhou, Sukmoon Chang, Dimitris N. Metaxas, Binsheng Zhao, Michelle S. Ginsberg, Lawrence H. Schwartz, "An Automatic Method for Ground Glass Opacity Nodule Detection and Segmentation from CT Studies", IEEE Engineering in Medicine and Biology Society (EMBS), pp. 3062-3065, 2006.
- MICCAI'06** Jinghao Zhou, Sukmoon Chang, Dimitris N. Metaxas, Binsheng Zhao, Michelle S. Ginsberg, Lawrence H. Schwartz, "Automatic Detection and Segmentation of Ground Glass Opacity Nodules," Medical Image Computing and Computer Assisted Intervention (MICCAI), pp. 784-791, 2006.
- ISBI'06** Jinghao Zhou, Sukmoon Chang, Dimitris N. Metaxas, Leon Axel, "Vessel Boundary Extraction Using Ridge Scan-Conversion and the Deformable Model," IEEE International Symposium on Biomedical Imaging (ISBI), pp. 189-192, 2006.
- SPIE'06** Sukmoon Chang, Jinghao Zhou, Dimitris N. Metaxas, Leon Axel, "False-Positive Elimination for Computer-Aided Detection of Pulmonary Micronodules," SPIE International Symposium on Medical Imaging, Vol. 6144, pp. 1751-1758, 2006.
- JTU'01** Jie Liu, Yiding Wang, Shangkai Gao, Zheng Li, Xiaorong Gao, Jinghao Zhou, "Calibration of 3D ultrasound imaging system based on magnetic position sensor", Journal of Tsinghua University (Science and Technology), vol. 09, pp. 18-21, 2001.
- EMBS'98** Jie Liu, Xiaorong Gao, Zhiguang Zhang, Shangkai Gao, Jinghao Zhou. "A new calibration method in 3D ultrasonic imaging system", 20th Annual International Conference of the IEEE Engineering in Medicine and Biology Society, pp. 839-841, 1998.